Astronomy & Astrophysics manuscript no. hd99458_arxiv
October 26, 2026
©ESO 2026

A comprehensive reanalysis of HD 99458

Not a magnetic Ap star but an oscillating Algol with ongoing mass transfer

E. Semenko[1⋆], Z. Mikulášek[2], D. Mkrtichian[1], P. Walczak[3], M. Gabdeev[4], J. Janík[2], O. Kochukhov[5], J. Kolář[2,6], E. Paunzen[2], M. E. Shultz[7], M. Skarka[8,2], V.N. Aitov[9], A.S. Beskakotov[9], R. Brahm[10,11,12], V.V. Dyachenko[9], L. Eyer[13], P. Kabáth[8], O. Kvaratskhelia[14], T. Kvernadze[14], J. Lipták[8], A.V. Moiseeva[9], V. Schaffenroth[15], L. Vanzi[16,17], and J. Žák[8]

[1] National Astronomical Research Institute of Thailand (Public Organization), Chiang Mai, 50180 Thailand
[2] Department of Theoretical Physics and Astrophysics, Masaryk University, Kotlářská 2, 611 37 Brno, Czech Republic
[3] Astronomical Institute, University of Wrocław, PL-51-622 Wrocław, Poland
[4] Pavol Jozef Šafárik University in Košice, Faculty of Science, Košice, Slovakia
[5] Department of Physics and Astronomy, Uppsala University, Box 524, 75120, Uppsala, Sweden
[6] Institute of Astronomy, Faculty of Physics, Astronomy and Informatics, Nicolaus Copernicus University in Toruń, Piwnice k. Torunia, PL-87148 Łysomice, Poland
[7] Independent researcher, Kingston, Ontario K7L 3N6, Canada
[8] Astronomical Institute of the Czech Academy of Sciences, Fričova 298, CZ-25165 Ondřejov, Czech Republic
[9] Special Astrophysical Observatory, Nizhnij Arkhyz, 369167, Russia
[10] Facultad de Ingeniería y Ciencias, Universidad Adolfo Ibáñez, Av. Diagonal las Torres 2640, Peñalolén, Santiago, Chile
[11] Millennium Institute for Astrophysics, Chile
[12] Data Observatory Foundation, Chile
[13] Department of Astronomy, University of Geneva, Chemin Pegasi 51, 1290 Versoix, Switzerland
[14] E. Kharadze Georgian National Astrophysical Observatory, 0301, Abastumani, Georgia
[15] Thüringer Landessternwarte, 07778 Tautenburg, Germany
[16] Centre for Astro Engineering, Pontificia Universidad Católica de Chile, Santiago, Chile
[17] Department of Electrical Engineering, Pontificia Universidad Católica de Chile, Santiago, Chile

Received date / Accepted date

ABSTRACT

Context. Since 2019, HD 99458 has been known as a unique example of a δ Sct variable with chemical peculiarities of Ap type in an eclipsing binary.
Aims. We aim to review the peculiar status of the star with new observational materials.
Methods. The current study is the result of meticulous analysis of space-based photometry from Kepler K2 and TESS, multi-site spectroscopic and spectropolarimetric observations, as well as speckle-interferometric data. Asteroseismic modelling of stellar pulsation is an essential part of the research.
Results. We find HD 99458 to be an eclipsing Algol-type system with active mass transfer from the cool companion filling its Roche lobe to the pulsating primary. We identified signatures of a disc and accretion with varying rates in spectra and light curves. The system's orbital period increases with the rate $\dot{P}_{\rm orb}$ of 5.045 s yr^{-1}, indicating potential multiplicity. We failed to detect traces of the primary's magnetic field or excessive abundances, both of which are necessary to classify HD 99458 as an Ap star. We have constrained the fundamental parameters of the pulsating primary and analysed its pulsation using asteroseismology. In space-based photometry, we identified pulsation modes with angular degree $\ell \leq 3$. Two-dimensional Fourier analysis of spectroscopic time series reveals pulsations in the form of standing waves with the azimuthal orders $|m| = 5 \pm 1$. Combined analysis of photometry and spectroscopy confirms the status of HD 99458 as a triaxial gravitationally distorted pulsator.
Conclusions. Our comprehensive study affirms the new classification for HD 99458.

Key words. Binaries: eclipsing – Stars: chemically peculiar – Stars: delta Scuti – Stars: abundances – Stars: individual: HD 99458

1. Introduction

Amid the surge of interest in the search for new exoplanets in space-based photometry obtained by the Kepler K2 mission (Borucki et al. 2010; Howell et al. 2014), Barros et al. (2016) identified HD 99458 as a candidate exoplanetary system after recognising periodic eclipses with a depth of 1.494%. In the follow-up study, Skarka et al. (2019) identified the secondary as a low-mass red dwarf star rather than an exoplanet. The primary component was found to be an A-type pulsating δ Scuti (hereafter, δ Sct) star with extensive spots and anomalous chemical composition. The reported excesses of Fe, Si, and Ti exceeded 1 dex compared to the Sun, allowing the authors to classify the primary component of HD 99458 as an Ap star.

The Ap stars form a subgroup of the family of chemically peculiar (CP) stars, mostly main-sequence objects with abnormal spectra indicating a peculiar chemical composition. The frac-

⋆ Corresponding author: eugene@narit.or.th

tion of CP stars among objects of a similar effective temperature is approximately 10%. Preston (1974) subdivided CP stars into four subgroups, where A stars with peculiar spectra occur in the groups CP1 and CP2. The populations of these groups differ in the character of variability, chemical composition, magnetism, and binarity. Strong, globally organised magnetic fields are the hallmark of Ap variables of the α^2 Canum Venaticorum (ACV; Hümmerich et al. 2018) type, or CP2 stars. Hereafter, we use Ap and CP2 interchangeably to refer to this class. According to the information presented in the Gaia Data Release 3 (DR3) catalogue, HD 99458 is classified as a variable of ACV|CP|MCP|ROAM|ROAP|SXARI type with a score of 0.27 (Eyer et al. 2023; Gavras et al. 2023; Rimoldini et al. 2023).

In contrast to their non-magnetic siblings, the CP2 stars seem to avoid close binary systems. The fraction of the known systems harbouring magnetic components shrinks rapidly with a decreasing orbital period (e.g. Carrier et al. 2002; Mathys 2017). To the best of our knowledge, only three such systems with periods shorter than 3 days are known: HD 15144 (Bonsack 1981; Cowley & Hubrig 2008), HD 200405 (Carrier et al. 2002), and HD 99458. Of the three, only the object of this study undoubtedly has a companion, as its radial velocity varies with a high amplitude and photometry shows eclipses.

The δ Sct variables are common among A-type stars. Many of them appear to be members of close binary systems. The δ Sct variables are multi-periodic pulsators of luminosity classes V to III with masses between approximately $1.5 M_\odot$ and $2.5 M_\odot$ (Handler 2009). The observed light changes are caused by multiple radial and non-radial low-order pressure (p) modes, which are excited through the κ mechanism (Handler 2009). In evolved δ Sct stars, so-called mixed modes are often observed. These pulsation modes exhibit gravity (g) mode characteristics in the interior and p-mode characteristics near the stellar surface (Bowman et al. 2016).

The coexistence of the δ Sct-type pulsation with the strong magnetic fields typical of Ap stars is an important observational effect with a wide potential application (e.g. Buysschaert et al. 2017; Neiner 2024). On the one hand, asteroseismology is the only reliable method for probing the internal structure of stars. On the other hand, incorporating magnetic effects into the theory of stellar oscillations is challenging (Walczak & Daszyńska-Daszkiewicz 2018). Observationally, identifying δ Sct pulsations in magnetic CP2 stars is also challenging. Spectral lines are simultaneously distorted by pulsation, Zeeman splitting, and chemical spots, complicating spectroscopic analyses (see, e.g. Gutteridge et al. 2026). Consequently, only a small number of CP2 stars are currently reported to exhibit δ Sct pulsations, most of which have been identified from photometry alone. As an example, Thomson-Paressant et al. (2025) reported only 13 stars. Many of these pulsators fall outside the classical instability strip, suggesting either inaccuracies in physical parameters or incorrect identification of pulsators as CP2 due to hidden binarity. Stellar pulsation with eclipses, as observed in HD 99458, provides a unique opportunity for a precise characterisation of the pulsator and its companion.

Skarka et al. (2019) considered the presence of a cool inflated companion with an accretion disc as an alternative interpretation of the out-of-eclipse variation of HD 99458. However, this scenario was rejected in favour of a fully detached binary with the CP2 primary due to weak observational support. The δ Sct pulsators in eclipsing Algol-type semi-detached systems (oEA stars) exhibit characteristics similar to those of classical δ Sct stars, yet their evolutionary status differs markedly due to mass transfer between components (Mkrtichian et al. 2002). In systems with large orbital inclinations and no eclipses, these pulsators can be difficult to distinguish from classical δ Sct stars photometrically. They may instead be classified by the radial velocities and the pronounced variations in their spectral line profiles, which arise from the non-stationary nature of mass transfer and the presence of hot regions that formed by the interaction of the gas stream with the stellar atmosphere. The ongoing mass transfer, regulated by magnetic activity cycles of the Roche-lobe–filling late-type component, exerts a significant influence on the pulsational spectrum (Lehmann et al. 2020; Mkrtichian et al. 2022).

Motivated by the growing interest in chemically peculiar stars with δ Sct-type pulsations and by the lack of magnetic and asteroseismic analyses of HD 99458 in the literature, we carried out a dedicated study. The main goals are to verify the CP2 status of the pulsating primary, detect its magnetic field, and revise the physical picture of the system.

The paper is structured as follows. Sect. 2 describes the data acquisition and reduction. Sect. 3 presents the revised properties of the system and its components. We place the individual findings in context and discuss them in Sect. 4. Supporting material is presented in the Appendices.

2. Data acquisition and reduction

The discovery of multi-mode stellar oscillations with a dominant frequency of $19.2\,\mathrm{d}^{-1}$, typical of δ Sct-type variables, was reported by Skarka et al. (2019) for HD 99458 as the result of the analysis of the Kepler K2 observations (Howell et al. 2014). For the current study, we used multicolour ground-based observations of the star, which were conducted in early 2019 but not included in the original publication, and retrieved new high-precision data from the Transiting Exoplanet Survey Satellite (TESS; Ricker et al. 2015). The original Kepler K2 observations were also revised for consistency.

2.1. Photometric observations from the ground

The dedicated observations of HD 99458 were carried out in five photometric filters (Johnson B, Strömgren-Crawford vby and Δa g_2), switched cyclically, during two consecutive nights in January 2019 at the Mt. Suhora Observatory in Poland with the 0.6-m Zeiss telescope equipped with an Apogee Alta U47 detector. The short exposure time, which varied by filter from 2 s (y and B) to 20 s (v), provided a high overall data cadence.

Data reduction and differential photometry were performed using the Image Reduction and Analysis Facility (IRAF, Stetson 1987) and `Munipack` (Hroch 2014). Both packages employ classic aperture photometry. As the target field is not very crowded, this approach seems to be appropriate. To account for varying seeing conditions, several apertures were tested. For each dataset, we chose the aperture that yielded the smallest scatter in the target star's differential light curves. This criterion was always satisfied by the presence of several comparison stars. The final light curves are shown in Fig. 1.

The excellent quality of the differential light curves, ensured by the relative brightness of HD 99458, unambiguously demonstrates multi-periodic pulsations of the δ Sct type. The data were further analysed using standard Fourier techniques and the Phase-Dispersion Method (PDM) implemented in the programme package `Peranso` (Paunzen & Vanmunster 2016). At this stage, we found a broad set of frequencies between 24

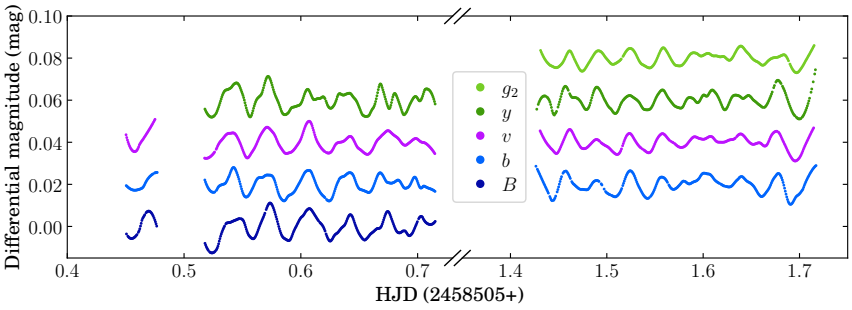


Fig. 1. Differential light curves of HD 99458 obtained in Johnson B, Strömgren-Crawford v, b, y, and $\Delta a\ g_2$ bands. An artificial vertical shift has been applied for demonstration purposes.

Table 1. Sources and characteristics of space-based photometry used in the study.

Mission	Band	Year	Data product	Cadence (s)
Kepler K2	K_p	2014	K2	1800
TESS (S45)	T	2021	TESS-SPOC	600
TESS (S46)	T	2021	TESS-SPOC	600
TESS (S72)	T	2023	TESS-SPOC	200

Table 2. Longitudinal magnetic field $\langle B_z \rangle$ of HD 99458 and the standard stars measured using SAO spectropolarimetry.

Star	BJD − 2 458 000	$\langle B_z^{COG} \rangle$ (G)	$\langle B_z^{reg} \rangle$ (G)
HD 99458	532.50040	−20 ± 115	−45 ± 60
	533.53655	190 ± 130	70 ± 60
	921.46063	−35 ± 60	15 ± 35
	922.29396	−45 ± 90	27 ± 35
Magnetic standards			
53 Cam	532.55482	2 630 ± 100	2 260 ± 60
	533.55547	3 370 ± 80	3 060 ± 40
	921.40202	1 300 ± 140	915 ± 50
α^2 CVn	922.34122	−780 ± 45	−635 ± 20
Non-magnetic standards			
o UMa	532.56329	−20 ± 5	−20 ± 5
	533.56394	−5 ± 5	0 ± 5
	921.40920	15 ± 5	−20 ± 5
HD 33256	922.18476	15 ± 15	5 ± 5

and 32 d^{-1}, clearly incompatible with the 19–22 d^{-1} range reported earlier. This apparent discrepancy originates from the Nyquist limit for the K2 data. The frequencies reported by Skarka et al. (2019) are mirrored (reflected) at the Nyquist frequency and must therefore be interpreted in the super-Nyquist regime (Chaplin et al. 2014).

2.2. Space-based observations and their phenomenological modelling

Our thorough analysis of the photometric behaviour of HD 99458 is based on a set of observations obtained from the Kepler K2 and TESS missions between 2014 and 2023. The Pre-search Data Conditioning Simple Aperture Photometry (PDCSAP) light curves were downloaded using `Lightkurve` (Lightkurve Collaboration et al. 2018). The K2 light curve consists of 3552 data points with a median uncertainty of 1.1 mmag. The three TESS sectors (45, 46, and 72), hereafter denoted S45, S46, and S72, yielded 17 501 photometric measurements with a median uncertainty of 0.85 mmag. Table 1 gives details about the individual light curves used in this study.

One of us (Z.M.) constructed a three-component phenomenological model of the investigated object that accurately describes the observed changes to within a few tenths of mmag and removes all aperiodic instrumental deformations of the light curve. The model's complexity is illustrated in Fig. 2, which shows a five-day segment of the TESS light curve from sector 72, together with its fit, which accounts for eclipses, multimode δ Sct pulsations, and variability attributed to spots.

2.3. Spectropolarimetry and échelle spectroscopy of HD 99458

2.3.1. Spectropolarimetry

Four observations of HD 99458 were obtained with the 6-m telescope of the Special Astrophysical Observatory of the Russian Academy of Sciences (SAO RAS). Spectra of the target star and four standards were acquired using the Main Stellar Spectrograph (MSS) equipped with the circular polarisation analyser (Chountonov (2004); Panchuk et al. (2014)). Data were acquired and reduced following the standard procedure described by Semenko et al. (2022). The extracted, calibrated, and continuum-normalised spectra cover the range 442.4–497.9 nm with an average resolving power of $R = \lambda/\Delta\lambda = 15\,000$. The signal-to-noise (S/N) ratio at 455 nm is 150–170 for HD 99458 and 300–700 for the standard stars.

The longitudinal magnetic field $\langle B_z \rangle$, which represents the line-of-sight component averaged over the visible stellar disc, was measured using two methods, detailed in Semenko et al. (2022). The results are summarised in Table 2, where the indices 'COG' and 'reg' denote the centre-of-gravity and regression method, respectively.

Between June 11th and June 15th 2020, five Stokes V observations of HD 99458 were acquired with the Echelle Spectropolarimetric Device for the Observation of Stars (ESPaDOnS; Donati et al. 1997), a high-resolution (R = 65 000) échelle spectropolarimeter at the Canada-France-Hawaii Telescope (CFHT). The data cover the range 370–1050 nm across 40 spectral orders. Each spectropolarimetric sequence consists of four subexposures obtained with different orientations of the polarisation optics, yielding four unpolarised (Stokes I) spectra, one circularly polarised (Stokes V) spectrum, and two null N spectra. The N spectra are acquired by combining the beams so that the intrinsic polarisation of the source cancels out, thereby providing both an independent measurement of the noise and a diagnos-

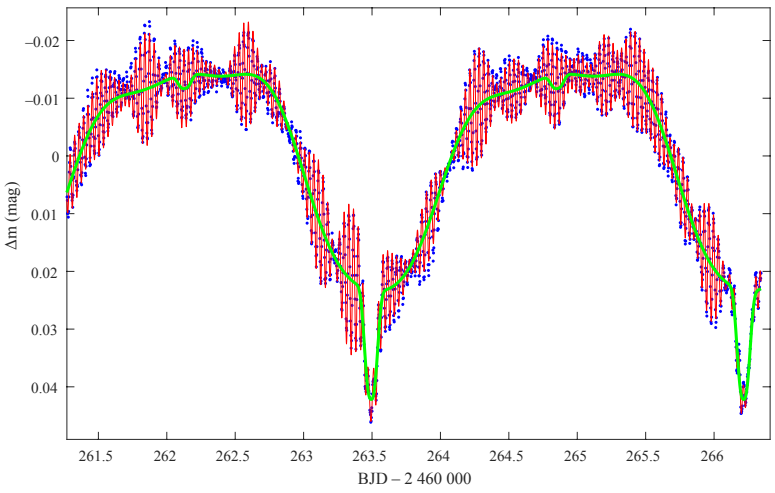


Fig. 2. Enlarged view of a five-day segment of the TESS light curve of HD 99458. The individual measurements are shown as blue points. The phenomenological model consists of the multi-periodic δ Sct pulsations shown as a red line and a combination of eclipses and a variable flux contribution of a bright spot on the surface of the primary component shown as a green line.

Table 3. Log of ESPaDOnS observations and results of the magnetic analysis.

BJD − 2 459 000	V_r (km s^{-1})	$\langle B_z \rangle$ (G)	$\langle N_z \rangle$ (G)
11.74414	2.2	19.4 ± 11.5	1.0 ± 11.5
12.74320	39.3	−11.9 ± 14.4	5.1 ± 14.4
13.74345	51.8	−21.8 ± 11.3	−13.0 ± 11.3
14.74375	−3.2	9.2 ± 11.6	12.9 ± 11.6
15.74368	59.0	18.2 ± 13.4	−0.1 ± 13.4

tic to ensure normal instrument operation. The characteristics of ESPaDOnS and data reduction steps were described in detail by Wade et al. (2016).

The ESPaDOnS observation log is given in Table 3. Each observation had a sub-exposure time of 430 s (total exposure time of 1720 s), yielding a mean peak S/N per spectral pixel of 412, with minimum and maximum S/N values of 366 and 441. Order-by-order normalisation was performed by fitting polynomial splines to continuum pixels in each spectral order.

In order to measure the magnetic field with the best possible S/N, least-squares deconvolution (LSD; Donati et al. 1997) mean line profiles were extracted using the `iLSD` package (Kochukhov et al. 2010a). LSD profiles are extracted by combining a line mask (delta functions at the laboratory wavelengths of the lines expected in the stellar spectrum, with corresponding depths and Landé factors) with the observed spectrum. The line mask was obtained from the Vienna Atomic Line Database (VALD3; Piskunov et al. 1995; Ryabchikova et al. 1997; Kupka et al. 1999, 2000; Ryabchikova et al. 2015) using an 'extract stellar' request for $T_{\rm eff}$ = 7 600 K, $\log g$ = 3.6, and solar metallicity. Following the procedure described by Shultz et al. (2018), the line mask was then cleaned by removing all hydrogen lines, lines blended with the pressure-broadened wings of hydrogen lines, and lines blended with interstellar or telluric lines, in order to ensure that the LSD Stokes I and V profiles are extracted from a set of lines with relatively similar profiles. The line mask was then 'tweaked' by adjusting the line depths to match the depths of the observed lines. Of the 8209 lines in the initial mask, 5685 lines remained for the analysis. The resulting LSD profiles are shown in Fig. 3, where

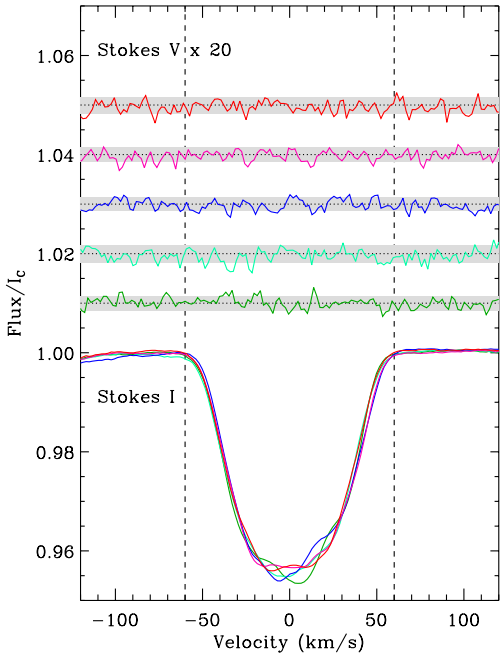


Fig. 3. LSD Stokes I (bottom) and Stokes V (top) profiles of HD 99458, where the latter profiles have been vertically shifted and amplified by a factor of 20. The LSD profiles are shown in the stellar rest frame. Grey-shaded regions indicate the mean uncertainty in Stokes V. The vertical dashed lines mark the integration range used to calculate the false alarm probability and $\langle B_z \rangle$.

the profiles have been shifted to the rest frame of the primary. Line-profile variations due to pulsations are clearly visible in the Stokes I profile.

The strength of the magnetic field was measured using $\langle B_z \rangle$ via the centre-of-gravity method (e.g. Mathys 1989; Wade et al. 2000). These measurements are given in Table 3, along with $\langle N_z \rangle$ (i.e. the centre-of-gravity measurement applied to the N spectrum). The mean uncertainty of the measurements is 12.4 G.

2.3.2. Échelle spectroscopy

The original paper by Skarka et al. (2019) reported HD 99458 as a δ Sct-type pulsator and simultaneously recognised it as a CP2 star according to the classification introduced by Preston (1974) based on measured individual abundances. Both types of stars are characterised by distinct patterns of line-profile variability (LPV), which rarely occur in the same object. To study the LPV and to quantitatively re-evaluate the photospheric composition of HD 99458, we utilised échelle spectra obtained in 2019–2026 using the instruments listed in Table 4.

A total of nine high-resolution spectra with exposure times ranging from 600 to 1400 s were obtained with the High Efficiency and Resolution Mercator Echelle Spectrograph (HERMES) in March 2019. On two occasions, observations were performed in time-resolved mode with a fixed exposure time $T_{\rm exp}$ = 300 s, yielding 25 spectra in total. A ThArNe lamp was used as a wavelength reference close to the time of the science exposure. The data were reduced with the instrument-specific pipeline (Raskin et al. 2011). The extracted spectra were normalised to the continuum using low-order polynomial fits.

We obtained 394 spectra over 15 observing runs, including seven intra-night time series, with the Medium-Resolution Echelle Spectrograph (MRES) on the 2.4-m Thai National Telescope at Doi Inthanon from 2020 to 2026. Data reduction was performed using the `PyYAP` pipeline[1] written in Python. The wavelength-calibrated spectra were normalised to the continuum level using custom scripts.

We carried out seven runs of high-resolution time-resolved spectroscopy in June–July 2025 using the Whoppshel instrument on the 1.5-m telescope at the Georgian National Astrophysical Observatory in Abastumani, Georgia. These observations produced a total of 90 spectra. The raw data were reduced following the same procedure as for MRES.

We obtained one night of time-resolved spectroscopy of HD 99458 in 2025 with the high-resolution échelle spectrograph PLATOSpec at the 1.52-m telescope at La Silla in Chile, formerly operated by the European Southern Observatory (ESO). Data reduction was performed using standard procedures in IRAF.

Table A.1 presents an observational log, grouped by instrument. The columns list the barycentric Julian date (BJD), exposure time $T_{\rm exp}$, signal-to-noise ratio S/N, measured radial velocity $V_{\rm r}$, and projected rotational velocity $\upsilon \sin i$.

The radial and rotational velocities of HD 99458 were derived by fitting a rotation profile function $G(\lambda)$, as defined in (Gray 2008), to the LSD profiles extracted using the mask described in Sect. 2.3.1. The same procedure was also applied to the original spectra from Skarka et al. (2019). The new values of $V_{\rm r}$ are listed in Table A.2. Although our approach to measuring $V_{\rm r}$ is less sensitive to deformations of the line profiles than, e.g., Gaussian profile fitting, the results are still significantly affected by LPV (Fig. 3). The mean rotational velocity $\langle \upsilon \sin i \rangle$ of the star obtained across all observations is 49.9 ± 2.0 km s^{-1}.

2.4. Speckle interferometry

Speckle interferometric observations of HD 99458 were obtained with the 6-m telescope of SAO RAS on 27 May 2024 (Maksimov et al. 2009). Three imaging series were recorded using filters with the central wavelength and bandpass combinations of 550/50, 700/50, and 900/80 nm. Each series contains 2 000 frames with exposure times ranging from 20 ms for the 550 and 700 nm filters to 60 ms for the 900 nm filter.

[1] Available at `https://github.com/ich-heisse-eugene/PyYAP`

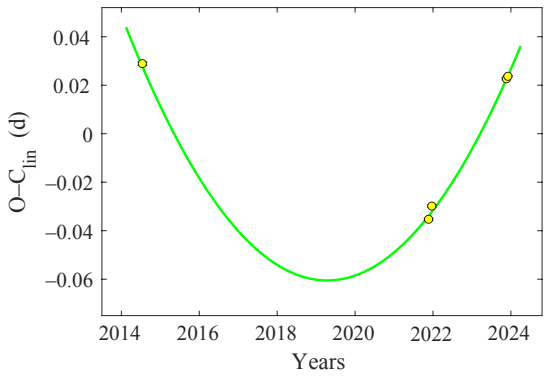


Fig. 4. Virtual O−C diagram for the centre of the primary eclipse with respect to the linear ephemeris given by the reference epoch M_0 and the period P_0.

3. Revised characteristics of HD 99458

The volume and quality of the observational material collected in our study allow us to reappraise the status of HD 99458 as a pulsating, chemically peculiar A-type star in an eclipsing binary system. Furthermore, extensive asteroseismic modelling of the pulsating δ Sct component is used to verify the consistency of the analysis.

3.1. HD 99458 as a system of stars

In the following sections, we develop a physical model for the stellar system HD 99458. We begin with a phenomenological description of the eclipses, as an incomplete or inaccurate accounting of them can compromise the interpretation of all subsequent results.

3.1.1. Phenomenological model of eclipses

The most stable and strictly periodic components of the observed light curve are the primary and secondary eclipses produced by the binary components, which orbit each other in relatively circular orbits. The shape of the eclipses and their depths remain constant throughout the observation period. Both eclipses can be described satisfactorily by a simple phenomenological model $F(\vartheta)$ proposed by Mikulášek (2015) and expressed as

$$F(\vartheta, A_{1,2}, d_{\rm e}, c_2, \Gamma) = A_1 \left\{1 - \left[1 - \exp\left(1 - \cosh\left(\frac{\varphi_1}{d_{\rm e}}\right)\right)\right]^{\Gamma_1}\right\} + A_2 \left\{1 - \left[1 - \exp\left(1 - \cosh\left(\frac{\varphi_2}{d_{\rm e}}\right)\right)\right]^{\Gamma_2}\right\}. \quad (1)$$

In the model, the dimensionless phase function $\vartheta(t)$ is the sum of the integer epoch E and the fractional phase φ (for details, see Mikulášek et al. 2008), the parameter $d_{\rm e}$ is proportional to the duration of each eclipse, and the dimensionless parameters $\Gamma_{1,2}$ describe the profile of the eclipses. The arbitrary phases φ_1 and φ_2 are defined as

$$\varphi_1 = \vartheta - \text{round}(\vartheta); \quad \varphi_2 = (\vartheta - c_2) - \text{round}\,[(\vartheta - c_2)]\,, \quad (2)$$

Table 4. List of the échelle spectrographs used in this study.

Device	Telescope	Wavelength range (Å)	Resolving power $R = \lambda/\Delta\lambda$	Reference
HERMES	1.2-m Mercator (Spain)	3 765–9 000	85 000	Raskin et al. (2011)
MRES	2.4-m TNT (Thailand)	4 200–10 050	15 000 (pre-2025)	
		3 710–10 050	18 000 (post-2025)	
ESPaDOnS	3.6-m CFHT (Hawaii, USA)	3 700–10 050	65 000	Donati et al. (1997)
PLATOSpec	1.5-m ESO telescope (Chile)	3 947–7 200	70 000	Kabáth et al. (2026)
Whoppshel	1.5-m ASA AZ1500 (Georgia)	4 000–7 500	33 000	Chargeishvili (2024)

Table 5. Amplitudes of eclipse minima.

Filter	$\lambda_{\rm eff}$ (Å)	A_1 (mag)	A_2 (mag)
$K_{\rm p}$	5500	0.01848(17)	0.00191(16)
T	8900	0.01874(7)	0.00244(6)

Notes. The depth of the primary minimum A_1 shows no dependence on the effective wavelength $\lambda_{\rm eff}$, whereas the secondary minimum A_2 appears deeper in the T band.

Table 6. Times of eclipse minima and corresponding O–C values derived from photometry.

E	O−2400000 BJD	O−$C_{\rm lin}$ (d)	O−$C_{\rm sqr}$ (d)	$O_{\rm II}$-$C_{\rm II\,sqr}$ (d)	Source
−1013	56 852.8756	0.0289	0.0012(7)	0.0060(32)	K2
−27	59 536.6707	−0.0353	−0.0013(5)	0.0004(19)	TESS S45
−16	59 566.6178	−0.0298	0.0024(4)	0.0019(18)	TESS S46
241	60 266.2157	0.0226	0.0002(4)	−0.0006(18)	TESS S72a
246	60 279.8266	0.0237	−0.0001(4)	−0.0019(17)	TESS S72b

Notes. E is the epoch number; O and $O_{\rm II}$ denote the observed times of the primary and secondary minima, respectively; $C_{\rm lin}$ and $C_{\rm sqr}$ are the calculated primary-minimum times from the linear and quadratic ephemerides, respectively, while $C_{\rm II\,sqr}$ is the calculated secondary-minimum time from the quadratic ephemeris. All calculated times are obtained from relations (3) and (4) with $\vartheta = E$ (or $\vartheta = E + 0.5$ for the secondary minimum). Uncertainties of the residuals are given in parentheses. The last column lists the photometric data sources.

where c_2 is the phase of the centre of the secondary eclipse, and the phase of the primary eclipse centre is put at zero. The depths A_1 and A_2 of the primary and secondary eclipses may vary over time.

The best-fit model describing eclipses in HD 99458 has the following parameters: $d_{\rm e} = 0.014\,61(8)$, $\Gamma_1 = \Gamma_2 = \Gamma = 1.354(3)$, $c_2 = 0.499\,6(3)$. As c_2 is nearly equal to 0.5, the orbit of the eclipsing binary is probably circular. The value of the parameter Γ, which is equal for both eclipses, suggests that the inclination angle is markedly different from 90 degrees, so the eclipses are very likely partial. These phenomenological conclusions are consistent with the physical solution of the eclipsing binary presented in Skarka et al. (2019).

The analysis of the course of the phase function $\vartheta(t)$ and the virtual O−C diagram for HD 99458 (Fig. 4), performed in the same manner as in Semenko et al. (2024), clearly shows the presence of a quadratic term in $\vartheta(t)$, indicating approximately linear growth of the period $P(t)$ during the observed interval. More explicitly,

$$\vartheta_0 = \frac{t - M_0}{P_0}; \quad \vartheta = \vartheta_0 - \tfrac{1}{2}\dot{P}\,(\vartheta_0 - \eta_2)\,(\vartheta_0 - \eta_3), \tag{3}$$

$$t_{\rm C}(\vartheta) = M_0 + P_0\,\vartheta + \tfrac{1}{2}\dot{P}\,P_0\,(\vartheta - \eta_2)\,(\vartheta - \eta_3), \tag{4}$$

$$P(t) = \dot{\vartheta}^{-1} = P_0\left\{1 + \dot{P}\left[\vartheta_0(t) - \tfrac{1}{2}(\eta_2 + \eta_3)\right]\right\}, \tag{5}$$

where parameters $\eta_2 = 150.8$ and $\eta_3 = -903.8$ ensure the orthogonality of the relations (3–4), $P_0 = 2\overset{\rm d}{.}721\,966\,9(3)$, $M_0 = 2\,459\,610.199\,08(10)$, $\dot{P} = 1.599(6) \times 10^{-7} = 5.045(18)\ {\rm s\,yr^{-1}}$.

The extremely smooth shape of the O−C diagram points to the possible extrinsic nature of the observed change in the orbital period. This could be due to either additional bodies in the system or a precession of the orbital plane on a timescale of dozens of years.

We paid special attention to the possible temporal development of the parameters describing the primary and secondary eclipses, in particular to the changes in the depth and the phase of the secondary minimum compared to the primary minimum. The analysis confirmed that the depth of the primary minimum A_1 (see equation (1)) remains constant within the modelling uncertainties of the observed light curve to an accuracy of a few per cent. Likewise, the position of the secondary minimum relative to that of the primary does not change, as finally indicated by the fifth column of Table 6. The eccentricity of the binary orbit apparently tends to zero.

3.1.2. Spectroscopic orbit

Fitting the new $V_{\rm r}$ dataset with the orbital solution presented by Skarka et al. (2019) revealed a systematic phase offset between the observations and the model. This discrepancy may stem from an increasing orbital period ($P_{\rm orb}$), as discussed in the previous section, or from the evolving argument of periastron (ω). However, the latter, known as apsidal motion, appears unlikely when applied to HD 99458 given its circular orbit.

To revise the orbital solution, we used the extended $V_{\rm r}$ dataset from Table A.1 using the `rvfit` code (Iglesias-Marzoa et al. 2015a,b). While the spectrum of the secondary is generally difficult to detect, we were able to identify a single Fe I 8824.219 Å line in which the contributions of both components are clearly discernible (Fig. 5). By measuring the five most visible profiles, we obtained the secondary's radial velocity, which varied over the course of one night from 140 to 155 km s^{-1} with an uncertainty of 10–20 km s^{-1}, thereby identifying the system as an SB2 binary. The best-fitting parameters of the system are presented in Table 7, and the corresponding $V_{\rm r}$ fits for each component are shown in Fig. 6.

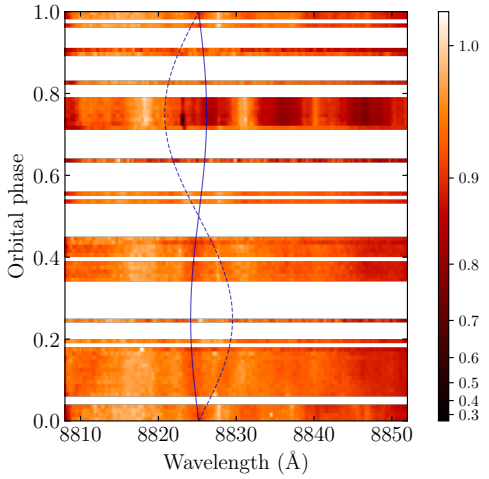


Fig. 5. Dynamic spectra showing the Fe I 8824.219 Å line in the two components of HD 99458. Radial velocity variations are shown by the solid line for the primary component and the dashed line for the secondary.

Table 7. Revised orbital elements for HD 99458.

Parameter	Value
T_p	2 456 814.492 89 ± 0.000 68
P (days)	2.722 172 ± 0.000 001
e	0.0 (fixed)
γ (km s^{-1})	32.38 ± 0.02
K_1 (km s^{-1})	34.94 ± 0.03
K_2 (km s^{-1})	147.6 ± 4.2
$M_1 \sin^3 i$ ($M_\odot$)	1.39 ± 0.10
$M_2 \sin^3 i$ ($M_\odot$)	0.33 ± 0.01
q (M_2/M_1)	0.24 ± 0.01
$a \sin i$ ($R_\odot$)	9.82 ± 0.22
RMS$_1$ V_r (km s^{-1})	1.4
RMS$_2$ V_r (km s^{-1})	11.5

The orbital period we derived from spectroscopy is 10.9 s longer than that published by Skarka et al. (2019). However, the observed difference is only about one-third of that expected between the two average observational epochs, given the rate $\dot{P}$ measured via eclipse timing. This apparent discrepancy, while broadly consistent with a variable orbital period, may result from the limited time span and quality of the data used in the 2019 study or from the pulsation-induced scatter in the measured radial velocities. We return to this problem in Sect. 4.

3.1.3. Physical model of eclipses

We utilised the TESS light curves, cleaned of the pulsation using our phenomenological model of photometric variability, to build a physical model of the binary system HD 99458. For this, we employed two codes: the PHysics Of Eclipsing BinariEs (`PHOEBE`; Prša & Zwitter 2005) and the Eclipsing binary Learning and Interactive System (`ELISa`; Čokina et al. 2021). `PHOEBE` was used solely to fit eclipses, ignoring out-of-eclipse

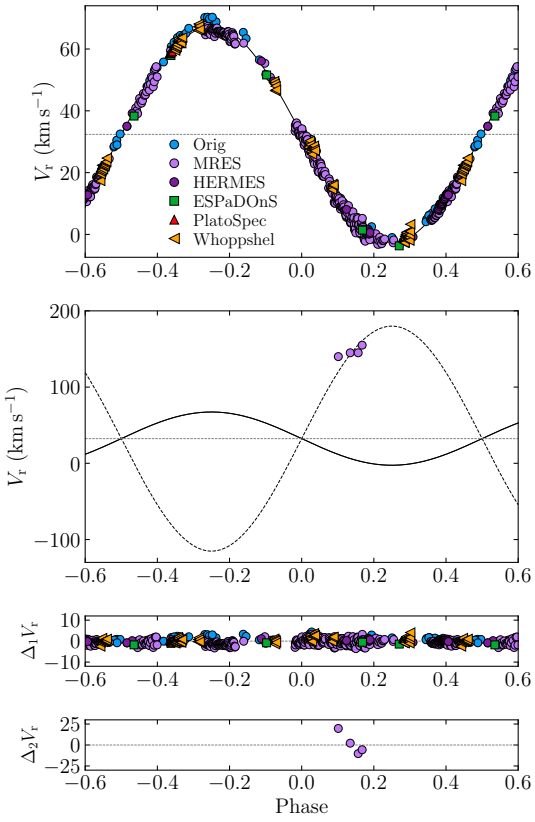


Fig. 6. From top to bottom: Measured radial velocities of the primary (panel 1) and secondary (panel 2) components, phased with an orbital period of 2^d.722 172. The best-fitting orbital solution is shown as the solid and dashed lines for the primary and secondary components, respectively. The horizontal dashed lines in both panels indicate the systemic velocity γ. Panels 3 and 4 show the corresponding residuals. The measurements labelled as 'Orig.' are listed in Table A.2 and were derived from the spectra used by Skarka et al. (2019).

variability (Fig. 7). For the model fitting, we utilised the differential corrections method. The modelling in `ELISa` included an MCMC-based uncertainty analysis. The optimisation proceeded through successive releases of the free parameters. This approach was chosen to reduce degeneracies between orbital and stellar-surface parameters during sampling. The mass priors were tied to independent constraints. The mass of the primary component was anchored to the asteroseismic value of $M_1 \approx 1.9\,M_\odot$ (Sect. 3.4). The secondary-mass bounds were derived from the K_1 value and the mass function, propagated across a plausible inclination interval. Under these constraints, we estimated inclination, masses and effective temperatures. The final models included configurations with both two fixed spots and two to three spots with free latitude. The spots were located on the primary component. Each spot was parametrised by longitude, latitude, angular radius, and the temperature factor. Table 8 summarises the modelling with both codes used. The posterior medians and 68% credible intervals are provided only for the five principal detached solutions obtained using the `ELISa` code.

In comparison to the results presented by Skarka et al. (2019), our final model is characterised by a slightly smaller mass ($1.8\,M_\odot$ vs $2.15\,M_\odot$) and a substantially smaller radius (2.3–$2.8\,R_\odot$ vs $3.47\,R_\odot$) of the primary. The most important difference is that the radius of the secondary star is larger, revised from 0.59 to 2.6–$2.8\,R_\odot$. Introducing an inflated secondary reduces the

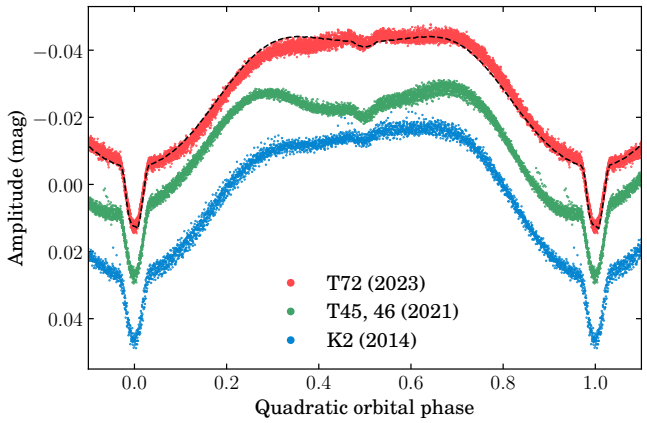


Fig. 7. Eclipse light curves in K2 and TESS data shifted vertically for clarity. The black dashed line shows the PHOEBE model fit without spots.

angle i by about 10° from the originally reported 73.2°. These changes make the secondary component fill its Roche lobe and provide the best overall agreement with the observations. The spots on the stellar surface that we used in the modelling with the ELISa code do not significantly improve the fit.

3.1.4. Potential third body

A gravitational perturbation from a third body could explain the observed variation in the orbital period of HD 99458. We used speckle interferometry to search for a potential close-in companion.

Fig. 8 presents the speckle-interferometric detection limits as a function of angular separation ρ and magnitude difference Δm for potential companions. In the analysis of the autocorrelation functions and power spectra of the speckle-interferometric data series, we find no clear evidence of additional components. Yet we cannot completely rule out a hypothetical third body, as the power spectra near the resolving limit of the 6-m telescope in the 700 and 900 nm filters appear asymmetric. This effect may result from an incomplete compensation of atmospheric dispersion at zenith distances $z > 60°$. In this range of z, the atmospheric dispersion compensator of our instrument becomes less effective. The observations of HD 99458 through the 550 nm filter are unaffected, as they were conducted under more favourable conditions. As the total recording time of a single series is less than 10 minutes, corresponding to a change in the zenith distance of only about 2°, the available data do not allow us to reliably distinguish between the residual effects of atmospheric dispersion and the presence of an unresolved component. Consequently, we cannot exclude a companion with $\Delta m > 2$ mag at $\lambda = 550$ nm and $\Delta m < 2$ mag in the 700 and 900 nm filters. Additional observations are necessary to obtain a more reliable result.

3.2. Reassessment of the CP status

To be classified as a CP star, HD 99458 must possess a strong globally organised magnetic field and demonstrate chemical anomalies. The presence of stable spots caused by the inhomogeneous distribution of chemical elements is another requirement. In our study, we tested the star against each of these criteria.

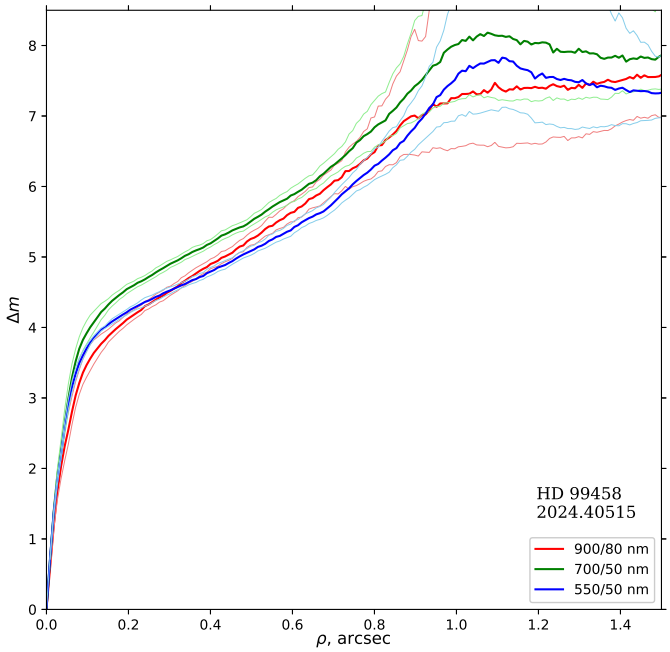


Fig. 8. Speckle-interferometric limits on the presence of additional components in HD 99458. The coloured lines show the angle-averaged limits on Δm at various distances. The semi-transparent lines mark the 1-σ uncertainty limits.

3.2.1. Magnetic field

Strong, large-scale magnetic fields are a defining characteristic of chemically peculiar A-type stars. However, Folsom et al. (2012) showed that in exceptional cases a magnetic field can be detected in very young stars with a normal composition or even with anomalies of λ Boo type. Our dedicated spectropolarimetric observations of HD 99458 made with the two spectropolarimeters showed no measurable longitudinal magnetic field.

The MSS observations place an upper limit of approximately 150 G on the longitudinal field $\langle B_z \rangle$ of HD 99458, verified by observations of two magnetic (53 Cam and α^2 CVn) and two non-magnetic (o UMa and HD 33256) standard stars. The only spurious signal was detected in the data for o UMa, although it is vanishingly small and does not affect our conclusion.

The analysis of the ESPaDOnS observations yielded a non-detection with even higher confidence due to a substantially larger number of measured lines contributing to the LSD analysis. In this case, the presence of a magnetic field was evaluated using false alarm probabilities (FAP; Donati et al. 1997), via calculation of the χ^2 statistic of Stokes V and N inside and outside of the stellar lines to the null model of zero polarisation. An FAP above 10^{-3} indicates a non-detection. All five ESPaDOnS observations are above the FAP threshold.

Fig. 9 shows $\langle B_z \rangle$ folded with the period P_0 (Sect. 3.1.1), assuming the primary's rotation is synchronised with the orbital motion. A first-order harmonic fit to the ESPaDOnS measurements yields an amplitude of 16 ± 11 G, consistent with the uncertainty in $\langle B_z \rangle$, and the reduced χ^2 is identical to that of the null model (i.e., no variation aside from noise).

To obtain a more accurate estimate of the upper limit of the global dipolar field strength, we performed a Bayesian comparison of the ESPaDOnS LSD Stokes V profiles with theoretical polarisation spectra calculated using the InversLSD code (Kochukhov et al. 2014). This software was applied to compute

Table 8. Physical solutions for the TESS light curve.

Model	$\mathcal{R}^2$	M_1 ($M_\odot$)	M_2 ($M_\odot$)	R_1 ($R_\odot$)	R_2 ($R_\odot$)	$T_{\rm eff,1}$ (K)	$T_{\rm eff,2}$ (K)	i (°)	Spot geometry
PHOEBE		1.8	0.4	2.34	2.80	7600 K (fixed)	3800 ± 100	64.4 ± 0.1	—
Spotless	0.981	$1.81^{+0.12}_{-0.07}$	$0.44^{+0.02}_{-0.02}$	2.73	2.55	7350^{+440}_{-420}	4060^{+310}_{-230}	$63.4^{+1.9}_{-1.9}$	—
1 spot	0.977	$1.85^{+0.12}_{-0.09}$	$0.44^{+0.02}_{-0.03}$	2.89	2.69	7600^{+300}_{-300}	4080^{+270}_{-240}	$62.6^{+1.8}_{-2.3}$	λ = 201°, ϕ = 89°, r = 9.4°, $T_{\rm sp}$ = 6840 K
2 spots, fixed ϕ	0.983	$1.85^{+0.12}_{-0.08}$	$0.44^{+0.02}_{-0.02}$	2.67	2.69	7750^{+180}_{-330}	3970^{+210}_{-170}	63.4 (fixed)	ϕ = 90° fixed; A: λ = 162°, r = 7.9°, $T_{\rm sp}$ = 7130 K; B: λ = 200°, r = 7.7°, $T_{\rm sp}$ = 6670 K
2 spots	0.982	$1.88^{+0.08}_{-0.11}$	$0.45^{+0.01}_{-0.02}$	2.83	2.63	7780^{+180}_{-430}	4080^{+290}_{-250}	$63.2^{+1.3}_{-1.7}$	A: λ = 193°, ϕ = 92°, r = 10.1°, $T_{\rm sp}$ = 7160 K; B: λ = 203°, ϕ = 94°, r = 8.6°, $T_{\rm sp}$ = 7240 K
3 spots	0.986	$1.86^{+0.11}_{-0.10}$	$0.45^{+0.01}_{-0.02}$	2.83	2.65	7690^{+240}_{-360}	4080^{+300}_{-250}	$62.8^{+1.9}_{-1.7}$	A: λ = 191°, ϕ = 93°, r = 8.5°, $T_{\rm sp}$ = 7380 K; B: λ = 200°, ϕ = 94°, r = 7.7°, $T_{\rm sp}$ = 7000 K; C: λ = 212°, ϕ = 93°, r = 8.6°, $T_{\rm sp}$ = 7230 K

Notes. The columns list the Bayesian $\mathcal{R}^2$ metric, the masses M_1 and M_2, the radii R_1 and R_2, and the effective temperatures $T_{\rm eff,1}$ and $T_{\rm eff,2}$ of the primary and secondary components, respectively; the inclination angle i, and the spot parameters: the radius r, longitude λ, latitude ϕ, and the temperature $T_{\rm sp}$.

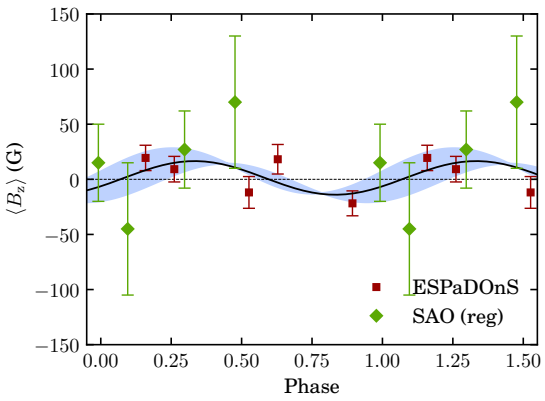


Fig. 9. ESPaDOnS and SAO $\langle B_z \rangle$ measurements phased with nominal rotation period. The black curve shows the harmonic fit to the measurements, and the shaded region indicates the associated uncertainties.

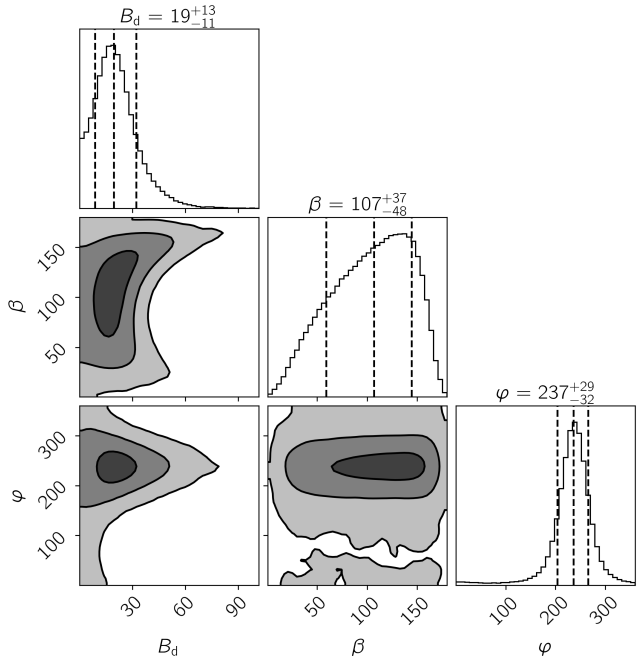


Fig. 10. Marginalised posterior probability distributions for a dipolar fit to the Stokes V LSD profiles of HD 99458. Contours correspond to 1, 2, and 3-σ confidence levels.

a library of predicted circular polarisation profiles for five rotational phases, assuming a coplanar synchronised configuration of the binary ($i_{\rm rot} = i_{\rm orb}$ and $P_{\rm rot} = P_{\rm orb}$). The Stokes V spectra were treated in the weak-field approximation (e.g. Kochukhov et al. 2010b), assuming that the LSD profile behaves as a pseudo-line with λ = 500 nm and an effective Landé factor of 1.2. The equivalent width and broadening of this line were adjusted by fitting the LSD Stokes I spectra. With these assumptions, Markov chain Monte Carlo (MCMC) sampling was applied to explore the entire parameter space $B_{\rm d}, \beta, \phi$ with the help of `SoBAT` routines written in IDL (Anfinogentov et al. 2021). A uniform prior was used for $B_{\rm d}$ and a random orientation of the dipolar field axis was implemented with uniform priors in ϕ and $\cos\beta$. The MCMC walkers were run for 10^6 steps after the initial 10^4 step burn-in. The resulting posterior distribution of the three dipolar field parameters is illustrated in Fig. 10. Formally, we find $B_{\rm d} = 19^{+13}_{-11}$ G but the statistical significance of this detection is below 2-σ. The upper limits for $B_{\rm d}$ are 32, 52, and 81 G for the 1, 2, and 3-σ confidence levels, respectively. Thus, any magnetic field possessed by the star must be in the 'ultra-weak' regime occupied by stars such as Vega or Alhena (e.g. Blazère et al. 2020), as it is certainly below the 300 G lower limit for magnetic Ap stars found by Aurière et al. (2007) and Sikora et al. (2019).

3.2.2. Abundance analysis

HD 99458 was recognised by Skarka et al. (2019) as a chemically peculiar object. The anomalous elemental abundances are the hallmark of this class of stars.

We used the IDL-based version of Spectroscopy Made Easy (SME) (Valenti & Piskunov 1996, 2012; Piskunov & Valenti 2017) to fit the HERMES spectra of HD 99458. From the set of atmospheric models distributed with SME, we utilised the grid of `LLmodels` (Shulyak et al. 2004) as the most suitable for A-type stars. The atomic line parameters were extracted from VALD3 in accordance with the preliminary effective temperature $T_{\rm eff}$ and surface gravity $\log g$ of the star.

First, we verified the stellar parameters $T_{\rm eff} = 7600$ K and $\log g = 3.6$ reported by Skarka et al. (2019). Spectrum synthesis of the first three Balmer lines and a 100 nm region centred at 520 nm showed mostly satisfactory agreement with the observations. Thus, we decided to use the originally published values for $T_{\rm eff}$ and $\log g$ throughout this study. The only visible exception, where the fit did not match the observed profiles, is H_α. This line demonstrates strong variability across spectra obtained at different epochs. While such variability is not expected from the main A-type star, it appears consistent with emission from a cool and active companion. Apart from H_α and the near-IR Fe I line used in Sect. 3.1.2, we have identified a few spectral features, described in Sect. 3.2.3, which are potentially attributable to the companion star. However, none of these findings allows us to infer the physical parameters or chemical composition of the secondary from the spectra. Moreover, the lines of the hot primary component completely dominate in the visible spectrum, so that we can effectively treat the star as single-lined in the abundance analysis.

After the preliminary phase, we evaluated the microturbulent velocity $\xi_{\rm micro} = 2.9 \pm 0.8$ km s^{-1} and the rotational velocity $v \sin i = 47.9 \pm 0.5$ km s^{-1} by fitting the Fe I and Fe II lines. The latter parameter is in full agreement with the value found from the LSD profiles (Table A.1).

Finally, by fitting large portions of the HERMES spectra, we evaluated the atmospheric chemical composition of HD 99458. The goodness of fit is demonstrated in Fig. 11. Table 9 lists the individual abundances of 23 species and their corresponding solar values, and Fig. 12 illustrates the relative abundance pattern. Our results show that most elements in HD 99458 are mildly depleted, in contrast to the 1 dex enrichment in Fe, Si, and Ti reported by Skarka et al. (2019).

3.2.3. Line profile variability

Given the absence of any chemical anomalies or a measurable magnetic field characteristic of CP2 stars, we can conclude that the earlier classification of HD 99458 is not supported by our analysis. However, a careful inspection of the high-resolution spectra has revealed an LPV, which can be attributed to at least two distinct mechanisms. One of these typically occurs in hot CP stars (e.g. Townsend & Owocki 2005), produces variable hydrogen lines, and, in the case of HD 99458, may indicate a magnetosphere in either component.

The H_α line exhibits significant line-profile variability in all high-S/N spectra obtained in this study. Moreover, somewhat weaker yet phase-coherent changes in H_β also persist throughout the orbital cycle. The lower resolution of MRES suppresses the fine structure of these profiles, but the spectra from this instrument provide superior phase coverage in our observations and were therefore selected to illustrate the effect of the hydrogen-line LPVs in Fig. 13. We subtracted the synthetic spectrum obtained using `SME` in Sect. 3.2.2 from the observations to examine the hydrogen-line profiles in greater detail.

In the residual spectra, both the H_α and H_β lines exhibit emission that reaches maximum strength at the approximate orbital phases of 0.1–0.2 and 0.7–0.8. These emission peaks are located at radial velocities of approximately +110 and −65 km s^{-1}. At orbital phases close to 0, 0.5, and 1, the emission profiles become nearly symmetric and double-peaked. In the PLATOSpec data, obtained near an orbital phase of 0.64, we observed intranight evolution of the absorption, with the absorption minimum centred at −220 km s^{-1}.

The H_α profiles obtained at similar orbital phases but at widely separated epochs can differ substantially, as demonstrated in Fig. 14. Given the large gaps between observations (HERMES in 2019, ESPaDOnS in 2020, and PLATOSpec in 2025), these differences suggest that the mechanism driving this

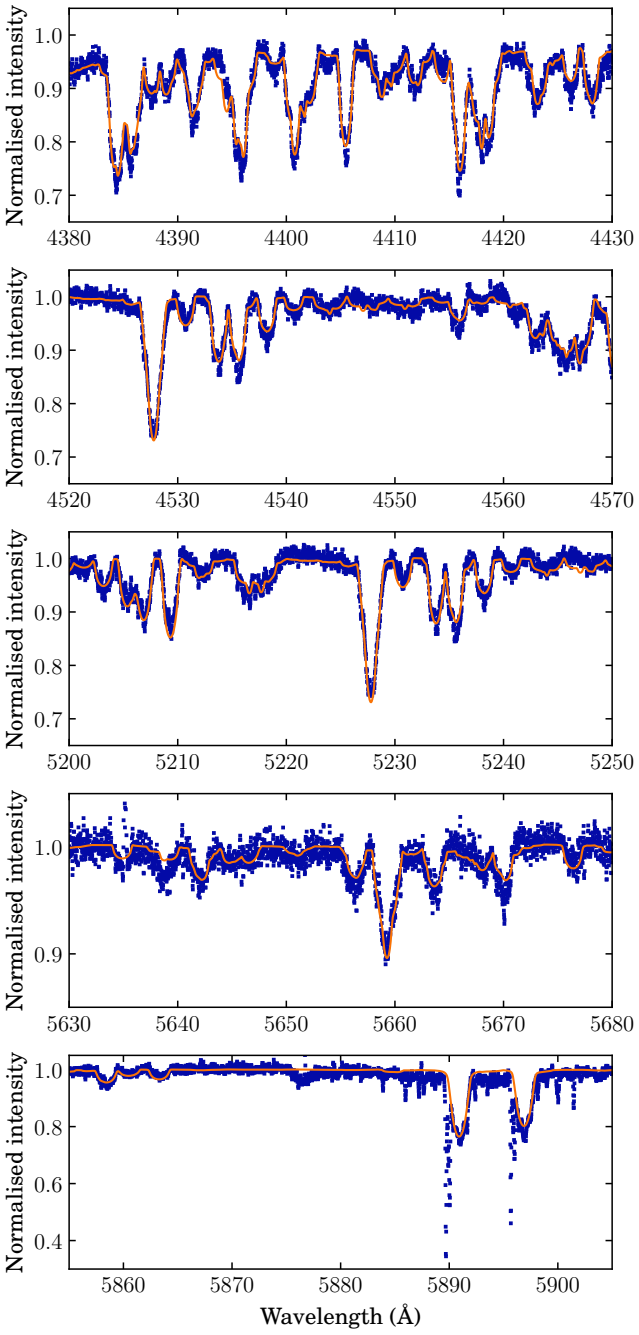


Fig. 11. Fit of a synthetic spectrum (orange) to the HERMES observations (blue).

Table 9. Atmospheric abundances ($\log N/N_{\rm tot}$) in HD 99458 together with the corresponding solar values (in parentheses).

Element and abundance	Element and abundance
C: −4.33±0.36 (−3.47)	Fe: −4.98±0.10 (−4.52)
O: −3.14 (−3.26)	Co: −7.00±0.13 (−7.09)
Na: −5.78±0.42 (−5.81)	Ni: −6.18±0.11 (−5.79)
Mg: −4.69±0.31 (−4.48)	Cu: −8.71±0.15 (−7.85)
Si: −4.89 (−4.44)	Zn: −8.07±0.25 (−7.47)
S: −5.17±0.13 (−4.91)	Y: −10.41±0.26 (−9.82)
Ca: −6.18±0.28 (−5.66)	Zr: −8.99±0.59 (−9.44)
Sc: −9.06±0.20 (−8.89)	Ba: −10.73±0.30 (−9.76)
Ti: −7.44±0.22 (−7.06)	La: −10.81 (−10.92)
V: −7.85 (−8.13)	Ce: −10.26±0.30 (−10.45)
Cr: −6.65±0.16 (−6.41)	Nd: −10.75 (−10.61)
Mn: −6.86±0.42 (−6.61)	

Notes. The uncertainties are given only for elements with a sufficient number of identified lines. The solar composition is compiled from Asplund et al. (2021) and Magg et al. (2022).

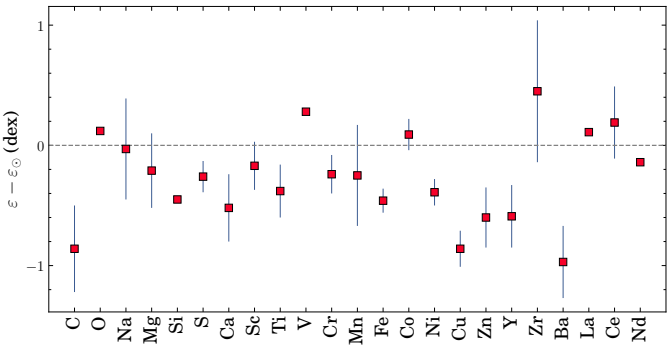


Fig. 12. Chemical composition of HD 99458 compared to the Sun.

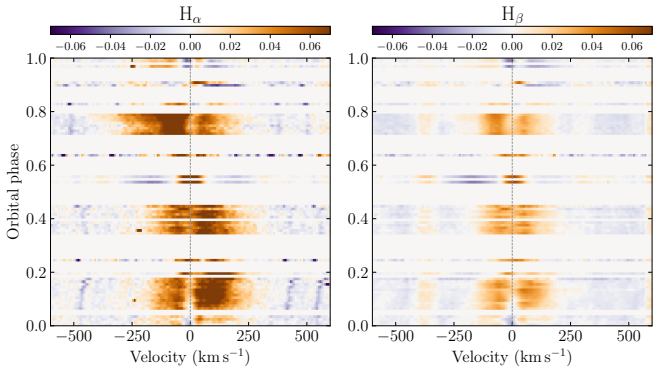


Fig. 13. Residual H_α (left) and H_β (right) profiles demonstrating LPVs as a function of orbital phase. The residuals were obtained by subtracting the synthetic spectrum from the observations. The velocity scale is given in the reference frame of the primary component.

hydrogen-line variability is not stable on multi-year timescales, and is therefore not typical of CP stars.

Our spectra contain a broad spectral feature of variable intensity that appears in the vicinity of the He I 5875 Å line in the high-S/N spectra obtained within $\pm 0.2\,\varphi_{\rm orb}$ of the primary

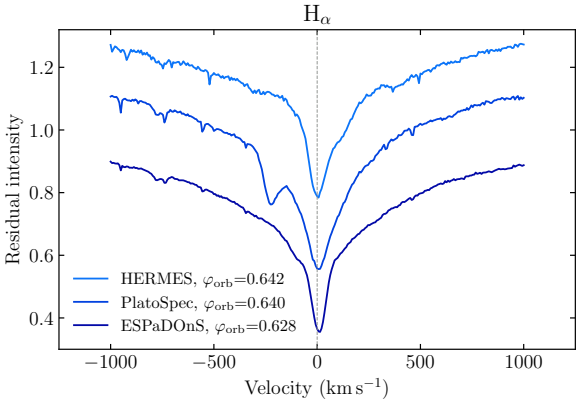


Fig. 14. Three spectral regions centred on H_α obtained at similar orbital phases. The corresponding dates are BJD 2 458 547.5964 (HERMES), BJD 2 459 015.7437 (ESPaDOnS), and BJD 2 460 850.526 (PLATOSpec).

eclipse (left panel of Fig. 15). The measured maximum equivalent width W_λ of this feature is 170 mÅ. With $T_{\rm eff}$=7600 K, the primary star is too cool to produce the photospheric He I 5875 Å line. Despite this, we associate this feature with helium and examine its origin in a broader context in Sect. 4.

Finally, the spectral region between the Paschen jump and 9000 Å contains multiple lines with substantially varying profiles. The most prominent feature here is the Ca II 8662 Å line (right panel of Fig. 15). Given the cool companion's contribution to this region, the variation is likely partly related to binarity. The secondary component may also be responsible for the phenomenon we observed in the data at BJD 2 461 071. In these observations, numerous absorptions developed rapidly over a timescale of ∼30 minutes. These absorptions appear as broadened lines with irregular and often asymmetric profiles. Fig. 16 illustrates this effect. To identify the lines, we compared the observations with two synthetic spectra computed for $T_{\rm eff}$= 7600 K (primary) and ≈ 4500 K (secondary). The comparison suggests that the observed absorptions are most likely abnormally enhanced high-excitation-potential ($\chi > 2$ eV) Fe I lines belonging to the secondary star, shifted by $\simeq +200$ km s^{-1} from the rest position. All identified features have similarly broadened asymmetric profiles with a typical $W_\lambda \approx 1$ Å. The results of the tentative identification are labelled as '(A)' in Fig. 16. For comparison, we also show several reference lines of the primary component. A possible explanation of this phenomenon is discussed in Sect. 4.

3.2.4. Model of spot variability

The main and most controversial part of the phenomenological model of photometric variability is the residual after subtraction of eclipses (Sect. 3.1.1) and pulsations (Sect. 3.3.1). It manifests as a periodic, asymmetric modulation of the system brightness, characterised by a phase curve that evolves with time. Formally, this signal can be approximated by a fourth-order harmonic polynomial with time-varying parameters. An alternative, more physically intuitive description represents this variability as a linear combination of three symmetric bright (warmer) surface spots with fluctuating intensities located near quadratic phases 0.3, 0.5, and 0.7 (Fig. 17). The corresponding phenomenological

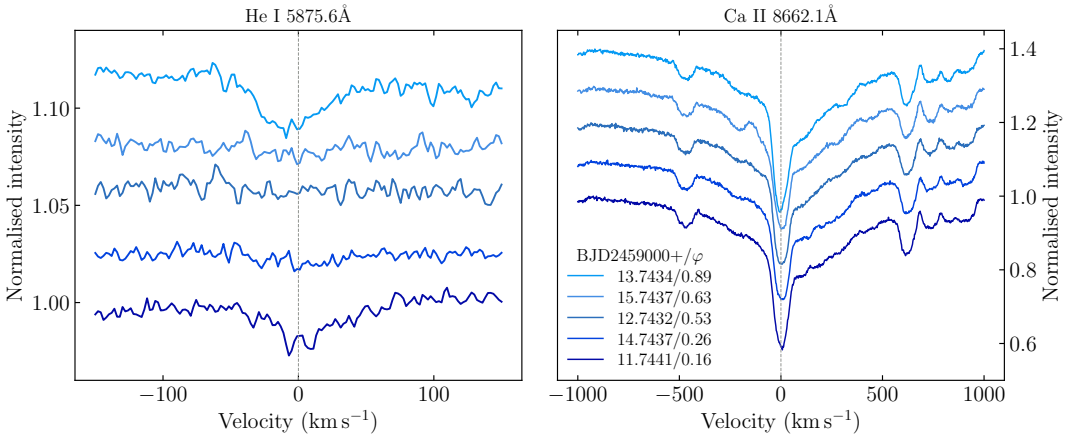


Fig. 15. Two spectral regions centred on He I 5875 Å (left) and Ca II 8662 Å (right), showing LPVs with orbital phase φ. The velocity scale is corrected for orbital motion.

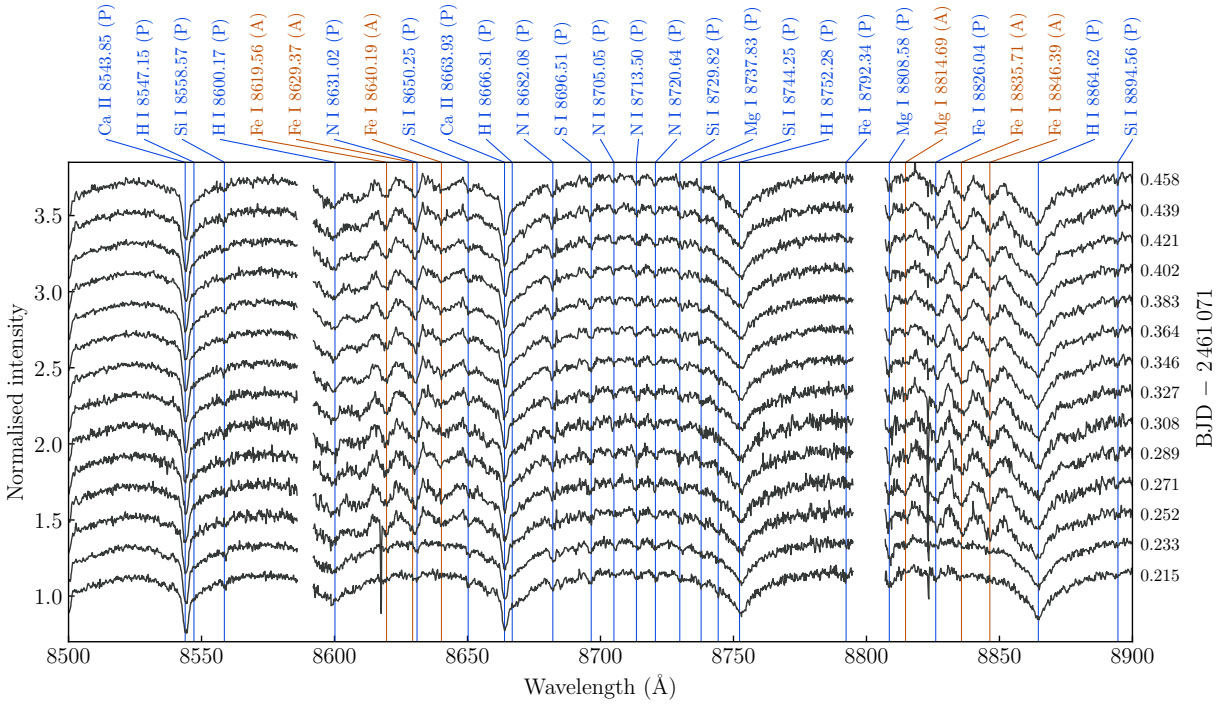


Fig. 16. Selected series of spectra demonstrating rapid spectral variability resulting in additional absorption features. The absorptions and their tentative identification are labelled with '(A)'. The lines of the primary component are denoted in the same manner with '(P)'.

model is

$$F_{\rm s}(\vartheta, B, d, \varphi_0) = \sum_{i=1}^{3} B_i(t) \left\{ \exp\left[1 - \cosh\left(\frac{\varphi_i}{d_i}\right)\right] - 2.289\, d_i \right\},$$
$$\text{where} \quad \varphi_i = (\vartheta - \varphi_{0i}) - \text{round}\,(\vartheta - \varphi_{0i}), \quad (6)$$

where φ_{0i} and d_i denote the instantaneous position and half-width of the i-th spot, respectively, and ϑ is the quadratic orbital phase defined from the eclipses. The instantaneous parameter values derived for the individual data groups are given in Table 10. From this table, one can conclude that the spot amplitudes $B_i(t)$ evolve on a timescale of about 10 days.

If our hypothesis about the spots is correct, their variability would be inconsistent with long-term stability of chemical spots observed in chemically peculiar stars (Skarka et al. 2019). Instead, such formations could represent sites of elevated temperature where, for example, accreting streams strike the stellar surface. Although the development of the spot component of the light curve appears substantial in Fig. 17, a detailed analysis of the data in Table 10 demonstrates only marginal changes in the parameters of the three identified spots. If the spots are associated with accretion onto the stellar surface, the corresponding process in HD 99458 may therefore be relatively stationary.

Detailed analysis of the phase light curves of magnetic chemically peculiar stars obtained from photometric satellite observations identifies relatively narrow brightness dips that persist in position and shape over many decades. These photometric dips are observed in the light curves of many mCP stars (e.g. Semenko et al. 2024). The most likely explanation

Table 10. Phenomenological parameters of the three bright spots.

S	φ_{01}	d_1	B_1 (mag)	φ_{02}	d_2	B_2 (mag)	φ_{03}	d_3	B_3 (mag)
K2	0.3178(20)	0.1432(13)	−0.03937(8)	0.4977(15)	0.0849(18)	−0.01105(8)	0.6755(17)	0.1376(15)	−0.04461(8)
S45, S46	0.2928(4)	0.1369(4)	−0.03665(4)	0.5153(9)	0.0806(4)	−0.01834(4)	0.6981(7)	0.1118(6)	−0.03750(5)
S72	0.3144(8)	0.1216(6)	−0.03351(4)	0.4956(7)	0.0812(4)	−0.01889(4)	0.6856(6)	0.1283(5)	−0.03772(4)
median	0.314	0.137	−0.036	0.498	0.081	−0.018	0.686	0.128	−0.038

Notes. Data sources S: Kepler K2, TESS S45, S46, and S72. The parameters φ_{0j}, d_j, and B_j, where $j = 1, 2, 3$, denote the central phase, half-width, and amplitude of the jth spot, respectively. Sizes of individual spots vary on timescales of 10–20 days.

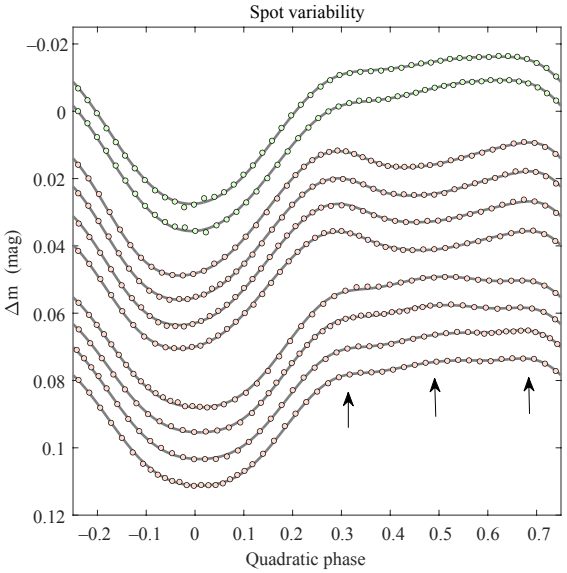


Fig. 17. Long-term evolution of the HD 99458 light curve after removing eclipses and δ Sct pulsations. The phase curves derived from K2 (2 curves), TESS S45 and S46 (2 curves each), and S72 (4 curves) can be interpreted as evidence of three hot surface spots located at phases 0.3, 0.5, and 0.7, each with a variable amplitude. The phenomenological model is defined by the relation (6).

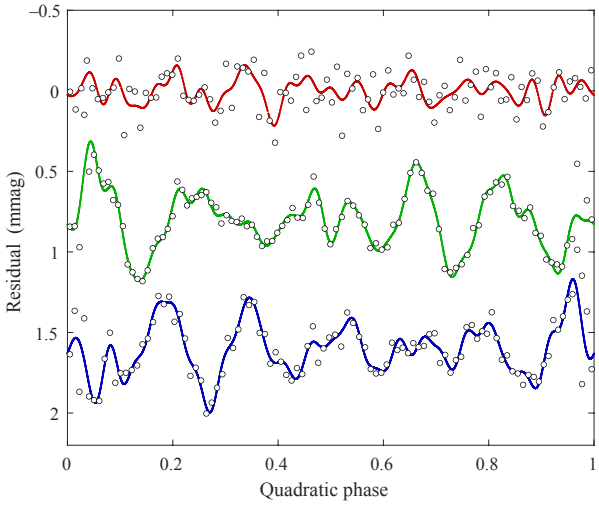


Fig. 18. Light curves shown relative to the quadratic ephemeris and corrected for occultations, trends, spot variability, and pulsations still exhibit residual variability with amplitudes up to 1 mmag. Red, green, and blue lines correspond to the K2, TESS S45+S46, and S72 observations, respectively.

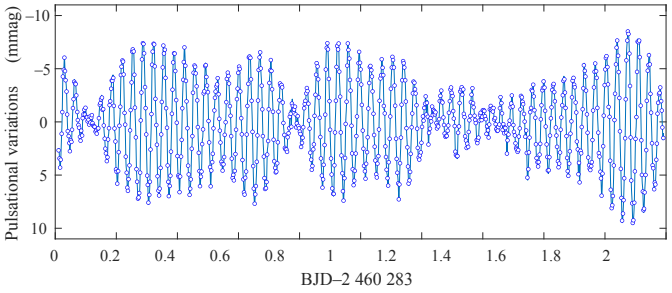


Fig. 19. Disentangled pulsational variability during a two-day interval.

for this phenomenon is the presence of semi-transparent clouds of charged particles frozen in the corotating magnetospheres of the stars, as proposed by Mikulášek et al. (2020) and developed by Krtička et al. (2022) and Mikulášek (2024). We also tested HD 99458 for the presence of these dips.

Fig. 18 shows the residual light curves after subtracting eclipses, long-term trends, spot variability, and pulsations for three data groups, each with a gap of several years. Since these curves do not appear to correlate, they are likely artefacts arising from the removal of the aforementioned variability mechanisms. This again confirms that the studied object is not a magnetic CP star, as other, primarily spectroscopic investigations have conclusively shown.

3.3. Observational manifestation of stellar pulsation

3.3.1. δ Sct pulsations in photometry and radial velocities

The shape of the HD 99458 light curves is determined mainly by strictly periodic brightness variations caused by eclipses, as discussed in Sect. 3.1.1, and by the spots considered in the previous section. As Skarka et al. (2019) first noted, the observed light curve of HD 99458 is also modulated significantly by multiperiodic, δ Sct-type pulsations. In our study, this is convincingly demonstrated by the TESS S72 light-curve detail shown in Fig. 2.

To study the pulsation component of stellar variability, we divided the data into three time-restricted groups: observations from K2, then from TESS sectors 45 and 46, and finally from sector 72, which we investigated separately. We assumed that light changes are periodic with the quadratic ephemeris, approximated by a smooth light curve, while we approximated the pulsations as a sum of sinusoidal changes with different frequencies and amplitudes (Fig. 19). By analysing the frequency spectrum

Table 11. Pulsation frequencies derived from the radial velocity time series.

ID	f ($\pm 0.05\,\mathrm{d}^{-1}$)	A (± 0.03 km s^{-1})	CID
f_{s1}	28.98	0.80	f_{16}
f_{s2}	26.77	0.56	f_{46}
f_{s3}	32.95	0.55	f_{94}
f_{s4}	33.05	0.50	f_{56} or f_{106}
f_{s5}	26.32	0.48	f_{65}
f_{s6}	31.60	0.39	f_{29}
f_{s7}	32.70	0.37	f_{49}
f_{s8}	31.24	0.29	
f_{s9}	23.83	0.27	

Notes. Columns give mode ID, frequency f (in d^{-1}), amplitude A (in km s^{-1}), and possible cross-identification (CID) with frequencies listed in Table B.1.

Table 12. Datasets used in seismic LPV analysis, sorted by average orbital phase φ_{orb}.

ID	BJD (first–last)	φ_{orb} (first–last)	N	Instrument
DS1	2 461 069.197–.426	0.964–0.048	62	MRES
DS2	2 461 102.116–.427	0.056–0.170	84	MRES
DS3	2 461 072.215–.462	0.072–0.163	67	MRES
DS4	2 458 859.381–.462	0.185–0.214	12	MRES
DS5	2 458 549.545–.623	0.357–0.386	20	HERMES
DS6	2 461 070.220–.467	0.340–0.431	67	MRES
DS7	2 458 860.313–.475	0.527–0.586	23	MRES
DS8	2 460 850.475–.576	0.621–0.658	22	PLATOSpec
DS9	2 461 071.214–.469	0.705–0.799	69	MRES

Notes. N denotes the number of spectra in each dataset.

of the variability, we identified several dozen frequencies in each group. In Table B.1, we summarise the reliably identified frequencies and their characteristics.

Multiperiodic pulsations are also visible in the measured radial velocities. After subtracting the orbital variation (Sect. 3.1.2), we performed a standard Fourier analysis of the residuals using the `Period04` programme (Lenz & Breger 2005). By prewhitening the time series obtained with MRES, PLATOSpec, and Whoppshel, we detected the nine pulsation frequencies listed in Table 11. Seven of these frequencies are potentially cross-identified in Table B.1.

3.3.2. Pulsation-induced LPV

First high-S/N spectra of HD 99458 obtained with the MSS and HERMES in 2019 revealed line-profile variability characteristic of pulsating δ Sct stars. Since then, we collected nine time-resolved datasets, including seven nights with MRES and one night each with HERMES and PLATOSpec, as listed in Table 12. The observations sample a range of orbital phases: three datasets are close to primary eclipse, one is near secondary eclipse, and two are nearly symmetric between secondary eclipse and quadratures.

From the beginning of our study, we aimed to test the influence of the close secondary body on stellar pulsations. Recent progress in interpreting tidally perturbed pulsations achieved in Zhang et al. (2024), Jayaraman et al. (2024), and most recently Fuller et al. (2025) has reinforced the relevance of our work. Given the good coverage of orbital phases and the high temporal resolution of the data collected in our study, we can directly assess the spectroscopic manifestation of tidally perturbed pulsations across different configurations.

For LPV analysis, we use a pixel-to-pixel technique based on the two-dimensional Discrete Fourier Transform (2D-DFT). The implementation follows the principles developed in Kennelly et al. (1992), Kennelly (1994), and Telting & Schrijvers (1997). Our variant of the 2D-DFT maps pulsations across the line profile and extracts the amplitude and phase of the selected modes, which are required for spectroscopic mode identification. The analysis is combined with the method developed by Mkrtichian et al. (in prep.) for reconstructing the surface nodal structure of tidally inclined pulsations in oEA stars. Fig. 20 shows the three-panel summary diagram produced by our 2D-DFT code for dataset DS6.

The left panel of Fig. 20 illustrates the average-subtracted line profiles. The vertical axis of the panel shows time in minutes that elapsed from the beginning of the series. The top axis in all panels gives the apparent longitude ϕ, spanning from $-90°$ to $+90°$, with $\phi = 0$ at the centre of the visible hemisphere. The lower axis of the panels shows the velocity scale, which varies across the line profile from $-v \sin i$ to $v \sin i$. The middle panel demonstrates the amplitude of the Fourier transform of the LPV computed in the time domain. The corresponding phase is shown in the right panel.

In LPV data, pulsation modes produce characteristic patterns resembling waves travelling across the line profile. Propagation from negative to positive longitude ϕ corresponds to a prograde mode, whereas propagation in the opposite direction indicates a retrograde mode. In the Fourier domain (middle panels), the pulsation appears as a signal at the frequency $f_{2\mathrm{D}}$. For non-radial modes, the amplitude distribution of the LPV exhibits alternating maxima and minima associated with the nodes and antinodes of the pulsation pattern, the number and spacing of which are related to the azimuthal order m. The spherical degree ℓ can be estimated from the phase variation across the line profile following schemes described in Schrijvers et al. (1997) and Telting & Schrijvers (1997).

The observed LPV pattern of HD 99458 is considerably more complex than the ideal case described above, with traces of multiple modes, including both prograde and retrograde components. Eclipses, changes in orbital configuration, and limited temporal resolution further complicate the interpretation. However, the most striking feature of the LPV in our observations is the presence of standing waves, clearly visible in the middle panel of Fig. 20. Standing waves are a distinctive feature of gravitationally perturbed pulsators (Fuller et al. 2025). The 2D-DFT diagrams for the remaining datasets (Sect. C) show how the pulsation pattern appears at different orbital phases. In each dataset, there is at least one pair of bright antinodes with a phase difference of π between them, as shown in Fig. 21. More regularly, however, the Fourier phase exhibits a staircase-like distribution. By localising the antinodes on the surface of the pulsating primary, we sought to identify the corresponding modes.

To identify the spectroscopic modes, we first measured the apparent frequencies $f_{2\mathrm{D}}$, amplitudes, and apparent longitudes ϕ of the antinodes listed in Table 13. Due to differences in temporal resolution and coverage across the datasets, the accuracy of

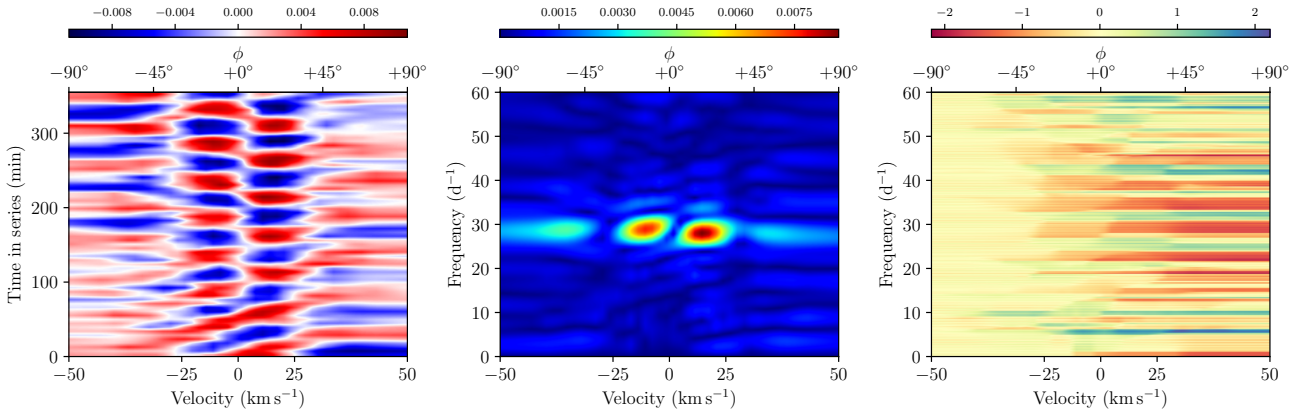


Fig. 20. 2D-DFT summary of LPV analysis of dataset DS6. The corresponding range of $\varphi_{\rm orb}$ is 0.340–0.431. The left panel shows LPV in residual spectra, the middle panel demonstrates the amplitude in the 2D Fourier transform of LPV, and the right panel shows the corresponding phase.

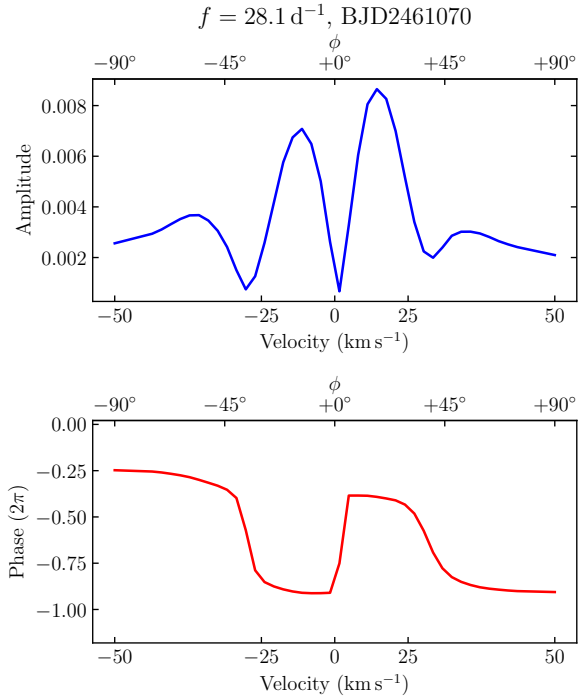


Fig. 21. Amplitude and phase variations of two modes near $f = 28.1\,{\rm d}^{-1}$ observed in dataset DS6.

Table 13. Apparent longitudes, frequencies, and amplitudes of the antinodes measured from the 2D-DFT diagrams.

ϕ (±5°)	$f_{\rm 2D}$ (±1.0 d^{-1})	A (×10^{-3})	ϕ (±5°)	$f_{\rm 2D}$ (±1.0 d^{-1})	A (×10^{-3})
DS1 (−13.0–17.3)			DS5 (128.5–139.0)		
−41	28.1	4.6	−39	26.1	1.9
−34	34.1	1.9	−6	27.9	2.5
−14	33.0	2.5	+11	35.7	1.7
−11	27.1	4.8	+26	26.6	3.9
+18	27.2	3.3	+55	28.5	2.5
+56	28.3	3.3	DS6 (122.4–155.2)		
DS2 (20.2–61.2)			−58	28.9	3.9
−22	28.6	7.5	−14	29.0	7.2
+8	29.5	7.6	+19	28.1	8.2
+13	33.7	3.5	+56	28.0	3.1
+41	27.0	5.5	DS7 (189.7–211.0)		
DS3 (25.9–58.7)			−39	32.3	1.5
−55	27.3	4.4	−2	30.2	2.3
−44	31.3	2.8	+30	28.0	2.2
−15	27.6	6.3	DS8 (223.6–236.9)		
+4	33.4	3.7	−25	30.1	3.9
+24	29.1	3.2	+11	29.1	4.8
+44	30.1	3.3	+35	28.3	4.1
DS4 (66.6–77.0)			DS9 (253.8–287.6)		
−26	29.7	1.2	−17	26.4	5.6
+16	26.9	1.5	−17	31.6	5.2
+59	31.3	0.8	+3	32.7	6.0
			+9	32.2	6.3
			+17	26.9	5.9

Notes. Range of phase angles spanning the time series is given in parentheses for each dataset.

the extracted values varies. The typical frequency uncertainty is of order 1 d^{-1} and depends strongly on the spot's angular position. The position of the antinode also defines the accuracy of the longitude measurements. Antinodes located closer to the stellar limb are more strongly affected by projection effects. The quoted uncertainty ±5° in ϕ therefore reflects only the accuracy with which the antinode's position can be inferred from the diagram, and does not account for the underlying physics.

In the second step, the antinode positions were mapped onto the stellar surface by correcting the apparent longitude ϕ for the orbital phase of the system. This procedure revealed zones where the antinodes preferentially occur (Fig. 22).

Finally, we averaged the positions of the individual antinode groups and compared their distribution with sectoral patterns containing different numbers of sectors. The best agreement was obtained for patterns corresponding to azimuthal orders $|m| = 5 \pm 1$, implying $\ell \geq |m| \geq 4$. The inferred pulsation pattern itself appears stable and synchronised with the orbital motion. However, we cannot exclude that some peaks originated from overlapping low-degree modes, as the frequencies in Table 13 form two distinct clusters below and above $f_{\rm 2D} \approx 30\,{\rm d}^{-1}$. To resolve this ambiguity, detailed mode modelling is required, which is beyond the scope of this paper.

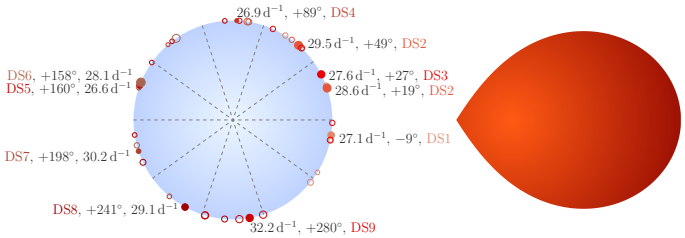


Fig. 22. Pole-on projection showing the distribution of surface antinodes on the pulsating component, derived from 2D-DFT diagrams. Datasets are colour-coded. The filled, labelled circles indicate the highest-amplitude peak in each dataset. Labels contain the dataset ID, frequency, and physical longitude of the antinode. Dashed lines identify nodal positions for the azimuthal order $|m| = 5$. The secondary component is shown for reference.

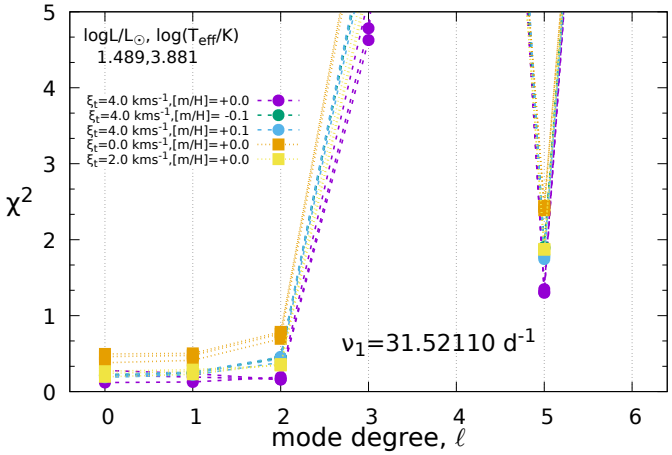


Fig. 23. χ^2 as a function of the mode degree, ℓ, for the dominant frequency $f_1 = 31.52110\,\mathrm{d}^{-1}$.

3.4. Seismic modelling

The detection of δ Sct-type pulsations makes HD 99458 a suitable target for asteroseismic modelling. Determining the star's evolutionary status places an important constraint.

The luminosity of HD 99458 can be estimated from the apparent brightness $V = 8.16(9)$ mag (Høg et al. 2000) and the parallax $\pi = 3.827(41)$ mas (Gaia DR3; Gaia Collaboration et al. 2016, 2021). The 3D reddening maps of Green et al. (2018) give the colour excess $E(B-V) = 0.033(17)$ mag at the star's parallax-based distance of 261.3 ± 2.8 pc. Adopting the total-to-selective extinction ratio for the Johnson V band, $R_V = 3.089$ (Fitzpatrick 2004), we derive an extinction of $A_V = 0.103(52)$ mag. The bolometric correction for the Johnson V band, taken from Flower (1996), is $BC_V = 0.0321(21)$, which yields a luminosity of $\log L/L_\odot = 1.489(31)$. The corresponding position in the Hertzsprung–Russell diagram (Fig. 26) places HD 99458 in the category of evolved stars.

Available Strömgren *bvy* photometry allowed us to perform preliminary mode identification. We applied the method developed by Daszyńska-Daszkiewicz et al. (2003), which provides constraints on the spherical degree ℓ of the pulsation modes. In particular, we constrained the mode degree of the dominant frequency, $f_1 = 31.52110\,\mathrm{d}^{-1}$ from Table B.1. The results are presented in Fig. 23, where the χ^2 values are shown as a function of ℓ. Here, χ^2 quantifies the goodness of fit between observed and calculated amplitudes and phases.

The calculated amplitudes and phases depend slightly on the adopted atmospheric models. In this work, we used the Vienna model atmospheres (Heiter et al. 2002) and adopted the nonlinear limb-darkening law of Claret (2000). We also examined the effects of different metallicities, [m/H], and microturbulent velocities, ξ_t. The effective temperature, adopted from the spectroscopic analysis, and the luminosity were fixed at the centre of the observational error box.

Our results indicate that in the observed pulsation spectrum, modes with $\ell = 0$, 1, and 2 are all plausible. Although the photometric mode identification is not fully conclusive and cannot replace modelling, it does not rule out the $\ell = 2$ hypothesis for the dominant mode, which is independently suggested by the seismic models discussed in the next section.

3.4.1. Multiplets

In the frequency spectrum of HD 99458, we identified two regular structures that can be interpreted as rotationally split modes of the same spherical degree and radial order, but with different azimuthal orders. The frequencies belonging to multiplet A and multiplet B are indicated in Fig. 24. The frequency separations between consecutive components are also shown on the right-hand y-axis. Both structures exhibit comparable frequency spacings and span a similar frequency range. The individual components of the multiplets are listed in Table 14. For multiplet analysis, we adopted the f_{best} frequencies listed in Table B.1. The K2 spectrum shown in Fig. 24 is used only to illustrate the frequency pattern.

Such regular patterns enable mode identification even when observations are limited to a single photometric band. Multiplet A consists of five components and can be interpreted as the complete set of rotationally split quadrupole modes ($\ell = 2$). Multiplet B comprises six frequencies, generally with lower amplitudes, and may correspond to octupole modes ($\ell = 3$). However, this multiplet is less regular than multiplet A, and one component appears to be missing, as $\ell = 3$ modes are expected to split into seven components.

Table 14. Frequencies, amplitudes, and frequency separations of the multiplets detected in HD 99458.

ID	f (d^{-1})	σ_f (d^{-1})	A (mmag)	Δf (d^{-1})	$\sigma_{\Delta f}$ (d^{-1})
		multiplet A			
f_{20}	26.65500	0.00030	0.640	0.3489	0.00042
f_{21}	27.00390	0.00030	0.580	0.3828	0.00036
f_4	27.38670	0.00020	1.550	0.3549	0.00022
f_2	27.74160	0.00010	1.800	0.3710	0.00022
f_5	28.11260	0.00020	1.460	—	—
		multiplet B			
f_{42}	27.29660	0.00090	0.210	0.3840	0.00092
f_7	27.68060	0.00020	1.180	0.3749	0.00028
f_9	28.05550	0.00020	1.030	0.3070	0.00028
f_{12}	28.36250	0.00020	0.920	0.3311	0.00073
f_{32}	28.69360	0.00070	0.300	0.3579	0.00086
f_{30}	29.05150	0.00050	0.350	—	—

Notes. The uncertainties of the frequency separations were calculated as $\sigma_{\Delta f} = (\sigma_{f_i}^2 + \sigma_{f_{i+1}}^2)^{1/2}$.

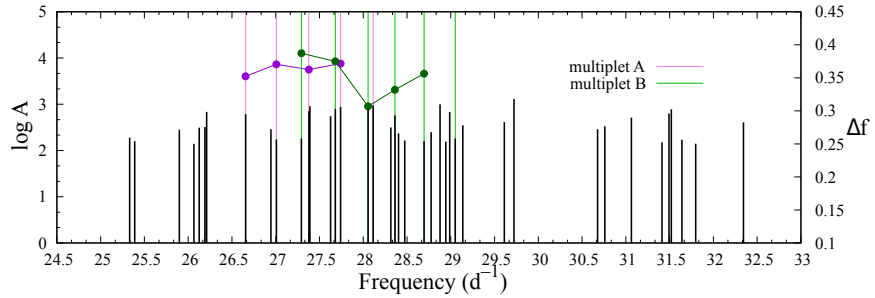


Fig. 24. Frequency spectrum of HD 99458. Left-hand y-axis shows the amplitudes of the detected modes. Frequencies belonging to multiplet A are indicated by violet lines, while those associated with multiplet B are marked in green. Right-hand y-axis shows the frequency separations between consecutive multiplet components, indicated by circles. Only frequencies derived from the K2 observations are shown.

3.4.2. Evolutionary models

Evolutionary tracks were computed using the Modules for Experiments in Stellar Astrophysics (MESA) code (Paxton et al. 2011, 2013, 2015, 2018, 2019), version 12115. Unless stated otherwise, we adopted the OPAL opacity tables (Iglesias & Rogers 1996), supplemented at low temperatures with data from Ferguson et al. (2005). The solar chemical composition was taken from Asplund et al. (2009).

The equation of state (EOS) implemented in MESA is a combination of several formulations, including OPAL (Rogers & Nayfonov 2002), SCVH (Saumon et al. 1995), PTEH (Pols et al. 1995), HELM (Timmes & Swesty 2000), and PC (Potekhin & Chabrier 2010). Nuclear reaction rates were adopted from the JINA REACLIB database (Cyburt et al. 2010), complemented by tabulated weak reaction rates from Fuller et al. (1985); Oda et al. (1994); Langanke & Martínez-Pinedo (2000). Screening effects were included following the prescriptions of Salpeter (1954), Dewitt et al. (1973), Alastuey & Jancovici (1978), and Itoh et al. (1979), while thermal neutrino loss rates were taken from Itoh et al. (1996). The evolutionary calculations include atomic diffusion as well as exponentially decaying convective core overshooting (Herwig 2000).

In a subset of models, we also considered rotationally induced mixing processes and angular momentum transport, including the Solberg–Høiland instability, secular shear instability, Eddington–Sweet circulation, Goldreich–Schubert–Fricke instability, and dynamical shear instability. A detailed description of these mechanisms can be found in Heger et al. (2000). In these computations, we adopted the scaling factor $f_c = 1/30$, which governs the efficiency of rotational mixing in the diffusion coefficient (Pinsonneault et al. 1989; Chaboyer & Zahn 1992; Heger et al. 2000), and $f_\mu = 0.05$, which describes the sensitivity of rotational mixing to the mean molecular weight gradient, ∇_μ (Heger et al. 2000).

3.4.3. Pulsational models

Adiabatic and non-adiabatic pulsation models were computed using our in-house code, which solves the linearised stellar pulsation equations (Walczak & Kopacz 2024). The effects of rotation were included using a perturbative approach, by solving first-order perturbed eigenfunctions (e.g. Ledoux 1951; Dziembowski & Goode 1992; Soufi et al. 1998; Suárez et al. 2006). Radial differential rotation was also taken into account. The rotational velocity profiles were obtained from MESA, which treats angular momentum transport in a diffusion approximation (Endal & Sofia 1978; Pinsonneault et al. 1989; Heger et al. 2000). We considered modes with degrees $\ell = 0$, 1, 2, and 3, and all corresponding azimuthal orders, $m \in [-\ell, \ell]$.

We aimed to reproduce the observed frequencies of HD 99458 using models located within the observational error box in the Hertzsprung–Russell diagram. We explored a broad parameter space, covering metallicities in the range $Z = 0.008$–0.02, stellar masses from $M = 1.8\,M_\odot$ to $2.2\,M_\odot$, and convective core overshooting parameters from $f_{\rm ov} = 0$ to 0.04. We also tested two values of the initial hydrogen abundance, $X = 0.70$ and $X = 0.725$, as well as two values of the mixing-length parameter, $\alpha_{\rm mlt} = 1.8$ and 1.0.

In our modelling, we assumed that multiplet A is associated with quadrupole modes ($\ell = 2$). We began by fitting the axisymmetric mode $f_4 = 27.38670\,{\rm d}^{-1}$. This frequency can be reproduced by modes of different radial orders, n, and therefore the position of the star in the Hertzsprung–Russell diagram was used to constrain the value of n. Initially, several solutions were possible, depending on the adopted model parameters. However, further analysis showed that only one solution was consistent with all constraints, corresponding to $n = 7$. Fitting the axisymmetric mode thus imposes a strong constraint on effective temperature (and hence the age) for a given set of parameters, including chemical composition (Z, X), stellar mass, rotational velocity, mixing-length parameter, and overshooting parameter.

Next, we attempted to reproduce the non-axisymmetric components of multiplet A. The key parameter controlling frequency splitting is the rotational velocity, $\upsilon_{\rm rot}$. By adjusting this parameter and adopting appropriate $T_{\rm eff}$ values, we were able to reproduce the observed frequencies of all components of multiplet A with good accuracy. Fitting both the axisymmetric mode and its rotationally split components effectively constrains two parameters, $T_{\rm eff}$ and $\upsilon_{\rm rot}$.

We then explored models computed with different values of Z, X, M, $\alpha_{\rm mlt}$, and $f_{\rm ov}$. By comparing observed and theoretical frequency spectra, we found that the high-amplitude frequency $f_3 = 29.72200\,{\rm d}^{-1}$ can be uniquely identified as an ($\ell = 2$, $m = -1$, p_8) mode. In the next step, we determined the stellar mass required to reproduce this frequency. Although f_3 could also be matched by a ($\ell = 2$, $m = -1$, p_9) mode if f_4 were assumed to have $n = 8$, such models lie well outside the observational error box in the Hertzsprung–Russell diagram and were therefore rejected.

We then examined models that simultaneously reproduce the components of the quadrupole multiplet and frequency f_3, exploring a range of metallicities, initial hydrogen abundances, mixing-length parameters, and overshooting efficiencies. We found that, for a particular metallicity, the dominant frequency $f_1 = 31.52110\,{\rm d}^{-1}$ can be matched by an ($\ell = 2$, $m = -1$, p_9) mode.

The final frequency we were able to reproduce accurately is $f_{23} = 26.12570\,{\rm d}^{-1}$. Achieving this required adjusting the overshooting parameter. For an appropriate value of $f_{\rm ov}$, this frequency can be identified as a dipole mode ($\ell = 1$, $m = 0$, p_8).

We note that the initial hydrogen abundance and mixing-length parameter have only a minor impact on the remaining, unfitted frequencies, and therefore cannot be reliably constrained using this approach. This issue is discussed further below.

A representative seismic model that reproduces the quadrupole multiplet as well as the f_3, f_1, and f_{23} frequencies is presented in Table 15 (Model 1). In this model, we adopt $X = 0.7$, $\alpha_{\rm mlt} = 1.8$, and OPAL opacities, while the remaining parameters are determined through frequency fitting. Rotationally induced mixing processes are not included in these calculations.

The resulting model requires a relatively large amount of convective core overshooting, $f_{\rm ov} = 0.03$. It is also slightly hotter than the blue edge of the observational error box in the Hertzsprung–Russell diagram, and its metallicity is subsolar.

The main discrepancy in this model concerns the rotational velocity. We derive a surface rotation of approximately 29 km s^{-1}, which is significantly lower than the observed projected rotational velocity, $\upsilon \sin i = 49.9 \pm 2.0$ km s^{-1}. This inconsistency can be alleviated by including rotationally induced mixing and angular-momentum transport. MESA provides several such mechanisms, as described in Sect. 3.4.2.

Rotationally induced mixing processes modify both the chemical composition profile and angular momentum transport within the star. In models that include rotational mixing, angular momentum is redistributed from the interior towards the surface, leading to significantly faster rotation in the outer layers. The resulting surface rotational velocity reaches approximately 50 km s^{-1}, making these models potentially consistent with the spectroscopic rotational constraint. A quantitative comparison with the observed $\upsilon \sin i$, including the inclination inferred from the orbital solution, is presented below. This result can therefore be regarded as indirect evidence for angular momentum transport mechanisms. The parameters of the seismic models computed with rotational mixing are listed in Table 15.

We examined two values of initial hydrogen abundance, corresponding to $X = 0.70$ for Model 2 and $X = 0.725$ for Model 3. Similarly, we tested two values of mixing-length parameter, with $\alpha_{\rm mlt} = 1.8$ for Model 2 and $\alpha_{\rm mlt} = 1.0$ for Model 4.

Internal rotational profiles of models computed without and with rotational mixing are shown in Fig. 25. The left-hand axis represents the linear rotational velocity, $\upsilon_{\rm rot}$ (in km s^{-1}), while the right-hand axis gives the corresponding angular velocity, Ω. In models without rotational mixing, the rotational velocity in the outer layers decreases to values of order 30 km s^{-1}. By contrast, models including rotational mixing exhibit a nearly monotonic increase in $\upsilon_{\rm rot}$ towards the surface, reaching approximately 50 km s^{-1} in the outermost layers.

It is noteworthy that Models 1 and 2 differ substantially, although the principal change in the adopted physical treatment is the inclusion of rotationally induced mixing and angular-momentum transport. Re-optimising our seismic solution then leads to significant differences in the inferred stellar parameters, including metallicity, mass, overshooting efficiency, and other model properties.

The origin of this behaviour is related to the nature of high-order p modes considered in our study, which propagate primarily in the outer stellar envelope. In the bottom panel of Fig. 25, we present mode inertia for the quadrupole axisymmetric mode ($\ell = 2$, $m = 0$, p_7), showing that most of the pulsation energy is concentrated in the outer layers above the region where $\log T \simeq 5.0$. As a result, rotational splitting of the multiplets is determined mainly by the rotation profile in these outer regions. Since these layers are most strongly affected by rotational mixing, including such processes has a substantial impact on the seismic modelling results.

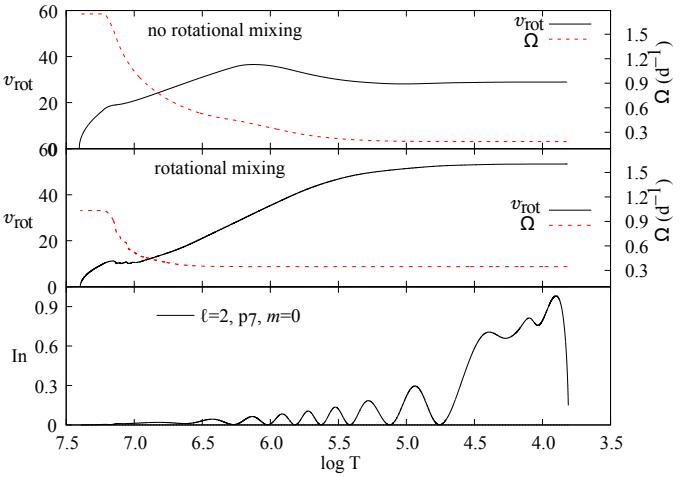


Fig. 25. Upper panel: internal rotational profile of seismic Model 1 listed in Table 15, given in terms of the linear rotational velocity (left-hand axis, in km s^{-1}) and the angular velocity (right-hand axis). Middle panel: as in the upper panel, but for Model 2, which includes rotational mixing. Bottom panel: mode inertia profile (in arbitrary units) for the ($\ell = 2$, $m = 0$, p_7) mode computed for Model 2.

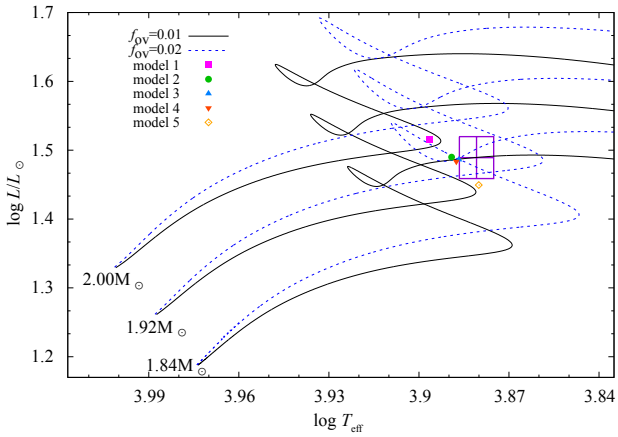


Fig. 26. Hertzsprung–Russell diagram showing the position of HD 99458. Evolutionary tracks were computed for $f_{\rm ov} = 0.02$, $\upsilon_{\rm rot,0} = 80$ km s^{-1}, $Z = 0.01$, and $X = 0.7$. Locations of the seismic models discussed in the text are also indicated.

Theoretical modes predicted within the observed frequency range of our seismic models are found to be stable. The instability parameter, η (Stellingwerf 1978), is typically of order -0.4, indicating difficulties in reproducing the excitation of the observed pulsation modes. However, these instability results should be interpreted with caution. In the present calculations, we adopted a frozen convective flux approximation, which is not ideally suited for δ Sct pulsators. A more realistic treatment would require a time-dependent, non-local convection formalism (e.g. Xiong et al. 2016; Antoci et al. 2019), although such modelling is beyond the scope of this work.

All models listed in Table 15 reproduce the observed frequency spectrum of HD 99458 reasonably well. Comparison between observed and theoretical spectra for Model 2 is presented in Fig. 27, where multiplets A and B are highlighted. The theoretical spectrum includes modes with degrees $\ell = 0$–3 and all

Table 15. Seismic models of HD 99458.

Model	opacity	Z	X	f_{ov}	α_{mlt}	$\upsilon_{rot,0}$ ($km\,s^{-1}$)	υ_{rot} ($km\,s^{-1}$)	M ($M_\odot$)	$\log T_{eff}$	$\log \frac{L}{L_\odot}$	R ($R_\odot$)	$\log g$	Age (Myr)	X_c
no rotational mixing														
1	OPAL	0.0089	0.7	0.030	1.8	126.1	28.7	1.9016	3.8965	1.5153	3.0754	3.7400	963.447	0.173
rotational mixing														
2	OPAL	0.0110	0.7	0.027	1.8	78.0	52.9	1.9467	3.8890	1.4895	3.0906	3.74599	934.616	0.178
3	OPAL	0.0104	0.725	0.028	1.8	77.6	53.3	1.9861	3.8867	1.4862	3.1118	3.7487	999.334	0.194
4	OPAL	0.0109	0.7	0.022	1.0	77.3	52.9	1.9451	3.8882	1.4860	3.0898	3.7458	939.428	0.173
5	OPLIB	0.0117	0.7	0.030	1.8	76.9	52.7	1.9212	3.8801	1.4494	3.0748	3.7447	993.381	0.191

Notes. Columns list the model identifier (Model), adopted opacity tables (Opacity), metallicity (Z), initial hydrogen abundance (X), convective core overshooting parameter (f_{ov}), mixing-length parameter (α_{mlt}), initial surface rotational velocity ($\upsilon_{surf,0}$), current surface rotational velocity (υ_{surf}), stellar mass (M), effective temperature ($\log T_{eff}$), luminosity ($\log L/L_\odot$), radius (R), surface gravity ($\log g$), age measured from the zero-age main sequence (Age), and central hydrogen abundance (X_c).

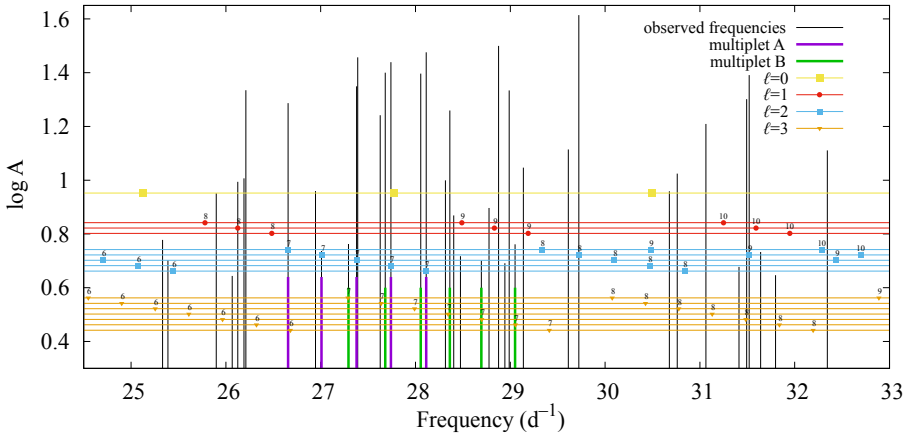


Fig. 27. Comparison between the observed and theoretical frequency spectra for Model 2. Components of multiplets A and B are indicated by violet and green lines, respectively. For clarity, the amplitudes of the frequencies detected in the K2 photometry have been scaled by a factor of 0.5. The vertical scale for the theoretical modes is arbitrary.

corresponding azimuthal orders; the vertical positions of the theoretical frequencies are arbitrary and serve only for visual clarity.

Multiplet A is reproduced particularly well by our model. Good agreement is also obtained for several individual frequencies, including the high-amplitude mode f_1, as well as f_3 and f_{23}. Additional satisfactory matches are found for $f_{41} = 28.40390\,d^{-1}$, identified as an ($\ell = 1$, $m = -1$) mode, $f_6 = 31.49280\,d^{-1}$, corresponding to ($\ell = 3$, $m = 1$), and $f_{18} = 30.75890\,d^{-1}$, identified as an ($\ell = 3$, $m = -1$) mode.

Interestingly, multiplet B is also reproduced reasonably well, particularly for the $m = -3$, 0, 1, and 2 components. The agreement is somewhat poorer for the $m = -2$ and $m = -1$ components. Many additional observed frequencies also have theoretical counterparts, although the agreement is not always exact. For example, the frequency $f_8 = 28.87760\,d^{-1}$ appears to correspond to an ($\ell = 1$, $m = 0$, p_9) dipole axisymmetric mode, but the predicted theoretical frequency is slightly lower than the observed value.

Propagating the frequency uncertainties to the individual splittings according to

$$\sigma_{\Delta f} = \left(\sigma_{f_i}^2 + \sigma_{f_{i+1}}^2\right)^{1/2},$$

we obtain consecutive splittings 0.3489 ± 0.00042, 0.3828 ± 0.00036, 0.3549 ± 0.00022, and $0.3710 \pm 0.00022\,d^{-1}$ for multiplet A, while for multiplet B they are 0.3840 ± 0.00092, 0.3749 ± 0.00028, 0.3070 ± 0.00028, 0.3311 ± 0.00073, and $0.3579 \pm 0.00086\,d^{-1}$. Thus, if only the formal frequency uncertainties are considered, the departure from uniform splitting is highly significant. We note, however, that these uncertainties describe the precision of the frequencies determined from the individual datasets and do not account for the observed epoch-to-epoch frequency variations. Indeed, frequencies measured independently from the K2 data and the two TESS sectors show shifts that are typically one or two orders of magnitude larger than their formal uncertainties. For example, the four splittings of multiplet A are 0.3489, 0.3791, 0.3586, and $0.3720\,d^{-1}$ in Sector 45; 0.3475, 0.3874, 0.3544, and $0.3714\,d^{-1}$ in Sector 72; and 0.3526, 0.3693, 0.3634, and $0.3714\,d^{-1}$ in K2 data. Therefore, although the non-equidistant character of the multiplets appears to be robust, the very high formal significance inferred from the statistical frequency uncertainties alone should not be interpreted literally.

Perfectly equidistant multiplets are expected only in the first-order perturbative approximation for sufficiently slow rotation. At the precision reached by observations of HD 99458, departures from this approximation may become important. Included radial differential rotation changes the magnitude of first-order splitting through a mode-dependent rotational kernel, but does not by itself produce non-equidistant components within a given multiplet. Additional deviations from a simple first-order Ledoux splitting may arise from second- and higher-order rotational effects, such as centrifugal distortion and higher-order Coriolis terms, which are not included in the present calculations. Near-degeneracy between modes of similar frequencies may further perturb the individual multiplet components. In addition, latitudinal differential rotation and perturbations related

to the close binary configuration may contribute to the observed non-uniformity of the splittings.

Seismic rotation inferred from the multiplet structure is nevertheless consistent with the independent orbital and spectroscopic constraints. Using the spectroscopic constraint $M_1 \sin^3 i = 1.39 \pm 0.10\,M_\odot$ together with the masses of our seismic models, $M \simeq 1.92$–$1.99\,M_\odot$, we obtain inclination angles of approximately 60°–67°, with central values close to 63°. For the models including rotational mixing, the present-day surface rotational velocities are $\upsilon_{\rm surf} \simeq 52.7$–$53.3$ km s^{-1}, corresponding to $\upsilon \sin i \simeq 46.1$–$48.4$ km s^{-1}. These values are broadly consistent with the spectroscopic estimate of $\upsilon \sin i = 49.9 \pm 2.0$ km s^{-1}. The corresponding surface rotation periods are approximately $2\overset{\rm d}{.}95$, that is slightly longer than the orbital period, $P_{\rm orb} = 2\overset{\rm d}{.}722172$.

We stress, however, that our seismic models include differential rotation, so the rotational splittings probe a kernel-weighted internal rotation rate rather than simply the surface angular velocity. Moreover, the exact surface rotation rate depends on the efficiency of angular momentum transport and has not been specifically calibrated to enforce synchronisation with the orbit. Thus, although the present models are not exactly synchronised at the surface, they reproduce multiplet A very well, provide a reasonable description of multiplet B, and simultaneously predict a projected surface rotational velocity consistent with the observed $\upsilon \sin i$. We therefore consider the seismic interpretation and the spectroscopic rotational constraint to be mutually consistent.

We find a strong dependence of the overshooting parameter on the adopted mixing-length parameter. In Model 4, computed with the lower value $\alpha_{\rm mlt} = 1.0$, the derived overshooting parameter $f_{\rm ov}$ is correspondingly smaller. The remaining stellar parameters, however, differ only marginally.

We also investigated the effect of opacity tables by computing models using OPLIB data (Colgan et al. 2016, 2015). The best-fitting seismic model obtained with OPLIB opacities is presented in Table 15 (Model 5). Significant differences between models computed with OPAL and OPLIB opacities indicate a strong sensitivity of seismic solutions to the opacity profile. High-order p modes primarily probe the outer stellar layers, where opacity profiles from different sources show the largest discrepancies. Consequently, δ Sct pulsators with well-identified multiplets may provide a valuable diagnostic for testing stellar opacity calculations. A comprehensive analysis, however, would require a larger sample of well-constrained multiplets.

The OPLIB-based model occupies a different location in the Hertzsprung–Russell diagram compared to OPAL models, being cooler and less luminous. Nevertheless, it remains close to the observational error box.

Our seismic analysis of HD 99458 suggests moderate-to-efficient convective core overshooting, with $f_{\rm ov}$ in the range of approximately 0.02–0.03. The exact value depends primarily on the mixing-length parameter $\alpha_{\rm mlt}$, and to a lesser extent on opacity tables. The models also indicate that the stellar metallicity is likely subsolar, with $Z \sim 0.01$. By contrast, the hydrogen abundance remains only weakly constrained. Models with higher X provide a slightly better match to the observational error box in the Hertzsprung–Russell diagram (see Fig. 26).

In summary, our seismic modelling of HD 99458 demonstrates that the observed frequency spectrum, including the identified multiplets, can be reproduced consistently within a narrow range of stellar parameters. The models favour subsolar metallicity and moderate-to-efficient convective core overshooting. Comparison between OPAL- and OPLIB-based models highlights the strong sensitivity of high-order p modes to the structure of the outer stellar layers, emphasising the diagnostic potential of δ Sct pulsators for constraining opacity calculations. Although the hydrogen abundance remains weakly constrained, the agreement between the seismic models and observations supports the overall consistency of the seismic solutions. In addition, models including angular-momentum transport yield projected surface rotational velocities consistent with the spectroscopic $\upsilon \sin i$ constraint and reproduce the overall rotational splitting pattern of the identified multiplets.

4. Discussion

Observational evidence collected in our study consistently supports the view that HD 99458 is a typical Algol-type binary system with mass transfer from the secondary component filling its Roche lobe (donor) to a pulsating δ Sct star (gainer), specifically a member of the oEA group of variables (Mkrtichian et al. 2022). This is precisely the interpretation that Skarka et al. (2019) briefly mentioned in their original publication and later rejected in favour of the CP2 star hypothesis.

The evidence collected in our study suggests that variable mass transfer and the accretion disc are responsible for fluctuations in out-of-eclipse photometric flux. Cold spots used in our modelling with `ELISa` are unable to produce a substantial effect on the flux.

We consider remarkably different H_α patterns shown in Fig. 13 and observed in spectra separated by several years to be an observational manifestation of long-periodic activity. Presumably, the main driver of this slow variation is the donor's weak magnetic field. While this field remains undetected, its fluctuating activity provides a plausible explanation for the detection of an X-ray source at the position of HD 99458 in observations from eROSITA (Predehl et al. 2021; Merloni et al. 2024; Ramos-Ceja et al. 2026). The source 3eRASS J112636.1+010319 is located within 1.8″ of HD 99458. The X-ray flux $F_{\rm X}$ of this source is 4.10×10^{-13} erg s^{-1} cm^{-2}. This yields an X-ray luminosity $L_{\rm X} = 3.35 \times 10^{30}$ erg s^{-1}, which is comparable to the X-ray luminosity of Algol (Nakayama et al. 2025).

We attribute the periodic reappearance of the He I 5875 Å line in spectra obtained around the orbital phases $\varphi_{\rm orb} = 0.89$ and $\varphi_{\rm orb} = 0.16$ to the presence of hot regions in the circumstellar environment. This feature naturally explains the excitation of the corresponding transition, which would be impossible in a star with the primary's effective temperature of 7600 K. Given the system geometry, the hot regions are most likely located where the gas stream hits the atmosphere of the pulsating star, clearly visible at orbital phases before the primary minimum, and in another zone on the back side of the gas stream interacting with gas flows circulating around the primary star. A similar periodic excitation of He I line around the phases of primary minima was reported in the semi-detached Algol-type system R CMa by Lehmann et al. (2018).

Strong variable absorption in the H_α line, visible in the PLATOSpec data, and near-IR lines observed with MRES at BJD 2 461 071 are part of the same mass-transfer process. The corresponding orbital phases are nearly symmetric around $\varphi_{\rm orb} = 0.75$, when the line connecting the stars is perpendicular to the line of sight. This geometry suggests that our spectra may have sampled the gas stream flowing from the donor to the gainer at different viewing angles.

We have, for the first time, performed a detailed asteroseismic analysis of HD 99458. We show that the rich pulsation spec-

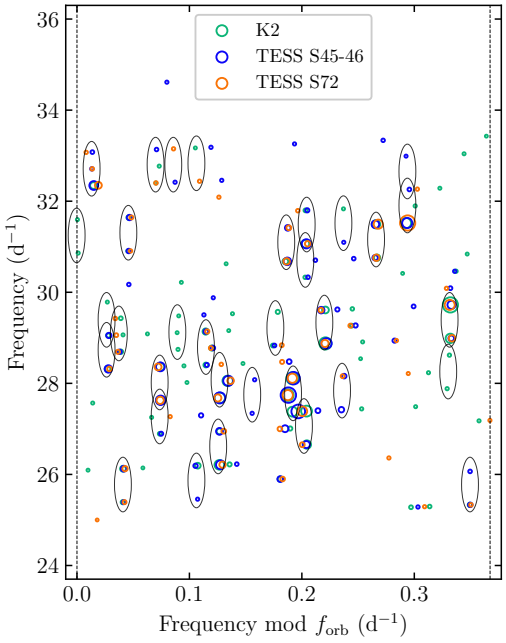


Fig. 28. Échelle diagram showing pulsation peaks detected in Kepler K2 and TESS photometry (Table B.1) as a function of frequency modulo $f_{\rm orb} = 0.36738\,{\rm d}^{-1}$. Frequencies separated by $2f_{\rm orb}$ are indicated in pairs. Symbol size is proportional to the amplitude.

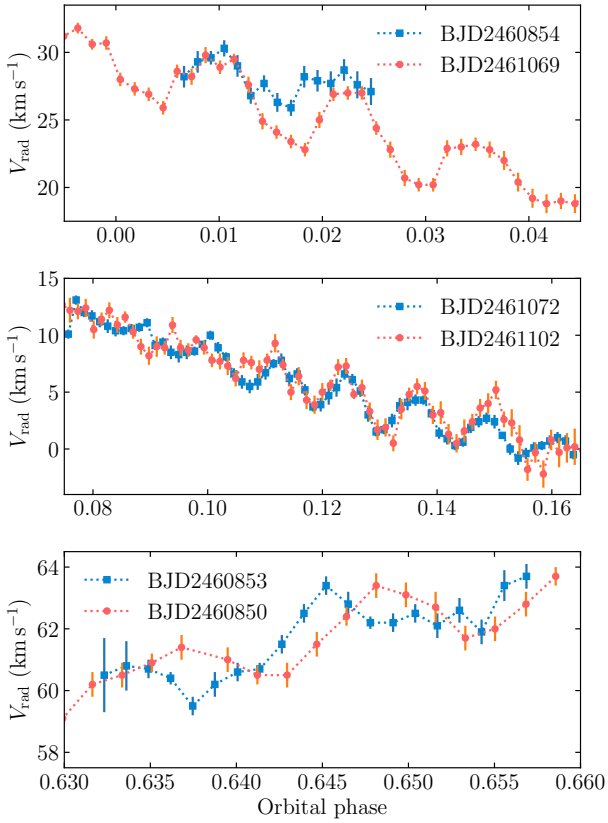


Fig. 29. Radial velocity variations of the pulsating primary at different epochs.

trum extracted from the photometry can be partly explained by intrinsic pulsations of the primary. Comparison between observational and theoretical frequencies shown in Fig. 27 confirms the identification of pulsation modes with degree ℓ up to 3. In addition, the star exhibits pulsation modes tidally perturbed by the secondary. The photometric échelle diagram constructed with the orbital frequency $f_{\rm orb} = 0.36738\,{\rm d}^{-1}$ contains more than 30 pairs of frequencies separated by $2f_{\rm orb}$ (Fig. 28). This effect is well-known and has a natural explanation in the theory of triaxial pulsation in gravitationally distorted stars (Fuller et al. 2025).

Extensive use of time-resolved spectroscopy extends the potential identification of gravitationally perturbed pulsations to higher spherical-harmonic orders inaccessible to photometry. By mapping the antinodes produced by non-radial pulsation and visible in our 2D-DFT analysis, we infer that azimuthal orders as high as $|m| = 5$, possibly ±1, are required to explain the recurrence of the antinodes at the same longitudes in different observing epochs. Furthermore, the character of the variability in radial velocities, shown, for example, in Fig. 29, indicates synchronisation of stellar pulsations with the orbital motion. The agreement between the radial-velocity pulsations observed in different epochs and phased with the photometrically derived $P_{\rm orb}$ independently supports the high consistency of our analysis, including the detection of $\dot{P} = 5.045\,{\rm s\,yr}^{-1}$. Thus, we hypothesise that the discrepancy between the two orbital period values obtained in Sects. 3.1.1 and 3.1.2 most likely originates from the multiplicity of HD 99458, despite the fact that we detect no significant variation in the systemic velocity and did not detect a tertiary in speckle-interferometric observations.

In our analysis, HD 99458 shows none of the Fe, Si, and Ti anomalies reported by Skarka et al. (2019). In contrast to abundances enhanced by 1 dex, we find most elements in HD 99458 to be mildly depleted. Such underabundant Population I A-type stars are commonly classified as λ Bootis stars (Paunzen 2004; Murphy & Paunzen 2017). The abundance profile of these objects is characterised by depletion of Fe-peak elements of up to 2 dex, but near-solar abundances of C, N, O, and S (e.g. Heiter 2002). In a large sample studied by Paunzen et al. (2002), stars showing λ Boo properties occupied the whole width of the main sequence, peaking at an age of ≈ 1 Gyr. An asteroseismically derived age of ~ 0.9 Gyr and subsolar metallicity make HD 99458 a good λ Boo candidate. The λ Boo status of HD 99458 requires additional confirmation primarily due to depleted carbon and slightly deficient sulphur. Even so, the lack of strongly overabundant species typical of CP2 stars, together with the absence of a strong magnetic field, allows us to conclude that the primary component of HD 99458 is genuinely not Ap.

In summary, our study has established a new classification for HD 99458, prompting a re-evaluation of the system as a whole. Beyond this specific result, our findings highlight how data quality and a comprehensive analytical approach influence the physical interpretation of observational data, underscoring the value of time-resolved spectroscopy.

Acknowledgements. The authors are very grateful to the referee for carefully reading our paper and for the thoughtful comments that helped us improve it. The authors express their gratitude to V. Kozlov (International Centre for Astronomical, Medical & Ecological Research, Ukraine) and G. Kapanadze (Georgian National Astrophysical Observatory, Georgia) for their assistance with data acquisition. This work is supported by the Fundamental Fund of Thailand Science Research and Innovation (TSRI) through the National Astronomical Research Institute of Thailand (Public Organization) (FFB690078/0269). This work has been supported by the DAAD (project No. 57442043) and the Erasmus+ programme of the European Union under grant number 2020-1-CZ01-KA203-078200. O.K. acknowledges support from the Swedish Research Council (grant agreement no. 2023-0366) and the Swedish National Space Agency. P.W. acknowledges financial support from the Polish National Sci-

ence Centre (NCN) under grant No. 2023/50/A/ST9/00144. The computations were performed using resources provided by the Wrocław Centre for Networking and Supercomputing (http://wcss.pl) under grant No. 265. M.G. acknowledges support from the EU NextGenerationEU through the Recovery and Resilience Plan for Slovakia under project No. 09I03-03-V04-00262. M.S. acknowledges the support by Inter-transfer grant no LTT-20015. A.V.M. acknowledges partial financial support from the Russian Science Foundation (grant No. 25-12-00003) for the MSS data reduction. J.Ž. acknowledges the support of the PRODEX agreement No. 400012791. This work is based on observations obtained at the Canada-France-Hawaii Telescope (CFHT), which is operated by the National Research Council of Canada, the Institut National des Sciences de l'Univers (INSU) of the Centre National de la Recherche Scientifique (CNRS) of France, and the University of Hawaii. This study includes observations made with MRES across multiple programmes, including the most recent ID TNTC13_011, at the Thai National Observatory, operated by the National Astronomical Research Institute of Thailand (Public Organisation). This work has made use of data from the European Space Agency (ESA) mission Gaia (https://www.cosmos.esa.int/gaia), processed by the Gaia Data Processing and Analysis Consortium (DPAC, https://www.cosmos.esa.int/web/gaia/dpac/consortium). Funding for the DPAC has been provided by national institutions, in particular the institutions participating in the Gaia Multilateral Agreement.

Data availability

Reduced ESPaDOnS spectra are available at the CFHT archive maintained by the CADC at https://www.cadc-ccda.hia-iha.nrc-cnrc.gc.ca/en/, where they can be found via standard stellar designations. The remaining spectra, as well as any additional materials used in the current research, can be obtained from the authors upon request.

References

Alastuey, A. & Jancovici, B. 1978, ApJ, 226, 1034
Anfinogentov, S. A., Nakariakov, V. M., Pascoe, D. J., & Goddard, C. R. 2021, ApJS, 252, 11
Antoci, V., Cunha, M. S., Bowman, D. M., et al. 2019, MNRAS, 490, 4040
Asplund, M., Amarsi, A. M., & Grevesse, N. 2021, A&A, 653, A141
Asplund, M., Grevesse, N., Sauval, A. J., & Scott, P. 2009, ARAA, 47, 481
Aurière, M., Wade, G. A., Silvester, J., et al. 2007, A&A, 475, 1053
Barros, S. C. C., Demangeon, O., & Deleuil, M. 2016, A&A, 594, A100
Blazère, A., Petit, P., Neiner, C., et al. 2020, MNRAS, 492, 5794
Bonsack, W. K. 1981, PASP, 93, 756
Borucki, W. J., Koch, D., Basri, G., et al. 2010, Science, 327, 977
Bowman, D. M., Kurtz, D. W., Breger, M., Murphy, S. J., & Holdsworth, D. L. 2016, MNRAS, 460, 1970
Buysschaert, B., Neiner, C., & Aerts, C. 2017, in IAU Symposium, Vol. 329, The Lives and Death-Throes of Massive Stars, ed. J. J. Eldridge, J. C. Bray, L. A. S. McClelland, & L. Xiao, 146–150
Carrier, F., North, P., Udry, S., & Babel, J. 2002, A&A, 394, 151
Chaboyer, B. & Zahn, J. P. 1992, A&A, 253, 173
Chaplin, W. J., Elsworth, Y., Davies, G. R., et al. 2014, MNRAS, 445, 946
Chargeishvili, B. B. 2024, Communications of the Byurakan Astrophysical Observatory, 71, 340
Chountonov, G. A. 2004, in Magnetic Stars, 286–291
Claret, A. 2000, A&A, 363, 1081
Colgan, J., Kilcrease, D. P., Magee, N. H., et al. 2015, High Energy Density Physics, 14, 33
Colgan, J., Kilcrease, D. P., Magee, N. H., et al. 2016, ApJ, 817, 116
Cowley, C. R. & Hubrig, S. 2008, MNRAS, 384, 1588
Cyburt, R. H., Amthor, A. M., Ferguson, R., et al. 2010, ApJS, 189, 240
Daszyńska-Daszkiewicz, J., Dziembowski, W. A., & Pamyatnykh, A. A. 2003, A&A, 407, 999
Dewitt, H. E., Graboske, H. C., & Cooper, M. S. 1973, ApJ, 181, 439
Donati, J. F., Semel, M., Carter, B. D., Rees, D. E., & Collier Cameron, A. 1997, MNRAS, 291, 658
Dziembowski, W. A. & Goode, P. R. 1992, ApJ, 394, 670
Endal, A. S. & Sofia, S. 1978, ApJ, 220, 279
Eyer, L., Audard, M., Holl, B., et al. 2023, A&A, 674, A13
Ferguson, J. W., Alexander, D. R., Allard, F., et al. 2005, ApJ, 623, 585
Fitzpatrick, E. L. 2004, in Astronomical Society of the Pacific Conference Series, Vol. 309, Astrophysics of Dust, ed. A. N. Witt, G. C. Clayton, & B. T. Draine, 33
Flower, P. J. 1996, ApJ, 469, 355
Folsom, C. P., Bagnulo, S., Wade, G. A., et al. 2012, MNRAS, 422, 2072
Fuller, G. M., Fowler, W. A., & Newman, M. J. 1985, ApJ, 293, 1
Fuller, J., Rappaport, S., Jayaraman, R., Kurtz, D., & Handler, G. 2025, ApJ, 979, 80
Gaia Collaboration, Brown, A. G. A., Vallenari, A., et al. 2021, A&A, 649, A1
Gaia Collaboration, Prusti, T., de Bruijne, J. H. J., et al. 2016, A&A, 595, A1
Gavras, P., Rimoldini, L., Nienartowicz, K., et al. 2023, A&A, 674, A22
Gray, D. F. 2008, The Observation and Analysis of Stellar Photospheres
Green, G. M., Schlafly, E. F., Finkbeiner, D., et al. 2018, MNRAS, 478, 651
Gutteridge, C., Neiner, C., Catala, C., & Folsom, C. P. 2026, A&A, 709, A43
Handler, G. 2009, in American Institute of Physics Conference Series, Vol. 1170, American Institute of Physics Conference Series, ed. J. A. Guzik & P. A. Bradley, 403–409
Heger, A., Langer, N., & Woosley, S. E. 2000, ApJ, 528, 368
Heiter, U. 2002, A&A, 381, 959
Heiter, U., Kupka, F., van't Veer-Menneret, C., et al. 2002, A&A, 392, 619
Herwig, F. 2000, A&A, 360, 952
Høg, E., Fabricius, C., Makarov, V. V., et al. 2000, A&A, 355, L27
Howell, S. B., Sobeck, C., Haas, M., et al. 2014, PASP, 126, 398
Hroch, F. 2014, Munipack: General astronomical image processing software
Hümmerich, S., Mikulášek, Z., Paunzen, E., et al. 2018, A&A, 619, A98
Iglesias, C. A. & Rogers, F. J. 1996, ApJ, 464, 943
Iglesias-Marzoa, R., López-Morales, M., & Jesús Arévalo Morales, M. 2015a, rvfit: Radial velocity curves fitting for binary stars or exoplanets, Astrophysics Source Code Library, record ascl:1505.020
Iglesias-Marzoa, R., López-Morales, M., & Jesús Arévalo Morales, M. 2015b, PASP, 127, 567
Itoh, N., Hayashi, H., Nishikawa, A., & Kohyama, Y. 1996, ApJS, 102, 411
Itoh, N., Totsuji, H., Ichimaru, S., & Dewitt, H. E. 1979, ApJ, 234, 1079
Jayaraman, R., Rappaport, S. A., Powell, B., et al. 2024, ApJ, 975, 121
Kabáth, P., Skarka, M., Hatzes, A., et al. 2026, MNRAS, 545, staf1972
Kennelly, E. J. 1994, PhD thesis, University of British Columbia, Canada
Kennelly, E. J., Walker, G. A. H., & Merryfield, W. J. 1992, ApJ, 400, L71
Kochukhov, O., Lüftinger, T., Neiner, C., Alecian, E., & MiMeS Collaboration. 2014, A&A, 565, A83
Kochukhov, O., Makaganiuk, V., & Piskunov, N. 2010a, A&A, 524, A5
Kochukhov, O., Makaganiuk, V., & Piskunov, N. 2010b, A&A, 524, A5
Krtička, J., Mikulášek, Z., Kurfürst, P., & Oksala, M. E. 2022, A&A, 659, A37
Kupka, F. G., Piskunov, N., Ryabchikova, T. A., Stempels, H. C., & Weiss, W. W. 1999, A&AS, 138, 119
Kupka, F. G., Ryabchikova, T. A., Piskunov, N. E., Stempels, H. C., & Weiss, W. W. 2000, Balt. Astron., 9, 590
Langanke, K. & Martínez-Pinedo, G. 2000, Nuclear Physics A, 673, 481
Ledoux, P. 1951, ApJ, 114, 373
Lehmann, H., Dervişoğlu, A., Mkrtichian, D. E., et al. 2020, A&A, 644, A121
Lehmann, H., Tsymbal, V., Pertermann, F., et al. 2018, A&A, 615, A131
Lenz, P. & Breger, M. 2005, Communications in Asteroseismology, 146, 53
Lightkurve Collaboration, Cardoso, J. V. d. M., Hedges, C., et al. 2018, Lightkurve: Kepler and TESS time series analysis in Python, Astrophysics Source Code Library
Magg, E., Bergemann, M., Serenelli, A., et al. 2022, A&A, 661, A140
Maksimov, A., Balega, Y. Y., Dyachenko, V., et al. 2009, Astrophysical Bulletin, 64, 296
Mathys, G. 1989, FCPh, 13, 143
Mathys, G. 2017, A&A, 601, A14
Merloni, A., Lamer, G., Liu, T., et al. 2024, A&A, 682, A34
Mikulášek, Z. 2015, A&A, 584, A8
Mikulášek, Z. 2024, in The BRITE Side of Stars. Celebrating the 10th Anniversary of BRITE Constellation, 11
Mikulášek, Z., Krtička, J., Henry, G. W., et al. 2008, A&A, 485, 585
Mikulášek, Z., Krtička, J., Shultz, M. E., et al. 2020, in Stellar Magnetism: A Workshop in Honour of the Career and Contributions of John D. Landstreet, ed. G. Wade, E. Alecian, D. Bohlender, & A. Sigut, Vol. 11, 46–53
Mkrtichian, D., Gunsriviwat, K., Lehmann, H., et al. 2022, Galaxies, 10, 97
Mkrtichian, D. E., Kusakin, A. V., Gamarova, A. Y., & Nazarenko, V. 2002, in Astronomical Society of the Pacific Conference Series, Vol. 259, IAU Colloquium 185: Radial and Nonradial Pulsationsn as Probes of Stellar Physics, ed. C. Aerts, T. R. Bedding, & J. Christensen-Dalsgaard, 96
Murphy, S. J. & Paunzen, E. 2017, MNRAS, 466, 546
Nakayama, K., Iwakiri, W. B., Enoto, T., et al. 2025, ApJ, 995, 152
Neiner, C. 2024, in The BRITE Side of Stars. Celebrating the 10th Anniversary of BRITE Constellation, 74
Oda, T., Hino, M., Muto, K., Takahara, M., & Sato, K. 1994, Atomic Data and Nuclear Data Tables, 56, 231
Panchuk, V. E., Chuntonov, G. A., & Naidenov, I. D. 2014, Astrophysical Bulletin, 69, 339
Paunzen, E. 2004, in IAU Symposium, Vol. 224, The A-Star Puzzle, ed. J. Zverko, J. Ziznovsky, S. J. Adelman, & W. W. Weiss, 443–450
Paunzen, E., Iliev, I. K., Kamp, I., & Barzova, I. S. 2002, MNRAS, 336, 1030
Paunzen, E. & Vanmunster, T. 2016, Astronomische Nachrichten, 337, 239

Paxton, B., Bildsten, L., Dotter, A., et al. 2011, ApJS, 192, 3
Paxton, B., Cantiello, M., Arras, P., et al. 2013, ApJS, 208, 4
Paxton, B., Marchant, P., Schwab, J., et al. 2015, ApJS, 220, 15
Paxton, B., Schwab, J., Bauer, E. B., et al. 2018, ApJS, 234, 34
Paxton, B., Smolec, R., Schwab, J., et al. 2019, ApJS, 243, 10
Pinsonneault, M. H., Kawaler, S. D., Sofia, S., & Demarque, P. 1989, ApJ, 338, 424
Piskunov, N. & Valenti, J. A. 2017, A&A, 597, A16
Piskunov, N. E., Kupka, F., Ryabchikova, T. A., Weiss, W. W., & Jeffery, C. S. 1995, A&AS, 112, 525
Pols, O. R., Tout, C. A., Eggleton, P. P., & Han, Z. 1995, MNRAS, 274, 964
Potekhin, A. Y. & Chabrier, G. 2010, Contributions to Plasma Physics, 50, 82
Predehl, P., Andritschke, R., Arefiev, V., et al. 2021, A&A, 647, A1
Preston, G. W. 1974, ARA&A, 12, 257
Prša, A. & Zwitter, T. 2005, ApJ, 628, 426
Ramos-Ceja, M. E., Lamer, G., Salvato, M., et al. 2026, A&A, 712, A171
Raskin, G., van Winckel, H., Hensberge, H., et al. 2011, A&A, 526, A69
Ricker, G. R., Winn, J. N., Vanderspek, R., et al. 2015, Journal of Astronomical Telescopes, Instruments, and Systems, 1, 014003
Rimoldini, L., Holl, B., Gavras, P., et al. 2023, A&A, 674, A14
Rogers, F. J. & Nayfonov, A. 2002, ApJ, 576, 1064
Ryabchikova, T., Piskunov, N., Kurucz, R. L., et al. 2015, Phys. Scr, 90, 054005
Ryabchikova, T. A., Piskunov, N. E., Kupka, F., & Weiss, W. W. 1997, Balt. Astron., 6, 244
Salpeter, E. E. 1954, Australian Journal of Physics, 7, 373
Saumon, D., Chabrier, G., & van Horn, H. M. 1995, ApJS, 99, 713
Schrijvers, C., Telting, J. H., Aerts, C., Ruymaekers, E., & Henrichs, H. F. 1997, A&AS, 121, 343
Semenko, E., Kochukhov, O., Mikulášek, Z., et al. 2024, MNRAS, 535, 2812
Semenko, E., Romanyuk, I., Yakunin, I., Kudryavtsev, D., & Moiseeva, A. 2022, MNRAS, 515, 998
Shultz, M. E., Wade, G. A., Rivinius, T., et al. 2018, MNRAS, 475, 5144
Shulyak, D., Tsymbal, V., Ryabchikova, T., Stütz, C., & Weiss, W. W. 2004, A&A, 428, 993
Sikora, J., Wade, G. A., Power, J., & Neiner, C. 2019, MNRAS, 483, 3127
Skarka, M., Kabáth, P., Paunzen, E., et al. 2019, MNRAS, 487, 4230
Soufi, F., Goupil, M. J., & Dziembowski, W. A. 1998, A&A, 334, 911
Stellingwerf, R. F. 1978, AJ, 83, 1184
Stetson, P. B. 1987, PASP, 99, 191
Suárez, J. C., Goupil, M. J., & Morel, P. 2006, A&A, 449, 673
Telting, J. H. & Schrijvers, C. 1997, A&A, 317, 723
Thomson-Paressant, K., Neiner, C., Labadie-Bartz, J., et al. 2025, A&A, 704, A134
Timmes, F. X. & Swesty, F. D. 2000, ApJS, 126, 501
Townsend, R. H. D. & Owocki, S. P. 2005, MNRAS, 357, 251
Valenti, J. A. & Piskunov, N. 1996, A&AS, 118, 595
Valenti, J. A. & Piskunov, N. 2012, SME: Spectroscopy Made Easy, Astrophysics Source Code Library, record ascl:1202.013
Čokina, M., Fedurco, M., & Parimucha, Š. 2021, A&A, 652, A156
Wade, G. A., Donati, J.-F., Landstreet, J. D., & Shorlin, S. L. S. 2000, MNRAS, 313, 851
Wade, G. A., Neiner, C., Alecian, E., et al. 2016, MNRAS, 456, 2
Walczak, P. & Daszyńska-Daszkiewicz, J. 2018, Contributions of the Astronomical Observatory Skalnate Pleso, 48, 73
Walczak, P. & Kopacz, A. 2024, MNRAS, 529, 4176
Xiong, D. R., Deng, L., Zhang, C., & Wang, K. 2016, MNRAS, 457, 3163
Zhang, V., Rappaport, S., Jayaraman, R., et al. 2024, MNRAS, 528, 3378

Appendix A: Spectroscopy log and radial velocities

Table A.1. Observational log with measured radial and rotational velocities of HD 99458.

BJD − 2 400 000	T_{exp} (s)	SNR	V_r ($km\,s^{-1}$)	$v \sin i$ ($km\,s^{-1}$)
		HERMES		
58 543.53811	600	100	1.7 ± 0.2	46.8 ± 0.4
58 543.57144	300	70	1.5 ± 0.2	48.1 ± 0.3
58 543.57549	300	70	0.9 ± 0.2	48.1 ± 0.3
58 543.57955	300	70	0.1 ± 0.2	48.2 ± 0.3
58 543.58360	300	70	0.2 ± 0.2	49.2 ± 0.3
58 543.58765	300	70	0.6 ± 0.3	49.4 ± 0.4
58 544.51535	900	135	39.2 ± 0.2	48.0 ± 0.3
58 545.49010	900	130	56.1 ± 0.2	46.7 ± 0.3
58 545.57962	900	130	49.6 ± 0.2	49.1 ± 0.3
58 546.56069	1200	155	−2.1 ± 0.2	46.8 ± 0.3
58 546.63441	1200	100	−0.8 ± 0.3	47.6 ± 0.4
58 547.59642	1200	145	61.5 ± 0.2	46.7 ± 0.3
58 549.54499	300	60	8.0 ± 0.2	50.1 ± 0.3
58 549.54904	300	70	8.4 ± 0.2	49.9 ± 0.4
58 549.55310	300	65	9.1 ± 0.2	50.1 ± 0.4
58 549.55715	300	55	9.6 ± 0.2	49.2 ± 0.4
58 549.56120	300	70	9.9 ± 0.3	47.8 ± 0.5
58 549.56525	300	80	9.9 ± 0.2	47.5 ± 0.5
58 549.56930	300	75	9.6 ± 0.2	47.5 ± 0.3
58 549.57335	300	80	9.9 ± 0.2	47.9 ± 0.3
58 549.57740	300	60	10.0 ± 0.2	48.8 ± 0.3
58 549.58146	300	70	10.5 ± 0.2	50.1 ± 0.3
58 549.58551	300	70	11.1 ± 0.3	50.5 ± 0.4
58 549.58956	300	70	11.1 ± 0.3	50.0 ± 0.4
58 549.59361	300	55	11.3 ± 0.2	48.8 ± 0.3
58 549.59766	300	55	11.6 ± 0.3	47.7 ± 0.4
58 549.60171	300	65	12.1 ± 0.2	46.7 ± 0.3
58 549.60576	300	60	12.8 ± 0.2	46.7 ± 0.4
58 549.60982	300	45	13.1 ± 0.3	47.9 ± 0.4
58 549.61387	300	50	12.9 ± 0.2	49.4 ± 0.3
58 549.61902	300	60	12.7 ± 0.3	50.9 ± 0.3
58 549.62308	300	60	12.8 ± 0.3	50.7 ± 0.4
58 551.57668	1300	140	8.1 ± 0.2	47.1 ± 0.3
58 552.64210	1400	120	35.0 ± 0.2	47.8 ± 0.3
		MRES		
58 859.38886	600	145	−1.6 ± 0.5	52.2 ± 0.1
58 859.39613	600	150	−0.3 ± 0.5	50.5 ± 0.8
58 859.40345	600	140	0.2 ± 0.4	47.5 ± 0.1
58 859.41071	600	125	−1.8 ± 0.4	50.0 ± 0.7
58 859.41799	600	140	−3.2 ± 0.7	52.0 ± 0.8
58 859.42585	600	150	−2.0 ± 0.7	52.2 ± 0.1
58 859.43313	600	155	−0.9 ± 0.6	47.5 ± 0.1
58 859.44040	600	160	−2.1 ± 0.8	52.4 ± 0.6
58 859.44767	600	160	−3.0 ± 0.3	52.4 ± 0.2
58 859.45495	600	140	−2.0 ± 0.8	52.2 ± 0.1
58 859.46223	600	130	−1.9 ± 0.9	49.7 ± 1.7
58 859.46950	600	145	−1.5 ± 0.7	47.5 ± 1.6
58 860.31411	600	145	40.9 ± 0.7	53.0 ± 0.9
58 860.32140	600	140	40.0 ± 0.5	54.3 ± 0.9
58 860.32866	600	145	39.1 ± 0.8	52.2 ± 0.4
58 860.33593	600	150	42.1 ± 0.7	48.3 ± 1.3
58 860.34329	600	150	44.0 ± 0.6	48.4 ± 1.0
58 860.35062	600	165	43.0 ± 0.5	53.6 ± 0.7
58 860.35789	600	170	42.5 ± 0.4	52.6 ± 0.4
58 860.36513	600	165	43.3 ± 0.9	51.3 ± 1.5
58 860.37242	600	160	45.6 ± 0.6	48.0 ± 1.0
58 860.38071	600	120	45.0 ± 0.6	52.7 ± 0.6
58 860.38797	600	155	45.2 ± 0.4	52.6 ± 0.4
58 860.39526	600	165	46.2 ± 0.6	51.8 ± 0.8
58 860.40255	600	170	47.6 ± 0.8	49.6 ± 1.5
58 860.40985	600	160	48.2 ± 0.5	49.3 ± 0.9
58 860.41714	600	120	46.7 ± 0.4	51.9 ± 0.5
58 860.42447	600	140	48.6 ± 0.4	52.3 ± 0.2
58 860.43184	600	155	51.0 ± 0.7	48.9 ± 1.2
58 860.43910	600	180	50.6 ± 0.7	49.4 ± 1.3
58 860.44638	600	175	47.8 ± 0.4	52.2 ± 0.1
58 860.45381	600	175	49.4 ± 0.5	52.2 ± 0.1
58 860.46108	600	170	53.7 ± 0.5	48.5 ± 0.9
58 860.46839	600	175	54.3 ± 0.6	47.5 ± 0.9
58 860.47569	600	150	51.0 ± 0.6	52.0 ± 0.6
58 861.32988	360	160	50.9 ± 0.4	52.3 ± 0.3
59 924.40243	2700	330	18.6 ± 0.5	49.1 ± 1.0
59 926.39947	1800	220	0.4 ± 0.5	52.3 ± 0.1
60 421.09276	600	105	55.4 ± 1.0	47.4 ± 1.7
60 421.10006	600	100	51.8 ± 0.7	49.8 ± 1.3
60 422.06080	300	75	−2.7 ± 0.8	52.1 ± 0.1
60 422.06455	300	70	−1.8 ± 1.0	52.1 ± 0.1
60 423.10382	600	60	59.6 ± 1.2	47.4 ± 2.1
61 069.19784	300	80	33.4 ± 0.6	49.3 ± 1.1
61 069.20159	300	85	34.3 ± 0.5	49.3 ± 1.0
61 069.20533	300	90	35.9 ± 0.4	49.9 ± 0.8
61 069.20908	300	80	36.1 ± 0.5	49.6 ± 1.0
61 069.21283	300	90	35.0 ± 0.5	52.6 ± 0.1
61 069.21658	300	90	35.2 ± 0.4	49.9 ± 0.8
61 069.22032	300	100	33.4 ± 0.6	52.6 ± 0.1
61 069.22407	300	100	32.9 ± 0.4	52.6 ± 0.3
61 069.22782	300	100	33.1 ± 0.5	52.6 ± 0.1
61 069.23156	300	100	31.9 ± 0.6	52.6 ± 0.1
61 069.23531	300	100	32.2 ± 0.5	48.5 ± 1.2
61 069.23906	300	100	32.2 ± 0.5	48.5 ± 0.1
61 069.24280	300	110	33.5 ± 0.4	49.2 ± 0.8
61 069.24655	300	100	33.8 ± 0.4	50.2 ± 0.8
61 069.25030	300	110	34.2 ± 0.4	49.3 ± 0.7
61 069.25403	300	105	32.1 ± 0.4	52.6 ± 0.1
61 069.25779	300	100	31.7 ± 0.6	52.6 ± 0.1
61 069.26152	300	110	30.6 ± 0.4	52.6 ± 0.1
61 069.26527	300	100	29.1 ± 0.5	52.6 ± 0.1
61 069.26902	300	95	28.8 ± 0.6	52.6 ± 0.1
61 069.27276	300	95	29.7 ± 0.5	51.7 ± 1.0
61 069.27651	300	95	30.7 ± 0.5	50.6 ± 1.0
61 069.28026	300	100	31.2 ± 0.4	48.5 ± 0.1
61 069.28400	300	105	31.8 ± 0.4	48.5 ± 0.1
61 069.28775	300	105	30.6 ± 0.4	49.3 ± 0.8
61 069.29150	300	110	30.7 ± 0.5	50.9 ± 0.9

Table A.1. continued

BJD − 2 400 000	T_{exp} (s)	SNR	V_r (km s^{-1})	$\upsilon \sin i$ (km s^{-1})
61 069.29524	300	110	28.0 ± 0.5	52.6 ± 0.1
61 069.29899	300	105	27.3 ± 0.5	52.6 ± 0.1
61 069.30273	300	105	26.9 ± 0.5	52.6 ± 0.1
61 069.30648	300	100	25.9 ± 0.5	52.6 ± 0.1
61 069.31023	300	100	28.6 ± 0.5	48.8 ± 0.9
61 069.31397	300	100	28.2 ± 0.6	50.6 ± 1.1
61 069.31772	300	90	29.8 ± 0.6	48.5 ± 0.1
61 069.32147	300	90	28.9 ± 0.5	47.9 ± 1.0
61 069.32521	300	95	29.5 ± 0.4	48.5 ± 1.0
61 069.32896	300	95	27.6 ± 0.6	49.2 ± 1.0
61 069.33270	300	90	24.9 ± 0.6	52.6 ± 0.1
61 069.33645	300	95	24.1 ± 0.5	52.6 ± 0.1
61 069.34020	300	90	23.4 ± 0.5	52.6 ± 0.1
61 069.34394	300	90	22.8 ± 0.5	52.6 ± 0.1
61 069.34769	300	80	25.0 ± 0.6	52.6 ± 0.3
61 069.35143	300	80	26.9 ± 0.5	48.5 ± 0.1
61 069.35518	300	85	27.0 ± 0.5	48.3 ± 1.2
61 069.35893	300	75	27.0 ± 0.5	48.5 ± 0.1
61 069.36267	300	85	24.4 ± 0.5	50.3 ± 0.9
61 069.36642	300	90	22.8 ± 0.6	51.4 ± 1.1
61 069.37017	300	90	20.7 ± 0.6	52.2 ± 0.9
61 069.37390	300	80	20.2 ± 0.5	52.6 ± 0.1
61 069.37765	300	75	20.2 ± 0.5	52.6 ± 0.1
61 069.38140	300	90	22.9 ± 0.6	52.6 ± 0.1
61 069.38514	300	80	23.0 ± 0.6	50.0 ± 1.0
61 069.38889	300	80	23.2 ± 0.5	48.5 ± 0.1
61 069.39264	300	80	22.8 ± 0.6	49.3 ± 1.1
61 069.39639	300	80	22.0 ± 0.7	49.7 ± 1.3
61 069.40013	300	80	20.4 ± 0.7	52.6 ± 0.1
61 069.40388	300	65	19.2 ± 0.7	52.6 ± 0.1
61 069.40763	300	75	18.8 ± 0.7	52.6 ± 0.1
61 069.41138	300	75	19.0 ± 0.6	52.6 ± 0.1
61 069.41513	300	80	18.8 ± 0.7	52.6 ± 0.1
61 069.41887	300	75	19.7 ± 0.7	49.4 ± 1.4
61 069.42262	300	60	20.4 ± 0.8	49.8 ± 1.5
61 069.42637	300	60	19.4 ± 0.7	52.6 ± 0.2
61 070.22048	300	90	4.8 ± 0.4	51.8 ± 0.5
61 070.22423	300	90	5.1 ± 0.5	51.9 ± 0.6
61 070.22797	300	93	4.5 ± 0.7	51.4 ± 0.1
61 070.23171	300	95	4.7 ± 0.5	48.5 ± 1.0
61 070.23545	300	95	5.4 ± 0.4	47.4 ± 0.1
61 070.23920	300	100	4.9 ± 0.4	47.4 ± 0.9
61 070.24293	300	100	6.2 ± 0.4	47.4 ± 0.1
61 070.24667	300	100	5.5 ± 0.6	49.7 ± 1.2
61 070.25041	300	90	5.4 ± 0.5	51.4 ± 0.1
61 070.25416	300	90	5.5 ± 0.3	51.3 ± 0.2
61 070.25790	300	90	6.3 ± 0.5	51.4 ± 0.1
61 070.26164	300	90	6.1 ± 0.7	51.4 ± 0.1
61 070.26538	300	90	6.2 ± 0.6	50.3 ± 1.2
61 070.26913	300	90	7.4 ± 0.4	47.5 ± 0.8
61 070.27287	300	90	6.8 ± 0.4	47.4 ± 0.1
61 070.27661	300	90	7.9 ± 0.5	47.4 ± 0.1
61 070.28034	300	90	7.8 ± 0.6	49.5 ± 1.2
61 070.28408	300	90	6.8 ± 0.6	51.4 ± 0.1
61 070.28783	300	95	7.7 ± 0.4	51.4 ± 0.1
61 070.29157	300	90	8.1 ± 0.5	51.4 ± 0.1

Table A.1. continued

BJD − 2 400 000	T_{exp} (s)	SNR	V_r (km s^{-1})	$\upsilon \sin i$ (km s^{-1})
61 070.29531	300	90	8.4 ± 0.6	49.4 ± 1.2
61 070.29905	300	85	8.5 ± 0.7	49.6 ± 1.4
61 070.30280	300	80	8.4 ± 0.5	51.4 ± 0.1
61 070.30654	300	90	9.2 ± 0.4	47.4 ± 0.7
61 070.31028	300	90	9.6 ± 0.6	48.8 ± 1.1
61 070.31402	300	90	10.5 ± 0.5	47.9 ± 1.0
61 070.31775	300	85	10.7 ± 0.5	47.4 ± 1.1
61 070.32150	300	80	10.9 ± 0.5	48.0 ± 0.9
61 070.32524	300	80	10.6 ± 0.5	49.4 ± 1.0
61 070.32898	300	80	11.0 ± 0.5	47.4 ± 0.1
61 070.33272	300	80	11.2 ± 0.8	51.4 ± 0.1
61 070.33647	300	80	10.6 ± 0.6	51.4 ± 0.1
61 070.34021	300	90	11.0 ± 0.4	51.3 ± 0.3
61 070.34395	300	90	11.0 ± 0.4	51.7 ± 0.4
61 070.34769	300	85	10.6 ± 0.5	51.5 ± 0.4
61 070.35144	300	90	12.9 ± 0.7	47.6 ± 1.2
61 070.35518	300	90	13.4 ± 0.6	47.4 ± 1.0
61 070.35891	300	85	14.2 ± 0.3	47.4 ± 0.1
61 070.36265	300	85	13.5 ± 0.5	48.3 ± 0.9
61 070.36640	300	85	12.7 ± 0.7	51.4 ± 0.1
61 070.37014	300	85	12.1 ± 0.8	51.4 ± 0.1
61 070.37388	300	80	12.9 ± 0.4	51.4 ± 0.1
61 070.37762	300	85	12.2 ± 0.5	51.8 ± 0.5
61 070.38137	300	80	14.6 ± 0.6	48.3 ± 1.2
61 070.38511	300	80	15.1 ± 0.6	47.4 ± 0.1
61 070.38885	300	80	15.5 ± 0.7	48.7 ± 1.4
61 070.39259	300	80	16.1 ± 0.5	48.2 ± 0.9
61 070.39632	300	80	15.5 ± 0.5	51.4 ± 0.1
61 070.40007	300	80	15.4 ± 0.7	49.2 ± 1.4
61 070.40381	300	80	15.3 ± 0.9	51.4 ± 0.3
61 070.40755	300	80	14.6 ± 0.6	49.7 ± 1.1
61 070.41129	300	80	14.9 ± 0.3	50.1 ± 0.6
61 070.41503	300	80	16.1 ± 0.4	48.5 ± 0.7
61 070.41878	300	80	16.4 ± 0.7	49.2 ± 1.4
61 070.42252	300	80	18.6 ± 0.8	48.1 ± 1.4
61 070.42626	300	80	18.1 ± 0.6	49.5 ± 1.2
61 070.43000	300	80	18.2 ± 0.6	48.2 ± 1.0
61 070.43375	300	80	18.3 ± 0.7	48.5 ± 1.4
61 070.43748	300	80	18.3 ± 0.9	51.4 ± 0.1
61 070.44122	300	80	17.7 ± 0.7	50.2 ± 1.4
61 070.44496	300	85	18.9 ± 0.5	48.4 ± 0.8
61 070.44871	300	80	19.2 ± 0.5	48.8 ± 1.0
61 070.45245	300	85	19.7 ± 0.7	49.6 ± 1.3
61 070.45619	300	85	20.1 ± 0.7	49.3 ± 1.4
61 070.45993	300	90	20.9 ± 0.5	47.8 ± 0.9
61 070.46367	300	85	21.0 ± 0.6	49.5 ± 1.2
61 070.46742	300	85	21.7 ± 0.7	48.8 ± 1.2
61 071.21460	300	110	66.6 ± 0.2	49.7 ± 0.5
61 071.21835	300	110	67.1 ± 0.3	47.4 ± 0.1
61 071.22209	300	105	67.2 ± 0.6	47.4 ± 1.1
61 071.22584	300	105	66.6 ± 0.6	51.5 ± 0.4
61 071.22959	300	100	67.1 ± 0.4	47.4 ± 0.8
61 071.23334	300	100	66.4 ± 0.4	49.3 ± 0.8
61 071.23708	300	100	65.8 ± 0.5	51.4 ± 0.1
61 071.24083	300	95	65.5 ± 0.7	51.4 ± 0.1
61 071.24458	300	90	64.6 ± 0.7	51.4 ± 0.1

Table A.1. continued

BJD − 2 400 000	T_{exp} (s)	SNR	V_r (km s^{-1})	$\upsilon \sin i$ (km s^{-1})
61 071.24831	300	90	65.7 ± 0.5	49.3 ± 0.9
61 071.25206	300	90	65.7 ± 0.5	47.5 ± 0.9
61 071.25582	300	85	66.3 ± 0.7	47.5 ± 1.3
61 071.25955	300	70	67.3 ± 0.6	47.5 ± 0.1
61 071.26330	300	70	66.7 ± 0.6	48.5 ± 1.2
61 071.26704	300	70	65.6 ± 0.5	51.4 ± 0.4
61 071.27079	300	75	65.5 ± 0.7	51.4 ± 0.1
61 071.27454	300	80	65.1 ± 0.7	51.4 ± 0.1
61 071.27828	300	80	65.0 ± 0.7	51.4 ± 0.1
61 071.28203	300	75	64.7 ± 0.6	51.4 ± 0.1
61 071.28578	300	75	66.7 ± 0.5	47.6 ± 0.9
61 071.28952	300	70	66.0 ± 0.6	47.5 ± 0.1
61 071.29327	300	60	66.4 ± 0.8	47.6 ± 1.3
61 071.29701	300	65	66.2 ± 0.5	50.1 ± 1.0
61 071.30076	300	65	66.1 ± 0.5	51.6 ± 0.4
61 071.30451	300	70	65.4 ± 0.7	51.5 ± 0.5
61 071.30826	300	65	66.0 ± 0.7	50.7 ± 1.3
61 071.31200	300	65	64.0 ± 0.6	51.4 ± 0.1
61 071.31575	300	70	65.8 ± 0.5	50.1 ± 1.0
61 071.31950	300	75	65.1 ± 0.6	48.0 ± 1.1
61 071.32324	300	90	65.9 ± 0.4	48.2 ± 0.6
61 071.32699	300	85	66.4 ± 0.4	47.5 ± 0.1
61 071.33074	300	90	66.8 ± 0.6	49.4 ± 1.1
61 071.33448	300	95	65.7 ± 0.4	50.8 ± 0.6
61 071.33823	300	110	65.7 ± 0.4	51.4 ± 0.1
61 071.34198	300	110	65.1 ± 0.4	51.4 ± 0.1
61 071.34572	300	115	65.7 ± 0.3	51.4 ± 0.1
61 071.34947	300	130	65.1 ± 0.4	48.9 ± 0.7
61 071.35321	300	130	65.6 ± 0.3	48.6 ± 0.6
61 071.35696	300	135	65.8 ± 0.4	48.0 ± 0.7
61 071.36071	300	130	65.7 ± 0.3	48.8 ± 0.6
61 071.36445	300	135	65.0 ± 0.3	49.6 ± 0.6
61 071.36820	300	135	65.4 ± 0.3	49.4 ± 0.5
61 071.37195	300	130	65.2 ± 0.3	50.8 ± 0.6
61 071.37568	300	120	64.5 ± 0.3	51.4 ± 0.1
61 071.37943	300	130	65.1 ± 0.4	49.7 ± 0.8
61 071.38318	300	130	65.3 ± 0.4	49.0 ± 0.8
61 071.38692	300	130	64.6 ± 0.3	51.4 ± 0.2
61 071.39067	300	130	64.4 ± 0.3	50.2 ± 0.6
61 071.39442	300	125	64.1 ± 0.5	50.3 ± 0.9
61 071.39816	300	120	64.4 ± 0.5	49.0 ± 0.9
61 071.40191	300	130	64.2 ± 0.4	49.1 ± 0.8
61 071.40566	300	135	64.9 ± 0.3	47.8 ± 0.5
61 071.40940	300	130	64.9 ± 0.4	48.0 ± 0.7
61 071.41315	300	110	65.7 ± 0.5	49.2 ± 0.9
61 071.41690	300	120	65.6 ± 0.5	49.4 ± 0.9
61 071.42064	300	120	64.8 ± 0.4	51.0 ± 0.7
61 071.42439	300	130	64.0 ± 0.2	51.4 ± 0.1
61 071.42814	300	130	62.4 ± 0.5	51.4 ± 0.1
61 071.43188	300	125	63.3 ± 0.7	50.5 ± 1.2
61 071.43563	300	120	62.4 ± 0.5	48.9 ± 1.0
61 071.43938	300	105	63.1 ± 0.4	47.5 ± 0.1
61 071.44312	300	105	63.9 ± 0.4	48.7 ± 0.8
61 071.44687	300	105	65.3 ± 0.6	49.5 ± 1.1
61 071.45062	300	110	64.8 ± 0.7	50.5 ± 1.4
61 071.45436	300	115	64.5 ± 0.6	53.3 ± 1.1

Table A.1. continued

BJD − 2 400 000	T_{exp} (s)	SNR	V_r (km s^{-1})	$\upsilon \sin i$ (km s^{-1})
61 071.45811	300	110	64.1 ± 0.5	52.5 ± 0.6
61 071.46186	300	105	62.2 ± 0.6	51.4 ± 0.1
61 071.46560	300	95	61.6 ± 0.9	50.1 ± 1.8
61 071.46935	300	100	61.7 ± 0.8	47.5 ± 1.4
61 072.21496	300	120	10.5 ± 0.5	51.3 ± 0.1
61 072.21871	300	110	10.1 ± 0.5	51.3 ± 0.1
61 072.22245	300	110	10.1 ± 0.4	51.4 ± 0.3
61 072.22620	300	105	13.1 ± 0.4	47.4 ± 0.7
61 072.22995	300	100	12.0 ± 0.4	47.4 ± 0.7
61 072.23370	300	100	11.7 ± 0.5	47.0 ± 0.9
61 072.23744	300	100	11.2 ± 0.5	47.4 ± 0.1
61 072.24119	300	120	10.8 ± 0.6	49.9 ± 1.1
61 072.24494	300	110	10.4 ± 0.5	51.4 ± 0.1
61 072.24868	300	105	10.4 ± 0.4	51.4 ± 0.1
61 072.25243	300	100	10.6 ± 0.4	51.4 ± 0.1
61 072.25618	300	110	10.7 ± 0.4	49.2 ± 0.8
61 072.25992	300	120	11.1 ± 0.4	47.4 ± 0.1
61 072.26367	300	115	9.1 ± 0.4	47.4 ± 0.1
61 072.26741	300	105	9.4 ± 0.4	47.4 ± 0.1
61 072.27116	300	105	8.5 ± 0.6	47.8 ± 1.0
61 072.27491	300	115	8.3 ± 0.7	48.7 ± 1.2
61 072.27866	300	110	8.5 ± 0.6	51.4 ± 0.1
61 072.28240	300	115	8.6 ± 0.4	51.4 ± 0.1
61 072.28615	300	110	9.2 ± 0.3	51.4 ± 0.1
61 072.28989	300	105	10.0 ± 0.4	48.0 ± 0.8
61 072.29364	300	125	8.9 ± 0.5	47.4 ± 0.9
61 072.29739	300	125	8.1 ± 0.4	47.4 ± 0.1
61 072.30113	300	125	6.6 ± 0.5	48.4 ± 0.9
61 072.30488	300	130	5.9 ± 0.6	49.5 ± 1.1
61 072.30863	300	110	5.5 ± 0.6	51.4 ± 0.1
61 072.31237	300	125	5.9 ± 0.7	51.4 ± 0.1
61 072.31612	300	115	6.7 ± 0.6	51.4 ± 0.1
61 072.31986	300	110	7.5 ± 0.4	49.7 ± 0.8
61 072.32361	300	115	7.8 ± 0.6	49.3 ± 1.1
61 072.32736	300	115	6.2 ± 0.6	48.4 ± 1.1
61 072.33110	300	115	6.6 ± 0.5	47.4 ± 0.1
61 072.33485	300	120	5.2 ± 0.5	48.1 ± 0.8
61 072.33860	300	115	3.7 ± 0.4	51.4 ± 0.1
61 072.34233	300	120	3.9 ± 0.6	51.4 ± 0.1
61 072.34608	300	115	4.7 ± 0.8	49.2 ± 1.6
61 072.34983	300	100	5.4 ± 0.8	49.4 ± 1.5
61 072.35357	300	105	6.6 ± 0.5	48.8 ± 1.0
61 072.35732	300	100	6.1 ± 0.5	48.5 ± 0.9
61 072.36107	300	130	5.1 ± 0.5	47.4 ± 0.1
61 072.36481	300	135	3.0 ± 0.6	47.5 ± 1.0
61 072.36856	300	140	1.5 ± 0.4	51.7 ± 0.4
61 072.37231	300	140	1.7 ± 0.4	51.4 ± 0.1
61 072.37605	300	145	2.5 ± 0.6	49.3 ± 1.2
61 072.37980	300	140	3.8 ± 0.7	48.7 ± 1.4
61 072.38354	300	135	4.1 ± 0.7	48.5 ± 1.3
61 072.38729	300	130	4.3 ± 0.5	49.7 ± 0.9
61 072.39104	300	140	4.3 ± 0.4	48.1 ± 0.7
61 072.39478	300	135	3.1 ± 0.4	48.2 ± 0.7
61 072.39853	300	135	1.4 ± 0.5	49.1 ± 0.9
61 072.40228	300	140	0.9 ± 0.5	49.5 ± 1.0
61 072.40602	300	140	0.3 ± 0.4	50.9 ± 0.6

Table A.1. continued

BJD − 2 400 000	T_{exp} (s)	SNR	V_r (km s^{-1})	$\upsilon \sin i$ (km s^{-1})
61 072.40977	300	130	0.6 ± 0.4	51.4 ± 0.1
61 072.41351	300	130	1.9 ± 0.5	49.1 ± 1.0
61 072.41726	300	130	2.4 ± 0.5	50.5 ± 0.9
61 072.42101	300	125	2.7 ± 0.5	51.4 ± 0.1
61 072.42476	300	125	2.4 ± 0.6	49.4 ± 1.1
61 072.42850	300	130	1.2 ± 0.3	48.8 ± 0.6
61 072.43225	300	125	−0.0 ± 0.5	49.6 ± 0.9
61 072.43599	300	110	−0.8 ± 0.6	50.4 ± 1.0
61 072.43974	300	105	−0.4 ± 0.5	50.0 ± 1.0
61 072.44349	300	90	0.1 ± 0.5	50.3 ± 0.9
61 072.44723	300	85	0.3 ± 0.4	51.4 ± 0.1
61 072.45098	300	100	0.7 ± 0.5	51.4 ± 0.1
61 072.45471	300	110	1.0 ± 0.5	51.4 ± 0.1
61 072.45846	300	105	0.7 ± 0.5	49.3 ± 1.0
61 072.46221	300	105	−0.5 ± 0.4	48.7 ± 0.8
61 102.11691	300	90	15.0 ± 0.6	53.7 ± 0.9
61 102.12066	300	85	18.0 ± 0.7	53.4 ± 1.0
61 102.12440	300	65	17.2 ± 1.3	47.4 ± 2.1
61 102.12815	300	60	16.0 ± 1.1	47.0 ± 1.3
61 102.13189	300	70	15.0 ± 1.3	52.1 ± 0.1
61 102.13564	300	75	14.2 ± 1.2	52.1 ± 0.1
61 102.13938	300	75	14.4 ± 1.2	52.1 ± 0.1
61 102.14313	300	90	15.0 ± 0.8	47.4 ± 1.3
61 102.14687	300	85	13.2 ± 1.0	50.4 ± 1.7
61 102.15062	300	90	14.9 ± 0.8	52.1 ± 0.1
61 102.15435	300	90	15.5 ± 0.6	47.4 ± 0.1
61 102.15810	300	80	15.3 ± 0.9	47.4 ± 1.5
61 102.16184	300	100	15.6 ± 0.6	47.4 ± 0.1
61 102.16559	300	105	12.7 ± 1.0	49.8 ± 1.8
61 102.16933	300	105	12.2 ± 1.1	49.1 ± 1.9
61 102.17307	300	115	12.1 ± 0.7	47.4 ± 1.7
61 102.17682	300	120	12.4 ± 0.8	52.1 ± 0.2
61 102.18056	300	120	10.5 ± 0.8	52.1 ± 0.1
61 102.18431	300	125	11.4 ± 0.6	52.1 ± 0.1
61 102.18805	300	130	12.2 ± 0.7	49.6 ± 1.2
61 102.19180	300	130	10.9 ± 0.7	52.1 ± 0.1
61 102.19554	300	130	11.6 ± 0.5	52.4 ± 0.4
61 102.19929	300	125	10.3 ± 0.6	52.1 ± 0.1
61 102.20302	300	130	9.0 ± 0.7	52.1 ± 0.1
61 102.20677	300	125	8.2 ± 0.8	52.1 ± 0.1
61 102.21051	300	130	9.0 ± 0.9	49.0 ± 1.6
61 102.21426	300	135	8.9 ± 0.6	48.6 ± 1.0
61 102.21800	300	135	10.9 ± 0.7	47.6 ± 1.1
61 102.22175	300	140	8.9 ± 0.7	50.3 ± 1.3
61 102.22549	300	140	8.7 ± 0.6	52.2 ± 0.4
61 102.22924	300	140	9.6 ± 0.4	52.9 ± 0.5
61 102.23298	300	130	8.9 ± 0.6	52.2 ± 0.1
61 102.23673	300	135	7.8 ± 0.6	52.2 ± 0.3
61 102.24047	300	130	7.7 ± 0.7	52.2 ± 0.1
61 102.24422	300	130	7.3 ± 0.8	52.2 ± 0.1
61 102.24796	300	135	6.2 ± 0.7	49.3 ± 1.3
61 102.25171	300	130	7.8 ± 0.7	52.2 ± 0.1
61 102.25544	300	135	7.6 ± 0.6	49.7 ± 1.1
61 102.25918	300	135	7.0 ± 0.8	49.8 ± 1.3
61 102.26293	300	125	7.8 ± 0.6	51.5 ± 0.9
61 102.26667	300	125	9.3 ± 0.8	49.9 ± 1.4

Table A.1. continued

BJD − 2 400 000	T_{exp} (s)	SNR	V_r (km s^{-1})	$\upsilon \sin i$ (km s^{-1})
61 102.27042	300	130	7.4 ± 0.5	52.2 ± 0.1
61 102.27416	300	130	5.0 ± 0.7	52.2 ± 0.1
61 102.27791	300	130	6.4 ± 0.8	52.2 ± 0.2
61 102.28165	300	130	4.3 ± 0.8	50.5 ± 1.5
61 102.28540	300	125	3.9 ± 0.8	47.4 ± 1.3
61 102.28914	300	130	5.0 ± 0.8	52.2 ± 0.1
61 102.29289	300	125	5.6 ± 0.5	47.4 ± 0.1
61 102.29663	300	125	7.2 ± 0.7	47.7 ± 1.2
61 102.30038	300	125	7.3 ± 0.7	49.9 ± 1.3
61 102.30411	300	135	4.8 ± 0.4	49.9 ± 0.8
61 102.30785	300	130	5.4 ± 0.7	52.7 ± 0.8
61 102.31160	300	140	3.3 ± 0.8	52.1 ± 0.2
61 102.31534	300	130	1.7 ± 0.9	52.2 ± 0.1
61 102.31909	300	135	1.9 ± 0.8	52.2 ± 0.1
61 102.32283	300	130	0.5 ± 0.7	52.2 ± 0.1
61 102.32658	300	120	3.5 ± 0.9	47.7 ± 1.5
61 102.33032	300	110	4.8 ± 0.6	47.4 ± 0.1
61 102.33407	300	120	5.5 ± 0.7	49.0 ± 1.3
61 102.33781	300	120	5.1 ± 0.8	53.5 ± 1.1
61 102.34156	300	120	3.0 ± 0.8	52.1 ± 0.3
61 102.34530	300	120	3.2 ± 1.0	52.2 ± 0.1
61 102.34905	300	120	1.3 ± 0.9	52.2 ± 0.1
61 102.35278	300	110	0.5 ± 0.8	52.2 ± 0.1
61 102.35653	300	110	1.6 ± 1.0	52.2 ± 0.1
61 102.36027	300	110	2.4 ± 0.7	47.7 ± 1.1
61 102.36401	300	105	3.6 ± 0.8	47.4 ± 0.1
61 102.36776	300	110	4.0 ± 0.9	49.3 ± 1.6
61 102.37150	300	110	5.2 ± 0.8	48.7 ± 1.3
61 102.37525	300	110	2.6 ± 0.7	51.3 ± 1.2
61 102.37899	300	100	2.3 ± 1.2	52.2 ± 0.1
61 102.38274	300	95	0.8 ± 1.3	52.2 ± 0.1
61 102.38648	300	85	−1.8 ± 1.0	52.2 ± 0.1
61 102.39023	300	75	−0.3 ± 0.9	52.2 ± 0.1
61 102.39397	300	80	−2.2 ± 1.2	52.7 ± 1.4
61 102.39772	300	80	0.8 ± 0.9	47.4 ± 0.1
61 102.40145	300	80	−0.3 ± 1.3	48.1 ± 2.2
61 102.40520	300	65	0.1 ± 1.3	52.2 ± 0.1
61 102.40894	300	45	0.2 ± 1.6	53.4 ± 2.2
61 102.41269	300	45	−0.1 ± 1.6	57.1 ± 2.5
61 102.41643	300	45	1.7 ± 1.7	54.4 ± 2.8
61 102.42018	300	60	−0.4 ± 1.6	52.2 ± 0.2
61 102.42392	300	65	0.9 ± 1.4	47.4 ± 0.1
61 102.42766	300	65	−1.7 ± 1.8	52.2 ± 0.1
61 103.18414	900	190	24.5 ± 0.8	51.0 ± 1.3
61 104.19826	900	180	61.9 ± 0.6	48.7 ± 1.1
PLATOSpec				
60 850.47538	400	47	58.5 ± 0.4	48.0 ± 0.6
60 850.48007	400	49	58.7 ± 0.4	48.5 ± 0.6
60 850.48477	400	47	58.5 ± 0.4	48.7 ± 0.6
60 850.48947	400	45	58.8 ± 0.4	49.3 ± 0.6
60 850.49417	400	46	59.2 ± 0.4	48.9 ± 0.5
60 850.49887	400	43	59.1 ± 0.4	46.5 ± 0.5
60 850.50357	400	42	60.2 ± 0.4	46.0 ± 0.6
60 850.50827	400	39	60.5 ± 0.4	46.3 ± 0.5
60 850.51297	400	41	60.9 ± 0.3	48.2 ± 0.5
60 850.51767	400	39	61.4 ± 0.4	48.5 ± 0.0

Table A.1. continued

BJD − 2 400 000	T_{exp} (s)	SNR	V_r (km s^{-1})	$\upsilon \sin i$ (km s^{-1})
60 850.52496	400	38	61.0 ± 0.4	48.9 ± 0.6
60 850.52966	400	37	60.5 ± 0.3	46.8 ± 0.5
60 850.53436	400	36	60.5 ± 0.4	45.9 ± 0.6
60 850.53906	400	34	61.5 ± 0.4	45.9 ± 0.5
60 850.54376	400	34	62.4 ± 0.3	48.0 ± 0.5
60 850.54846	400	35	63.4 ± 0.4	48.5 ± 0.5
60 850.55316	400	36	63.1 ± 0.4	49.9 ± 0.5
60 850.55786	400	34	62.7 ± 0.5	49.2 ± 0.7
60 850.56256	400	36	61.7 ± 0.4	47.7 ± 0.5
60 850.56726	400	36	62.0 ± 0.4	45.9 ± 0.5
60 850.57212	400	36	62.8 ± 0.4	46.0 ± 0.6
60 850.57682	400	36	63.7 ± 0.3	46.3 ± 0.5
		Whoppshel		
60 845.24571	300	41	66.1 ± 0.4	49.4 ± 0.4
60 845.24923	300	40	67.2 ± 0.4	48.7 ± 0.6
60 845.25276	300	39	68.1 ± 0.4	48.5 ± 0.6
60 845.25628	300	37	67.4 ± 0.5	49.8 ± 0.7
60 845.25980	300	38	66.3 ± 0.4	49.4 ± 0.5
60 846.25584	300	50	15.0 ± 0.3	47.2 ± 0.4
60 846.25937	300	37	14.5 ± 0.3	47.0 ± 0.5
60 846.26288	300	37	16.3 ± 0.3	48.5 ± 0.5
60 846.26641	300	37	15.8 ± 0.3	48.7 ± 0.5
60 846.26993	300	23	16.0 ± 0.5	41.6 ± 0.8
60 847.23221	300	33	17.3 ± 0.3	49.1 ± 0.6
60 847.23572	300	34	19.5 ± 0.3	46.2 ± 0.5
60 847.23924	300	31	20.3 ± 0.4	45.6 ± 0.6
60 847.24275	300	31	20.7 ± 0.4	47.3 ± 0.5
60 847.24627	300	30	22.4 ± 0.4	48.4 ± 0.7
60 847.24978	300	33	21.3 ± 0.3	50.9 ± 0.6
60 847.25329	300	32	21.1 ± 0.3	53.1 ± 0.4
60 847.25680	300	33	21.9 ± 0.3	51.4 ± 0.5
60 847.26032	300	30	22.2 ± 0.4	52.2 ± 0.6
60 847.26383	300	31	22.1 ± 0.3	50.2 ± 0.4
60 847.26734	300	31	22.5 ± 0.2	50.0 ± 0.2
60 847.27086	300	35	23.1 ± 0.3	48.4 ± 0.5
60 847.27437	300	33	23.4 ± 0.4	46.5 ± 0.7
60 847.27788	300	30	23.5 ± 0.3	46.0 ± 0.6
60 847.28140	300	29	24.7 ± 0.3	50.4 ± 0.5
60 851.26311	300	21	49.3 ± 0.5	53.6 ± 0.7
60 851.26662	300	20	49.6 ± 0.6	54.8 ± 1.0
60 851.27013	300	22	48.8 ± 0.5	50.5 ± 0.8
60 851.27365	300	20	46.5 ± 0.4	45.9 ± 0.7
60 851.27716	300	19	48.0 ± 0.4	48.2 ± 0.7
60 851.28067	300	17	46.8 ± 0.6	48.4 ± 0.9
60 852.24202	180	27	−2.6 ± 0.4	51.4 ± 0.0
60 852.24415	180	31	−2.1 ± 0.4	50.7 ± 0.7
60 852.24627	180	34	−2.3 ± 0.4	50.3 ± 0.5
60 852.24839	180	32	−2.6 ± 0.4	50.3 ± 0.6
60 852.25052	180	25	−2.7 ± 0.4	48.4 ± 0.6
60 852.25265	180	29	−1.5 ± 0.4	48.4 ± 0.7
60 852.25477	180	25	−0.7 ± 0.4	46.5 ± 0.8
60 852.25689	180	30	−0.2 ± 0.4	47.8 ± 0.6
60 852.25902	180	25	−0.6 ± 0.4	48.4 ± 0.6
60 852.26115	180	27	0.1 ± 0.4	50.0 ± 0.5
60 852.26327	180	29	0.7 ± 0.4	48.4 ± 0.6
60 852.26540	180	32	−0.1 ± 0.5	49.2 ± 0.8

Table A.1. continued

BJD − 2 400 000	T_{exp} (s)	SNR	V_r (km s^{-1})	$\upsilon \sin i$ (km s^{-1})
60 852.26752	180	29	−0.7 ± 0.5	51.1 ± 0.9
60 852.26965	180	31	−0.7 ± 0.5	51.1 ± 0.8
60 852.27177	180	25	−0.9 ± 0.5	51.4 ± 0.0
60 852.27399	180	26	−0.9 ± 0.4	51.8 ± 0.6
60 852.27612	180	25	−1.2 ± 0.4	51.6 ± 0.7
60 852.27824	180	26	−1.6 ± 0.4	51.6 ± 0.6
60 852.28037	180	22	−1.5 ± 0.5	49.9 ± 0.4
60 852.28250	180	21	1.0 ± 0.5	51.9 ± 0.9
60 852.28462	180	20	−1.0 ± 0.6	51.0 ± 0.9
60 852.28675	180	20	−2.0 ± 0.7	49.7 ± 1.2
60 852.28887	180	22	−0.2 ± 0.6	46.4 ± 1.1
60 852.29100	180	25	1.0 ± 0.6	47.9 ± 1.0
60 852.29313	180	21	3.3 ± 0.7	48.7 ± 1.2
60 853.22767	300	31	60.5 ± 1.2	48.4 ± 1.9
60 853.23118	300	25	60.8 ± 0.8	48.4 ± 1.2
60 853.23470	300	35	60.7 ± 0.3	50.3 ± 0.4
60 853.23821	300	33	60.4 ± 0.2	49.1 ± 0.4
60 853.24173	300	37	59.5 ± 0.3	49.3 ± 0.6
60 853.24524	300	34	60.2 ± 0.4	49.9 ± 0.3
60 853.24875	300	31	60.6 ± 0.3	48.4 ± 0.5
60 853.25227	300	31	60.7 ± 0.2	48.4 ± 0.4
60 853.25578	300	31	61.5 ± 0.3	49.4 ± 0.5
60 853.25929	300	29	62.5 ± 0.3	48.4 ± 0.5
60 853.26281	300	30	63.4 ± 0.3	48.4 ± 0.5
60 853.26632	300	23	62.8 ± 0.4	48.7 ± 0.6
60 853.26984	300	30	62.2 ± 0.2	49.1 ± 0.4
60 853.27335	300	29	62.2 ± 0.3	49.4 ± 0.6
60 853.27686	300	27	62.5 ± 0.3	49.9 ± 0.2
60 853.28041	300	32	62.1 ± 0.4	48.5 ± 0.6
60 853.28393	300	31	62.6 ± 0.4	49.9 ± 0.0
60 853.28744	300	25	61.9 ± 0.4	49.9 ± 0.0
60 853.29096	300	26	63.4 ± 0.5	48.6 ± 0.8
60 853.29447	300	21	63.7 ± 0.4	45.9 ± 0.7
60 854.24665	300	15	28.2 ± 0.8	51.6 ± 1.3
60 854.25016	300	16	29.3 ± 0.8	51.6 ± 1.3
60 854.25368	300	19	29.6 ± 0.5	51.6 ± 0.9
60 854.25719	300	19	30.3 ± 0.6	53.3 ± 0.8
60 854.26071	300	16	29.0 ± 0.8	54.4 ± 1.3
60 854.26422	300	17	26.8 ± 0.6	51.2 ± 1.0
60 854.26773	300	18	27.7 ± 0.6	52.1 ± 1.1
60 854.27125	300	17	26.3 ± 0.7	49.6 ± 1.3
60 854.27476	300	18	25.9 ± 0.6	48.2 ± 1.0
60 854.27828	300	16	28.2 ± 0.8	51.9 ± 1.3
60 854.28179	300	15	27.9 ± 0.8	53.6 ± 1.1
60 854.28531	300	14	27.7 ± 0.9	51.1 ± 1.5
60 854.28882	300	14	28.7 ± 0.8	54.1 ± 1.3
60 854.29234	300	15	27.6 ± 1.0	53.5 ± 1.5
60 854.29585	300	14	27.1 ± 1.0	57.3 ± 1.5

Notes. Columns list the mid-exposure barycentric Julian date, exposure time (T_{exp}), maximum SNR, radial velocity (V_r) and rotational velocity ($\upsilon \sin i$).

Table A.2. Radial velocities of HD 99458 measured from the spectra presented in Skarka et al. (2019).

BJD − 2 450 000	V_r (km s^{-1})	BJD − 2 450 000	V_r (km s^{-1})
7 828.44658	28.3 ± 0.4	7 853.51071	66.7 ± 0.4
7 828.46791	30.5 ± 0.5	7 874.35562	4.1 ± 0.6
7 828.49370	32.5 ± 0.6	7 854.37255	32.9 ± 0.5
7 829.42227	65.4 ± 0.3	7 874.37695	6.1 ± 0.9
7 829.44360	63.4 ± 0.4	7 884.34898	31.3 ± 0.5
7 839.43422	35.0 ± 0.7	7 884.35990	30.6 ± 0.4
7 840.43219	56.5 ± 0.5	7 884.37081	30.8 ± 0.3
7 841.43370	−1.0 ± 0.6	7 884.38172	30.7 ± 0.4
7 843.42595	35.3 ± 0.6	7 891.36052	53.0 ± 0.3
7 844.41622	4.9 ± 0.3	7 891.38185	54.0 ± 0.3
7 844.43755	6.3 ± 0.3	7 902.31940	55.8 ± 0.7
7 844.45888	6.9 ± 0.4	8 203.30667	1.3 ± 0.6
7 844.48021	8.3 ± 0.3	8 203.32800	2.5 ± 0.4
7 844.54083	11.8 ± 0.2	8 203.34933	−1.0 ± 0.6
7 844.56216	12.0 ± 0.4	8 203.39051	−3.1 ± 0.5
7 844.58349	13.2 ± 0.3	8 203.41184	−2.3 ± 0.6
7 844.60482	14.0 ± 0.4	8 226.31602	60.8 ± 0.3
7 845.46456	70.2 ± 0.3	8 226.33735	62.2 ± 0.2
7 845.48589	70.3 ± 0.3	8 227.33847	29.3 ± 0.3
7 845.50722	69.1 ± 0.3	8 229.32680	69.8 ± 0.3
7 845.52855	69.2 ± 0.3	8 229.34813	70.3 ± 0.3
7 845.54989	68.8 ± 0.3	8 230.31655	11.7 ± 0.3
7 853.40406	61.7 ± 0.2	8 230.33788	10.3 ± 0.5
7 853.42539	63.7 ± 0.3	8 231.33008	28.6 ± 0.3
7 853.44672	64.4 ± 0.2	8 231.35141	29.0 ± 0.2
7 853.46805	64.2 ± 0.3	8 253.35443	47.9 ± 0.3
7 853.48938	65.1 ± 0.4	8 253.37576	49.8 ± 0.3

Appendix B: Frequencies in K2 and TESS data

Table B.1. Master list of 122 pulsation frequencies identified in three photometric datasets: TESS sectors 45–46 (S45), TESS sector 72 (S72), and K2.

ID	$f_{\rm best}$ (d^{-1})	σ_f (d^{-1})	Src	$f_{\rm S45}$ (d^{-1})	$A_{\rm S45}$ (mmag)	$f_{\rm S72}$ (d^{-1})	$A_{\rm S72}$ (mmag)	$f_{\rm K2}$ (d^{-1})	$A_{\rm K2}$ (mmag)	N	$A_{\rm max}$ (mmag)
f_1	31.52110	0.00020	S45	31.52110	1.040	31.52150	2.810	31.52000	0.860	3	2.810
f_2	27.74160	0.00010	S45	27.74160	1.800	27.74110	1.660	27.74120	1.000	3	1.800
f_3	29.72200	0.00020	S72	29.72360	0.760	29.72200	1.630	29.72260	1.420	3	1.630
f_4	27.38670	0.00020	S72	27.38300	1.550	27.38670	1.530	27.37780	0.800	3	1.550
f_5	28.11260	0.00020	K2	28.11360	1.380	28.11250	1.460	28.11260	1.070	3	1.460
f_6	31.49280	0.00030	S45	31.49280	0.680	31.49540	1.430	31.49340	0.630	3	1.430
f_7	27.68060	0.00020	S45	27.68060	1.180	27.67880	0.990	27.68060	0.890	3	1.180
f_8	28.87760	0.00020	S45	28.87760	1.090	28.87630	1.000	28.87670	1.070	3	1.090
f_9	28.05550	0.00020	S45	28.05550	1.030	28.05760	0.840	28.05500	0.860	3	1.030
f_{10}	27.62800	0.00020	S45	27.62800	0.940	27.62760	1.010	27.62740	0.600	3	1.010
f_{11}	27.39040	0.00040	K2	27.40050	0.290	—	—	27.39040	0.920	2	0.920
f_{12}	28.36250	0.00020	S45	28.36250	0.860	28.36050	0.920	28.36230	0.630	3	0.920
f_{13}	31.06400	0.00020	S45	31.06400	0.910	31.06520	0.600	31.06310	0.580	3	0.910
f_{14}	32.34450	0.00020	S45	32.34450	0.860	32.34860	0.910	32.34420	0.440	3	0.910
f_{15}	26.21350	0.00040	S72	26.21170	0.870	26.21350	0.800	26.21070	0.780	3	0.870
f_{16}	28.98780	0.00030	K2	28.98860	0.400	28.98930	0.830	28.98780	0.750	3	0.830
f_{17}	30.67910	0.00040	S72	30.67970	0.680	30.67910	0.830	30.67800	0.330	3	0.830
f_{18}	30.75890	0.00040	S72	30.75780	0.370	30.75890	0.830	30.75950	0.400	3	0.830
f_{19}	28.31630	0.00030	S45	28.31630	0.660	28.31730	0.420	28.31560	0.330	3	0.660
f_{20}	26.65500	0.00030	S45	26.65500	0.600	26.65180	0.460	26.65590	0.640	3	0.640
f_{21}	27.00390	0.00030	S45	27.00390	0.580	26.99930	0.410	27.00850	0.160	3	0.580
f_{22}	26.94560	0.00030	S45	26.94560	0.570	26.94940	0.440	26.94560	0.340	3	0.570
f_{23}	26.12570	0.00040	S45	26.12570	0.430	26.12680	0.560	26.12500	0.340	3	0.560
f_{24}	29.61150	0.00050	K2	29.60770	0.530	29.60750	0.450	29.61150	0.450	3	0.530
f_{25}	31.41490	0.00040	S45	31.41490	0.410	31.41580	0.460	—	—	2	0.460
f_{26}	25.89750	0.00040	S45	25.89750	0.420	25.89960	0.400	25.89750	0.280	3	0.420
f_{27}	29.13760	0.00060	K2	29.13780	0.270	29.13900	0.310	29.13760	0.390	3	0.390
f_{28}	27.42140	0.00120	S45	27.42140	0.380	—	—	—	—	1	0.380
f_{29}	31.64150	0.00040	S45	31.64150	0.370	31.64320	0.260	31.64080	0.190	3	0.370
f_{30}	29.05150	0.00050	S45	29.05150	0.350	29.05810	0.230	29.05090	0.170	3	0.350
f_{31}	26.19150	0.00090	K2	26.18950	0.220	—	—	26.19150	0.330	2	0.330
f_{32}	28.69360	0.00070	S45	28.69360	0.230	28.69220	0.300	28.69480	0.180	3	0.300
f_{33}	28.47710	0.00060	S45	28.47710	0.270	28.47080	0.280	—	—	2	0.280
f_{34}	29.27090	0.00080	S45	29.27090	0.210	29.26630	0.280	29.26750	0.110	3	0.280
f_{35}	25.39090	0.00090	S45	25.39090	0.180	25.39160	0.270	25.39000	0.150	3	0.270
f_{36}	28.77660	0.00070	S45	28.77660	0.250	28.77480	0.250	28.77570	0.270	3	0.270
f_{37}	28.15860	0.00070	S45	28.15860	0.260	28.15720	0.220	—	—	2	0.260
f_{38}	25.33170	0.00070	S45	25.33170	0.240	25.33230	0.180	25.33140	0.180	3	0.240
f_{39}	28.83140	0.00140	S45	28.83140	0.130	28.83790	0.240	28.83000	0.120	3	0.240
f_{40}	30.90610	0.00070	S45	30.90610	0.240	30.90770	0.130	30.90540	0.080	3	0.240
f_{41}	28.40390	0.00090	S45	28.40390	0.180	—	—	28.40300	0.230	2	0.230
f_{42}	27.29660	0.00090	S45	27.29660	0.210	—	—	—	—	1	0.210
f_{43}	28.93820	0.00080	S45	28.93820	0.200	28.93980	0.130	—	—	2	0.200
f_{44}	31.79960	0.00080	S45	31.79960	0.200	31.79120	0.170	31.79800	0.120	3	0.200
f_{45}	29.62210	0.00170	S45	29.62210	0.190	—	—	—	—	1	0.190
f_{46}	26.89370	0.00090	S45	26.89370	0.180	—	—	26.89240	0.100	2	0.180
f_{47}	29.42460	0.00170	S72	—	—	29.42460	0.170	29.42950	0.110	2	0.170
f_{48}	32.39980	0.00380	S72	—	—	32.39980	0.170	32.39970	0.030	2	0.170
f_{49}	32.71020	0.00150	S45	32.71020	0.100	32.71050	0.170	—	—	2	0.170
f_{50}	28.41670	0.00550	S72	—	—	28.41670	0.160	—	—	1	0.160
f_{51}	29.56910	0.00150	K2	—	—	—	—	29.56910	0.150	1	0.150
f_{52}	29.68990	0.00120	S45	29.68990	0.150	—	—	—	—	1	0.150
f_{53}	30.09000	0.00100	S45	30.09000	0.150	30.08650	0.130	—	—	2	0.150

Table B.1. continued

ID	$f_{\rm best}$ (d^{-1})	σ_f (d^{-1})	Src	$f_{\rm S45}$ (d^{-1})	$A_{\rm S45}$ (mmag)	$f_{\rm S72}$ (d^{-1})	$A_{\rm S72}$ (mmag)	$f_{\rm K2}$ (d^{-1})	$A_{\rm K2}$ (mmag)	N	$A_{\rm max}$ (mmag)
f_{54}	32.43860	0.00440	S72	—	—	32.43860	0.140	—	—	1	0.140
f_{55}	32.25780	0.00120	S45	32.25780	0.130	32.26490	0.130	—	—	2	0.130
f_{56}	33.07800	0.00120	S45	33.07800	0.130	33.07250	0.130	—	—	2	0.130
f_{57}	33.15020	0.00230	S72	—	—	33.15020	0.130	—	—	1	0.130
f_{58}	26.06630	0.00130	S45	26.06630	0.120	—	—	—	—	1	0.120
f_{59}	26.22620	0.00250	S45	26.22620	0.120	—	—	—	—	1	0.120
f_{60}	30.33070	0.00120	S45	30.33070	0.120	—	—	30.32820	0.080	2	0.120
f_{61}	30.73880	0.00170	S45	30.73880	0.120	—	—	—	—	1	0.120
f_{62}	32.08840	0.00250	S72	—	—	32.08840	0.120	—	—	1	0.120
f_{63}	25.28520	0.00190	S45	25.28520	0.080	—	—	25.27900	0.110	2	0.110
f_{64}	25.29560	0.00340	K2	—	—	25.29110	0.110	25.29560	0.090	2	0.110
f_{65}	26.36150	0.00260	S72	—	—	26.36150	0.110	—	—	1	0.110
f_{66}	27.26910	0.00290	S72	—	—	27.26910	0.110	—	—	1	0.110
f_{67}	30.70470	0.00220	S45	30.70470	0.110	—	—	—	—	1	0.110
f_{68}	33.13510	0.00170	S45	33.13510	0.110	—	—	—	—	1	0.110
f_{69}	30.17140	0.00160	S45	30.17140	0.100	—	—	—	—	1	0.100
f_{70}	33.33660	0.00160	S45	33.33660	0.100	—	—	—	—	1	0.100
f_{71}	27.18610	0.00350	S72	—	—	27.18610	0.090	27.17640	0.040	2	0.090
f_{72}	28.21560	0.00600	S72	—	—	28.21560	0.080	—	—	1	0.080
f_{73}	29.50340	0.00190	S45	29.50340	0.080	—	—	—	—	1	0.080
f_{74}	29.63540	0.00280	K2	—	—	—	—	29.63540	0.080	1	0.080
f_{75}	30.46120	0.00180	S45	30.46120	0.080	—	—	30.46240	0.060	2	0.080
f_{76}	33.18350	0.00210	S45	33.18350	0.080	—	—	—	—	1	0.080
f_{77}	27.34200	0.00310	S45	27.34200	0.070	—	—	—	—	1	0.070
f_{78}	28.07900	0.00250	S45	28.07900	0.070	—	—	—	—	1	0.070
f_{79}	32.41680	0.00250	S45	32.41680	0.070	—	—	—	—	1	0.070
f_{80}	32.45830	0.00230	S45	32.45830	0.070	—	—	—	—	1	0.070
f_{81}	25.45660	0.00270	S45	25.45660	0.060	—	—	—	—	1	0.060
f_{82}	28.61960	0.00350	K2	—	—	—	—	28.61960	0.060	1	0.060
f_{83}	29.87910	0.00260	S45	29.87910	0.060	—	—	—	—	1	0.060
f_{84}	31.09730	0.00250	S45	31.09730	0.060	—	—	—	—	1	0.060
f_{85}	33.25780	0.00250	S45	33.25780	0.060	—	—	—	—	1	0.060
f_{86}	34.61380	0.00240	S45	34.61380	0.060	—	—	—	—	1	0.060
f_{87}	27.43940	0.00450	K2	—	—	—	—	27.43940	0.050	1	0.050
f_{88}	27.88280	0.00410	K2	—	—	—	—	27.88280	0.050	1	0.050
f_{89}	31.89560	0.00460	K2	—	—	—	—	31.89560	0.050	1	0.050
f_{90}	28.23360	0.00480	K2	—	—	—	—	28.23360	0.040	1	0.040
f_{91}	28.74560	0.00530	K2	—	—	—	—	28.74560	0.040	1	0.040
f_{92}	30.86110	0.00630	K2	—	—	—	—	30.86110	0.040	1	0.040
f_{93}	32.77010	0.00540	K2	—	—	—	—	32.77010	0.040	1	0.040
f_{94}	32.98960	0.00400	S45	32.98960	0.040	—	—	—	—	1	0.040
f_{95}	27.25260	0.00620	K2	—	—	—	—	27.25260	0.030	1	0.030
f_{96}	27.48740	0.00750	K2	—	—	—	—	27.48740	0.030	1	0.030
f_{97}	27.56760	0.00720	K2	—	—	—	—	27.56760	0.030	1	0.030
f_{98}	28.38350	0.00840	K2	—	—	—	—	28.38350	0.030	1	0.030
f_{99}	28.90980	0.00610	K2	—	—	—	—	28.90980	0.030	1	0.030
f_{100}	29.06410	0.01050	K2	—	—	—	—	29.06410	0.030	1	0.030
f_{101}	29.52880	0.00700	K2	—	—	—	—	29.52880	0.030	1	0.030
f_{102}	29.78490	0.00650	K2	—	—	—	—	29.78490	0.030	1	0.030
f_{103}	31.59520	0.00710	K2	—	—	—	—	31.59520	0.030	1	0.030
f_{104}	31.83180	0.00780	K2	—	—	—	—	31.83180	0.030	1	0.030
f_{105}	32.28490	0.00820	K2	—	—	—	—	32.28490	0.030	1	0.030
f_{106}	33.04120	0.00690	K2	—	—	—	—	33.04120	0.030	1	0.030
f_{107}	24.99990	0.01310	S72	—	—	24.99990	0.020	—	—	1	0.020
f_{108}	26.09390	0.01100	K2	—	—	—	—	26.09390	0.020	1	0.020
f_{109}	28.01880	0.00870	K2	—	—	—	—	28.01880	0.020	1	0.020
f_{110}	28.43600	0.01130	K2	—	—	—	—	28.43600	0.020	1	0.020

Table B.1. continued

ID	$f_{\rm best}$ (d^{-1})	σ_f (d^{-1})	Src	$f_{\rm S45}$ (d^{-1})	$A_{\rm S45}$ (mmag)	$f_{\rm S72}$ (d^{-1})	$A_{\rm S72}$ (mmag)	$f_{\rm K2}$ (d^{-1})	$A_{\rm K2}$ (mmag)	N	$A_{\rm max}$ (mmag)
f_{111}	29.08580	0.01190	K2	—	—	—	—	29.08580	0.020	1	0.020
f_{112}	29.11220	0.01010	K2	—	—	—	—	29.11220	0.020	1	0.020
f_{113}	29.15810	0.01040	K2	—	—	—	—	29.15810	0.020	1	0.020
f_{114}	29.48100	0.00880	K2	—	—	—	—	29.48100	0.020	1	0.020
f_{115}	30.21810	0.01230	K2	—	—	—	—	30.21810	0.020	1	0.020
f_{116}	30.62530	0.00940	K2	—	—	—	—	30.62530	0.020	1	0.020
f_{117}	30.83970	0.01490	K2	—	—	—	—	30.83970	0.020	1	0.020
f_{118}	33.16960	0.01190	K2	—	—	—	—	33.16960	0.020	1	0.020
f_{119}	26.14270	0.02820	K2	—	—	—	—	26.14270	0.010	1	0.010
f_{120}	28.54060	0.01440	K2	—	—	—	—	28.54060	0.010	1	0.010
f_{121}	30.41490	0.01430	K2	—	—	—	—	30.41490	0.010	1	0.010
f_{122}	33.42840	0.01430	K2	—	—	—	—	33.42840	0.010	1	0.010

Notes. Identifiers $f_{\rm n}$ are ordered by decreasing $A_{\rm max}$. The best frequency $f_{\rm best}$ and its uncertainty σ_f were taken from the most precise detection (column Src). N is the number of datasets in which the frequency is detected. Amplitudes are in mmag; em dashes indicate non-detection.

Appendix C: 2D-DFT diagrams

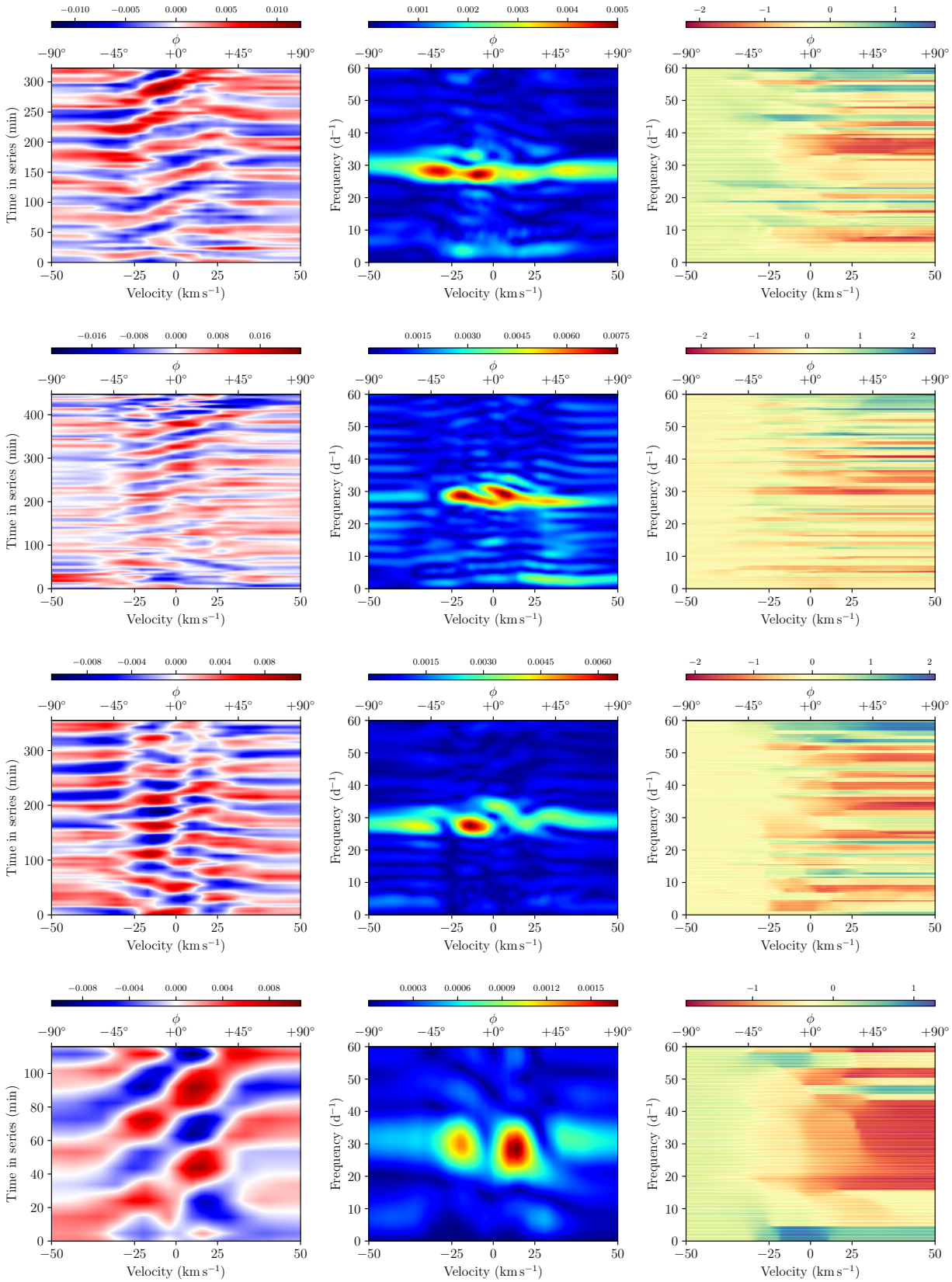


Fig. C.1. Top to bottom: 2D-DFT summary of the LPV analysis of datasets DS1–DS4. The corresponding orbital phases are $\varphi_{\rm orb}$ = 0.964–0.048, 0.056–0.170, 0.072–0.163, and 0.185–0.214, respectively. The left panels show LPV in residual spectra, the middle panels demonstrate amplitude variability in the 2D Fourier transform of LPV, and the right panels show the corresponding phase.

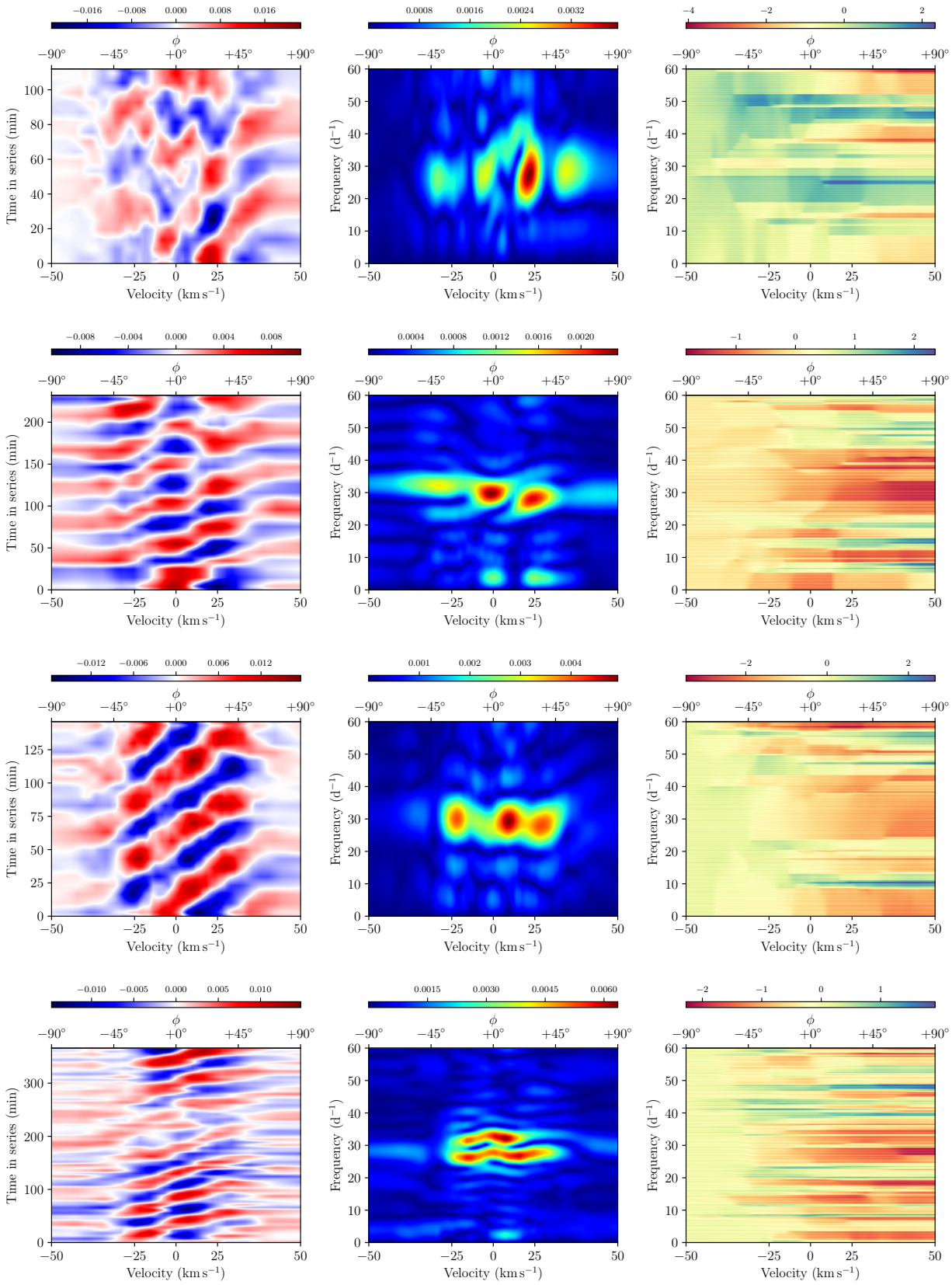


Fig. C.2. Top to bottom: 2D-DFT summary of the LPV analysis of datasets DS5, DS7–DS9. The corresponding orbital phases are $\varphi_{\rm orb}$ = 0.357–0.386, 0.527–0.586, 0.621–0.658 and 0.705–0.799, respectively. The left panels show LPV in residual spectra, the middle panels demonstrate amplitude variability in the 2D Fourier transform of LPV, and the right panels show the corresponding phase.